

**STUDY OF FORMATION AND CONVECTIVE TRANSPORT OF AEROSOLS  
USING OPTICAL DIAGNOSTIC TECHNIQUE**

A Dissertation

by

TAE-KYUN KIM

Submitted to the Office of Graduate Studies of  
Texas A&M University  
in partial fulfillment of the requirements for the degree of

DOCTOR OF PHILOSOPHY

May 2004

Major Subject: Mechanical Engineering

**STUDY OF FORMATION AND CONVECTIVE TRANSPORT OF AEROSOLS  
USING OPTICAL DIAGNOSTIC TECHNIQUE**

A Dissertation

by

TAE-KYUN KIM

Submitted to Texas A&M University  
in partial fulfillment of the requirements  
for the degree of

DOCTOR OF PHILOSOPHY

Approved as to style and content by:

---

Kenneth D. Kihm  
(Chair of Committee)

---

Mahboobul Mannan  
(Member)

---

Peter McIntyre  
(Member)

---

Denis Phares  
(Member)

---

Dennis L. O'Neal  
(Head of Department)

May 2004

Major Subject: Mechanical Engineering

**ABSTRACT**

Study of Formation and Convective Transport of Aerosols Using Optical Diagnostic  
Technique. (May 2004)

Tae-Kyun Kim, B.S., Korea Military Academy;

M.S., Texas A&M University

Chair of Advisory Committee: Dr. Kenneth D. Kihm

The characteristics of liquid and solid aerosols have been intensively investigated by means of optical diagnostic techniques. Part I describes the characteristics of liquid aerosol formation formed by heat transfer fluids (HTFs) from bulk liquids. Part II investigates the characteristics of convective transport behavior of solid particles in virtual impactor (VI).

The objective of part I is to establish correlations which offer predictions on atomized particle size of HTFs which are widely and commonly used in process industries. There are numerous reports stating that mist explosions formed from leakage cause disastrous accidents in process industries. For safety concerns, the characteristics of mist formation should be known in order to prevent HTFs from catching on fire or exploding. The empirical data on formation of mist are collected by the optical measurement technique, the Fraunhofer diffraction. The Buckingham-PI theorem is applied to establish a correlation between empirical data and representative physical

properties of HTFs. Final results of correlations are solved by a statistical method of linear regression.

The objective of part II is to investigate the characteristics of convective transport behavior in virtual impactor (VI) which is used to sort polydisperse precursor powder in the process industries of superconductor wire. VI is the device to separate polydisperse particles as a function of particle size by using the difference in inertia between different sizes of particles. To optimize VI performance, the characteristics of convective transport should be identified. This objective is achieved by visualization techniques. The applied visualization techniques are Mie-scattering and laser induced fluorescence (LIF). To investigate analytically, a local Stokes number is introduced in order to offer criteria on predicting the efficiency of VI performance and boundary effect on particle separation. The achieved results can enhance performance and eliminate defects by having knowledge of the behavior of solid particles in VI.

**DEDICATION**

to my loving family

## ACKNOWLEDGMENTS

I would like to express my heartfelt thanks to my advisor, Dr. Kenneth D. Kihm, for his guidance and support throughout these studies. Also, I sincerely appreciate my graduate committee members, Dr. Mahboobul Mannan, Dr. Peter McIntyre, and Dr. Denis Phares, for their support and advice on this research.

I would like to thank to my two collaborators: Kiran Krishna from the Department of Chemical Engineering at Texas A&M University who helped to conduct the research on part I; and Satyanarayanan Seshadri from the Department of Mechanical Engineering at Texas A&M University who worked on the research for part II. Working with them made great results.

I would like to express my appreciation to my parents for their warmth and to my wife and sons for their encouragement and support during these studies. Also, I would like to thank my lab members for their support.

Finally, I would like to express my sincere gratitude to my country and the Korean Army for giving me an opportunity to undertake these fruitful studies at the Department of Mechanical Engineering at Texas A&M University.

## TABLE OF CONTENTS

	Page
ABSTRACT.....	iii
DEDICATION.....	v
ACKNOWLEDGMENTS.....	vi
TABLE OF CONTENTS.....	vii
LIST OF FIGURES.....	x
LIST OF TABLES.....	xv
NOMENCLATURE.....	xvii
 CHAPTER	
I INTRODUCTION.....	1
II THE CHARACTERISTICS OF LIQUID AEROSOL FORMATION OF HEAT TRANSFER FLUIDS (HTFs): RESEARCH BACKGROUND ON PART I.....	3
2.1 Motivation.....	3
2.2 Flame Propagation of Liquid Droplets.....	6
2.3 Atomization Process.....	12
2.4 Aerosol Particle Distribution.....	16
2.5 Particle Size Measurement.....	17
2.6 Atomization Analysis on Empirical Data.....	21
III EXPERIMENTAL CONDITIONS AND SETUP.....	23
3.1 Test Heat Transfer Fluids.....	23
3.2 Experimental Setup.....	28
3.2.1 General Description of System.....	28
3.2.2 Plain-Orifice Nozzle.....	30
3.2.3 Malvern System.....	34
3.3 Experimental Conditions.....	37

CHAPTER	Page
IV RESULTS AND ANALYSIS.....	38
4.1 Results and Analysis of Measurements.....	38
4.1.1 Analysis at the Reference Condition.....	38
4.1.2 Pressure Effect on Atomization.....	41
4.1.3 Temperature Effect on Atomization.....	43
4.2 Correlation on Predicted Particle Diameter.....	46
4.3 Validation of Correlation Results.....	51
V DISCUSSION AND FURTHER STUDY ON LIQUID FORMATION OF HTFS.....	54
VI THE CHARACTERISTICS OF CONVECTIVE TRANSPORT OF SOLID PARTICLES IN VIRTUAL IMPACTOR: RESEARCH BACKGROUND FOR PART II.....	60
6.1 Motivation.....	60
6.2 The Effect of Particle Size on Superconductor Wire and Tape.....	64
6.3 Sorting Particles by Virtual Impactor.....	66
6.4 Visualization on Micro Size Solid Particles in VI.....	71
6.5 Particle Generation of Monodisperse Size.....	78
VII EXPERIMENTAL SETUP .....	82
7.1 General Apparatus.....	82
7.1.1 Light Illumination Optics System.....	82
7.1.2 VI System.....	86
7.1.3 Image Recording/Processing System.....	91
7.1.4 Particle Imaging System .....	91
7.1.5 Particle Generation System.....	94
7.2 Verification.....	101
7.2.1 Verification of Particle Size and Monodisperse Distribution.....	101
7.2.2 Verification of Detecting Fluorescent Image under Mixture with Dust.....	106



CHAPTER	Page
VIII RESULTS AND ANALYSIS.....	108
8.1 Collecting Efficiency of VI.....	108
8.2 Visualization of Particle Trajectory.....	114
8.2.1 Lower Stokes Number.....	114
8.2.2 Higher Stokes Number.....	117
8.2.3 Defect Particles for Higher Stokes Number.....	117
8.2.4 Analysis of Defect Particles by Local Stokes Number.....	119
8.2.5 Characteristics of Convective Transport.....	126
8.3 Mass Loading Effect on Current System.....	128
8.3.1 Experimental Conditions.....	128
8.3.2 Optimized Mass Loading Condition.....	129
8.3.3 Analysis of the Status at Nozzle Throat.....	133
IX DISCUSSION AND FURTHER STUDY ON PART II.....	140
X CONCLUSION.....	145
REFERENCES.....	147
APPENDIX A.....	154
APPENDIX B.....	157
APPENDIX C.....	160
VITA.....	161

## LIST OF FIGURES

FIGURE	Page
2.1 Concept of mist and vapor flammability.....	5
2.2 Processes of a single droplet burning .....	7
2.3 Total surface area ratio with respect to number of particles when a single initial droplet diameter of 1cm breaks into smaller particles having the identical liquid volume.....	9
2.4 Flame propagation speed as a function of particle diameter.....	11
2.5 Classification of disintegration modes and their characteristics.....	14
2.6 Images of three liquid disintegration processes recorded by high-speed CCD camera at 500 frames per second.....	15
2.7 Different aerosol particle distribution by Rosin-Rammler analytical model with different values of the constant $q$ .....	17
2.8 Fraunhofer diffraction particle size analyzer; Malvern system.....	20
3.1 Properties of density variation of six Heat Transfer Fluids as a function of temperature.....	26
3.2 Properties of viscosity variation of six Heat Transfer Fluids as a function of temperature.....	26
3.3 Result of measurement on the surface tension of six Heat Transfer Fluids.....	28
3.4 Experimental setup.....	29
3.5 Apparatus of plain-orifice nozzle.....	31
3.6 Mass flow rate as a function of Reynolds number.....	33
3.7 Comparison of $C_D$ between measurement and calculation of Eq. (3.3).....	35

FIGURE	Page
3.8 Applied $C_D$ for research as a function of theoretical Reynolds number.....	35
3.9 Example of calibration result of particle distribution of reticle.....	36
4.1 Measurement result and analysis on three Heat Transfer Fluids at their reference condition.....	39
4.2 Measurement result and analysis of pressure effect.....	42
4.3 Measurement result and analysis of temperature effect.....	45
4.4 Correlation results for six Heat Transfer Fluids compared with measured drop size at a given droplet formation condition.....	48
5.1 Prediction of SMD for six different Heat Transfer Fluids under 500 psig, 130 °C, and 0.21 mm of nozzle diameter.....	55
5.2 Images of captured flame propagation using butane gas.....	58
6.1 Process of fabrication of superconductor wire.....	61
6.2 Two examples of particle size distribution of precursor.....	63
6.3 Principle of inertial impactor.....	67
6.4 Principle of virtual impactor on separating poly-dispersed solid particles using inertia difference between larger and smaller particles.....	70
6.5 Principle of fluorescence process.....	75
6.6 Example of the characteristic spectra of fluorescent particles .....	76
6.7 Examples of using fluorescent particles in polydisperse dust particles for the study of the characterization on particle behavior and investigating efficiency of system.....	77
6.8 Diagram of the instability on the liquid surface of a cylindrical jet column producing liquid droplets .....	80

FIGURE	Page
6.9 Process of generating monodisperse solid particles from uniform size of liquid particles generated by VOAG.....	81
7.1 General apparatus of experimental setup for investigating the characteristics of transport behavior of different sizes of solid particles in virtual impactor using visualization techniques.....	83
7.2 Design of geometric optics for illuminating two test areas and images of implemented setup.....	85
7.3 Virtual impactor applied to research .....	87
7.4 Images of VI test rig.....	89
7.5 Configuration of air flow control system.....	90
7.6 Image recording/processing system.....	92
7.7 Particle imaging system of reflected fluorescent microscope.....	93
7.8 VOAG system .....	96
7.9 Dust feeder system.....	99
7.10 Particle distribution of Arizona Road Dust.....	100
7.11 Captured images of particles collected by filter papers.....	102
7.12 Images of generated particle settled on the surface of microscopic cover glass located on the observation window glass at minor flow.....	104
7.13 Results of verification on detecting images under loading ARD only using optical filter.....	106
7.14 Detecting fluorescent particles only using optical filter when mixture of ARD and fluorescent particles is loaded.....	107
8.1 Areas of investigation for collecting efficiency of current VI system and example of Mie-scattering image of captured particles.....	110

FIGURE	Page
8.2 Frequencies of detecting particles at major and minor flow for Stokes number of 0.72.....	112
8.3 Result of evaluating collecting efficiency of major flow of VI.....	113
8.4 Visualized images of lower Stokes number.....	116
8.5 Visualized images of higher Stokes number.....	118
8.6 Visualized images of defect particles under higher Stokes number.....	120
8.7 Velocity profile of current VI at the nozzle throat under designed flow condition.....	121
8.8 Local Stokes numbers at nozzle throat for smaller particles under designed air flow rate of 10.26 SCFH .....	123
8.9 Local Stokes number for larger particles under designed air flow rate of 10.26 SCFH.....	124
8.10 Enlarged local Stokes number for larger particles using the velocity profile of converging flow.....	126
8.11 Schematically illustrated characteristics of convective transport of solid particles in virtual impactor as a function of Stokes number under a given flow rate.....	127
8.12 Images of LIF for two different mass loading conditions.....	129
8.13 The status of nozzle throat after running 5 minutes for four different mass loading conditions.....	131
8.14 Distribution patterns of particles for two different mass loading conditions.....	132
8.15 The ratio of total cross-sectional area of particles which occupy a single plane at nozzle throat to area of nozzle throat.....	134
8.16 Individual particle distribution in the reference volume.....	136
9.1 Modified inlet design for eliminating defect particles by introducing clean air of sheath flow.....	142

FIGURE	Page
B.1 Apparatus of Fisher Surface Tensiomat Model 20.....	158
B.2 Comparison of surface tension between given data from manufacturer and measurement on AAR.....	159

## LIST OF TABLES

TABLE	Page
2.1 Example of Heat Transfer Fluids and applications.....	4
2.2 Examples of mean diameters and applications.....	18
3.1 Characteristic temperatures of Heat Transfer Fluids.....	24
3.2 Established experimental temperature conditions.....	25
3.3 Correlated properties of Heat Transfer Fluids as a function of temperature.....	27
3.4 Matrix for experimental condition.....	37
3.5 Combinations of seven experimental conditions .....	37
4.1 Result of correlation for predicting droplet size using Eq. (2.5).....	47
4.2 Description of indication of ' <i>Log diff</i> ' for reliability on experimental data.....	51
4.3 Exponential value of correlation for Eq. (4.2) .....	53
7.1 Design requirements for current virtual impactor.....	88
7.2 Equivalent particle sizes for precursor and Rhodamine 590 for a given Stokes number and designed air flow rate.....	98
7.3 Average diameter and standard deviation of particles generated by VOAG.....	105
8.1 Experimental conditions of particle sizes and velocities to vary Stokes numbers for gathering data on collecting efficiency.....	109
8.2 Detected particle number density for both major and minor flow for Stokes number ranging from 0.42 to 25.0.....	111

TABLE	Page
8.3 Conditions of ARD mass loading from dust feeder.....	128
8.4 Cross-sectional area and volume of ARD per 100 particles.....	138
8.5 Result of analysis for number of particles in a reference volume.....	138
8.6 Ratio of total summation of particles' diameter at a particle plane to nozzle width.....	139
9.1 $R_{length}$ for precursors.....	144
B.1 Calculated value of reading.....	159



**NOMENCLATURE**

$A$	Area
$C$	Percent Contrast
$C_D$	Discharge Coefficient
$C$	Concentration
$D$	Representative Diameter
$d$	Diameter
$d_p$	Particle Diameter
$d_{pipe}$	Pipe Diameter
$g$	Acceleration of Gravity
$h$	Plank Constant
$I$	Intensity
$I(b)$	Intensity of Background
$I(o)$	Intensity of Object
$i_s$	Scattering Parameter
$J_C$	Critical Current Density
$K$	Evaporation Constant
$L$	Dimension of Length
$L$	Pipe Length, Distance, Mean Circumference of the Ring
$l_o$	Orifice Length
$M$	Dimension of Mass

$M$	Weight
$\dot{m}$	Mass Flow Rate
$N$	Particle Number
$N_i$	Number of Drops in Size Range $i$
$n$	Index of Refraction
$P$	Pressure
$R^2$	Coefficient of Determination
$R_{\text{length}}$	Ratio of Total Summation of Particle Diameter at a Particle Plane to Width
$Q$	Fraction of Total Volume, Quantum Efficiency
$q$	Constant
$S$	Dial Reading
$T$	Dimension of Time
$T$	Temperature
$t$	Droplet Lifetime
$V$	Velocity
$\dot{V}$	Volume Flow Rate
$w$	Characteristic Length Scale
$X$	Constant
$x$	Axial Distance from Nozzle

#### Greek Symbol

$\varepsilon$	Absorptivity
---------------	--------------

$\Delta$	Difference
$\eta$	Collecting Efficiency
$\lambda$	Wavelength
$\mu$	Viscosity
$\theta$	Angle
$\rho$	Density
$\sigma$	Surface Tension
$\sigma_{\text{std}}$	Standard Deviation
$\nu$	Light Frequency

#### Subscript

<i>abs</i>	Absorption
<i>c</i>	Critical
<i>ems</i>	Emission
<i>F</i>	Fluorescent
<i>g</i>	Gas
<i>I</i>	Incident Light
<i>l</i>	Liquid
<i>j</i>	Liquid Jet
<i>o</i>	Nozzle Orifice
<i>p</i>	Particle
<i>s</i>	Scattered Light

## Dimensionless Parameter

Oh	Ohnesorge Number
Re	Reynolds Number
Stk	Stokes number
We	Weber Number

## Abbreviation

ARD	Arizona Road Dust
CCD	Charged Couple Device
CW	Continuous Wave
HTF	Heat Transfer Fluid
PIT	Powder-in-Tube
SMD	Sauter Means Diameter
SCFH	Standard Cubic Feet per Hour
VI	Virtual Impactor
VOAG	Vibrating Orifice Aerosol Generator

## Heat Transfer Fluid Name

AAR	Alkylated Aromatic
BDP	Bi/D-phenly Oxide
DAL	Diaryl Alkyl

DTA	Di-/Tri-Aryl Compound
MTO	Modified Terpenyl Oxide
WMO	White Mineral Oil

## CHAPTER I

### INTRODUCTION

Natures of aerosol particles are not of great interest to common peoples since they are too small to be notified. The aerosol particles, however, have great effects on peoples' way of living. The most extreme example of the effect of aerosol particles has been broadcasted on September 11, 2001. When the Twin Towers of the World Trade Center collapsed on that day, people watched with horrible the tremendous amount of dust storm that overtook people and left them covered with debris from buildings. Environmental Protection Agency (EPA) has collected samples of aerosol pollutant from New York for analysis and recently announced that the pollution was not seriously toxic as it was considered (report of '*World Trade Center Disaster Response Air Monitoring Data Summaries*,' EPA, 2002). Subsequently, 'Anthrax threats' in public area, government offices have added to this feeling of terrors. These incidents have led to more general interest on the serious effect of aerosols on our lives.

The aerosol is great concerns to researchers in a certain area. The applications of aerosols can be easily found around us and the areas of its application are various. The aerosol is defined as a suspension of solid or liquid particles in a gas. In this dissertation,

---

The model journal is the *Journal of Loss Prevention in the Process Industries*.

two typical types of aerosol, liquid and solid, will be discussed.

Part I describes the characteristics of liquid aerosol formation investigated by the method of optical measurement, Fraunhofer diffraction, in order to establish correlations on prediction of atomized particle size distribution. Applied liquids are heat transfer fluids (HTFs) which are extensively used in process industries. Chapter II explains the motivation and objective of research and research theories of background to be applied. Chapter III shows experiment setup and established experiment conditions to conduct research. Chapter IV has the results and analysis on liquid aerosol formation of heat transfer fluids. Chapter V discusses the suggestion and further studies on liquid aerosol research.

Part II focuses on the characteristics of convective transport behavior of solid particle separation inside virtual impactor (VI) by means of visualization techniques. Chapter VI tells the motivation, objectives, and the basic principles of research on the method of particle separation, particle generation, and visualization. Chapter VII illustrates experimental setup and conditions to achieve objectives. Chapter VIII contains the result and analysis on the characteristics of convective transport behavior in VI. Chapter IX will discuss the summary of result on the part II.

Chapter X will summarize and make conclusion regarding the study on the characteristics of liquid aerosol formation and convective transport behavior of solid aerosol.

## CHAPTER II

### THE CHARACTERISTICS OF LIQUID AEROSOL FORMATION OF HEAT TRANSFER FLUIDS (HTFs): RESEARCH BACKGROUND ON PART I

Chapter II will discuss the motivation and objective of liquid formation of HTFs research and describe background theories to achieve the research objectives.

#### 2.1 Motivation

In the chemical process industry, HTFs are utilized in a heat exchanger to enhance the effectiveness of operation. Table 2.1 shows some examples of products and their applications. The one of reasons of using HTFs is safety considerations in order to avoid from getting fire or explosion since their flash point is relatively high. This makes people believe that HTFs are safe material for dealing with high temperature. There, however, are 54 fires and explosions involving HTFs for a recent ten year period, resulting in \$150 million in losses (Febo and Valiulis, 1995). Some of accidents were caused by mist explosion that was formed by leakage under higher working pressure and relatively high temperature conditions with ambient temperature.

The flammability of the higher boiling organic fluids and petroleum oils was investigated by Sullivan et al. (1947). They studied the explosive hazard due to oil mists in the atmosphere and categorized the spontaneous ignition temperature of aerosols of various flammable fluids. The possibility of mist explosions below flash point of



Table 2.1

Example of Heat Transfer Fluids and their applications

Product Name	Chemical Composition	Maximum Working Temperature	Applications
DOWTHERM A <sup>1</sup>	Diphenyl Oxide/Biphenyl Blend	400 °C	Indirect heat transfer for liquid phase or vapor phase heating
DOWTHERM G <sup>1</sup>	Mixture of di- and tri-aryl compounds	371 °C	Liquid phase heat transfer systems
DOWTHERM J <sup>1</sup>	Mixture of Isomers of an Alkylated	315 °C	Single fluid heating and cooling
DOWTHERM Q <sup>1</sup>	Mixture of Diphenylethane and Alkylated Aromatics	330 °C	An alternative to hot oils in liquid phase heat transfer
DOWTHERM RP <sup>1</sup>	Diaryl Alkyl	350 °C	Polyester, nylon, and other synthetic fiber processing facilities
MultiTherm IG-4 <sup>2</sup>	White Mineral Oil	316 °C	Chemical Processing industry, asphalt storage facilities, die temperature control systems, commercial laundries
MultiTherm PG-1 <sup>2</sup>	White Mineral Oil	316 °C	Chemical Processing , food processing, plastics industry, die casting

<sup>1</sup> Product from Dow Chemical company

<sup>2</sup> Product from MultiTerm LLC company

flammable liquids was recognized by Eichhorn (1955). He investigated flammability of flammable liquids under different air/fuel ratio and temperature for mist and vapor. Figure 2.1 summarizes his experimental result showing that mist can explode under favorable conditions when temperature is even below flash point.

From above studies, it is clear that mist formation of HTFs causes imminent safety concerns to process industries where HTFs are extensively used. The available data on characteristics of mist formation of HTFs that can prevent disastrous accidents, however, is limited since research on this topic has not been intensively conducted. The objective of part I is to achieve valuable information on the mist formation of HTFs to prevent accidents from process industries.

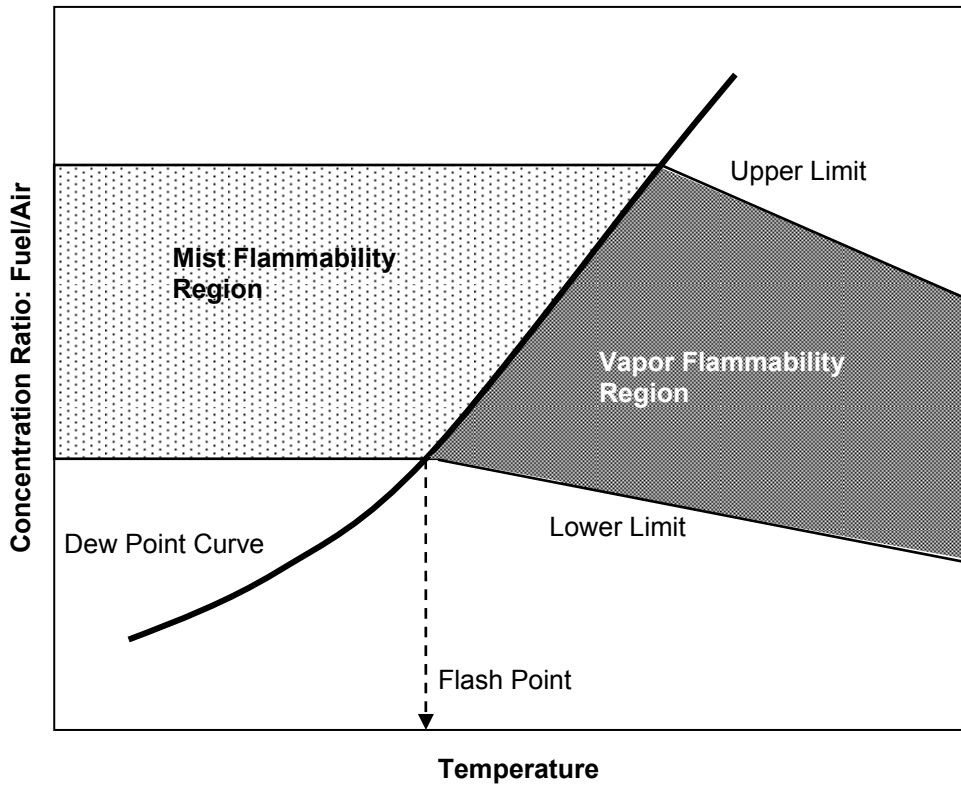


Fig. 2.1. Concept of mist and vapor flammability (Eichhorn, 1955).

## 2.2 Flame Propagation of Liquid Droplets

The definition of explosion is the flame propagation at very high velocity, resulting abrupt rise in temperature and pressure. Thus, explosion is the one of the process of flame propagations. To have better understanding on the explosion, the basic principle of flame propagation needs to be understood. The basic phenomenon in flame propagation will be only discussed since it is very complicated mechanism that is beyond the scope of this dissertation.

The first step is to understand a flame process of a single particle. The processes of burning a single particle schematically illustrated in Fig. 2.2. are:

1. Heating Process

Liquid droplet is heated by outer heating source. Heating energy is consumed by liquid droplet in order to reach its boiling point.

2. Vaporization Process

The temperature of surface reaches at boiling point, liquid begins to vaporize. The amount of vapor is supplied through the surface of droplet. Outer source of energy is being consumed by liquid to be totally vaporized.

3. Burning Process at Flash Point

Vapor burns when amount of vapor is sufficient and ignition energy exceeds activation energy.

From this principle of a burning process of a single droplet, two facts about the effect of particle size on flame propagation can be extracted as:

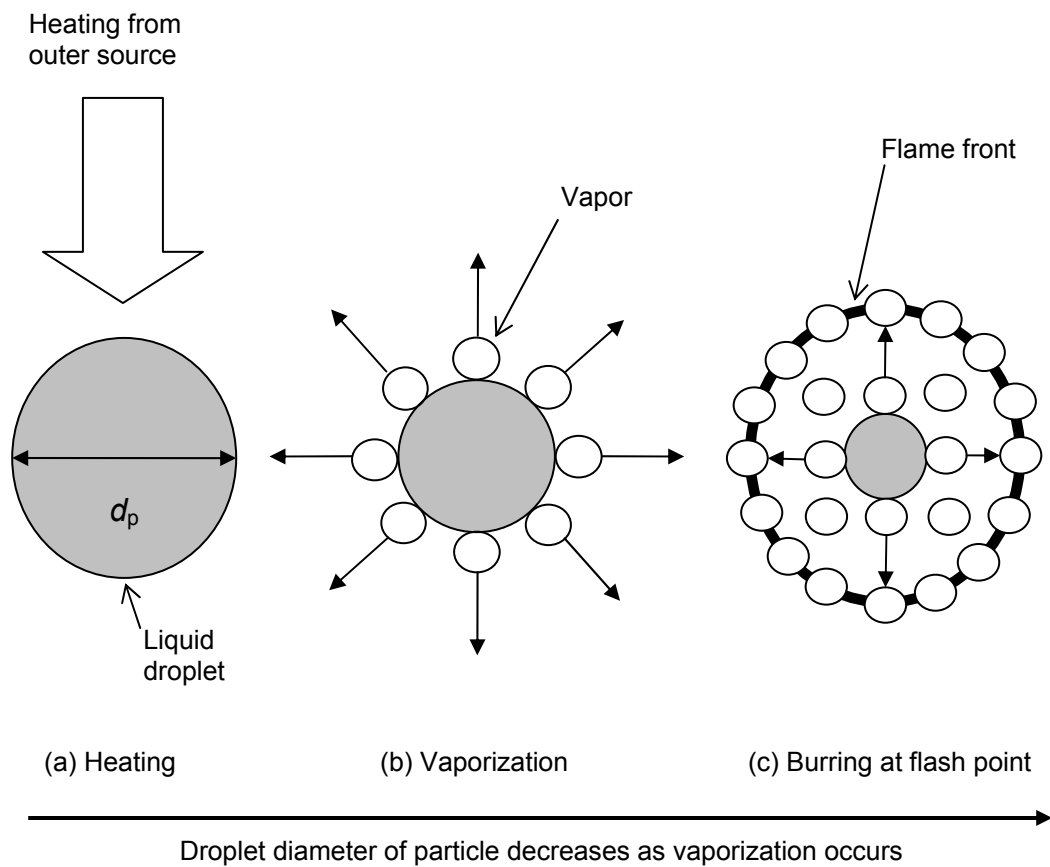


Fig. 2.2. Processes of a single droplet burning (propagation of flame front occurs when sufficient amount of vapor is supplied by droplet. Without sufficient amount of vapor, flame is quenched. Flame propagates to unburned vapor area).

## 1. Droplet Lifetime

The droplet life time is proportional to particle diameter. This can be expressed by well known  $d_p^2$ -law for combustion science as following

$$t = \frac{d_p^2}{K} \quad (2.1)$$

where  $t$  is the droplet lifetime for burning,  $d_p$  is the initial diameter of droplet, and  $K$  is the evaporation constant. Eq. (2.1) shows droplet life time is proportional to the particle size. It causes two phenomena in flame front; flame thickness and flame propagation speed. For larger particles, flame thickness is thicker than that of smaller particles since it takes more time to be totally vaporized. The flame propagation speed is inversely proportional to particle size since lesser amount of outer energy is applied to ignite vapor.

## 2. Amount of Vapor for a Single Droplet

The amount of vapor is proportional to the liquid diameter since the mass transfer occurs through the surface of liquid droplet. For the view of a single droplet, under the identical condition, a larger single particle will produce more amount of vapor which is not true for actual combustion process.

In actual combustion process, multi-droplets of fuel liquid should be considered. When flame propagates, sufficient amount of vapor from droplets that can sustain flame is essential. As mentioned above, surface area is the key factor that affects the mass transfer of vapor for an identical liquid and temperature. For a single particle, it is

mentioned that larger particle produces more vapor. But for multi-droplet condition, the total surface area should be considered instead of the surface area of one single particle. Figure 2.3 shows the normalized surface area ratio with respect to a single particle when it breaks up into smaller particles having the same liquid volume. In Fig. 2.3, the initial droplet diameter is 1 cm and breaks up into 10 million particles having  $d_{p, \text{final}} = 46 \mu\text{m}$ . At this state, the total surface area is about 200 times larger than that of initial single

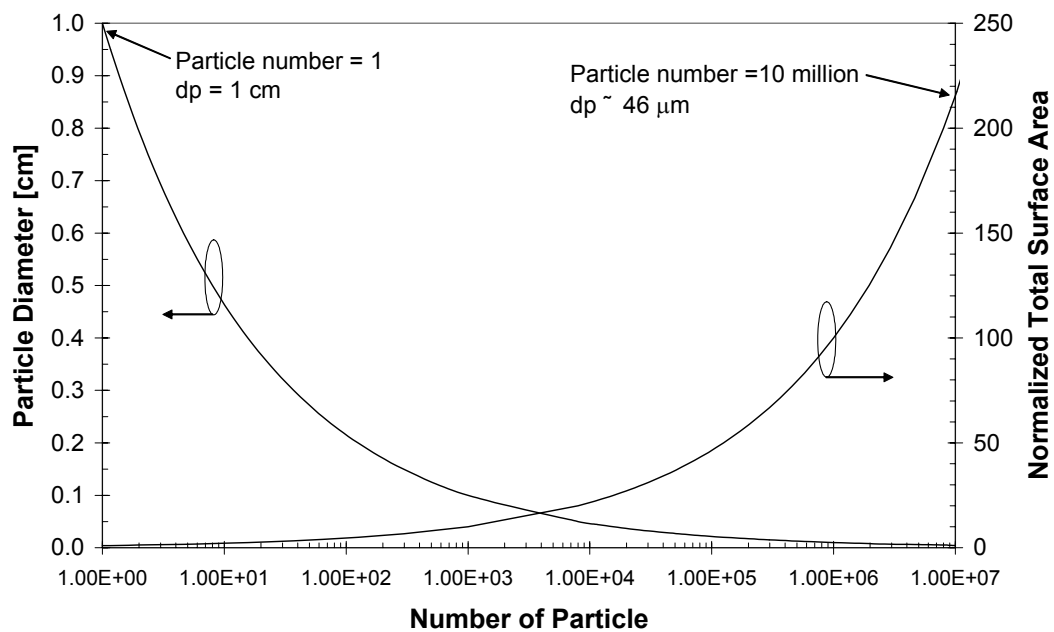


Fig. 2.3. Total surface area ratio with respect to number of particles when a single initial droplet diameter of 1cm breaks into smaller particles having the identical liquid volume.

droplet. Figure 2.3 clearly shows that smaller particles for a given volume can produce enough amount of vapor within a given time resulting in more favorable conditions of flame sustain and propagation. On the other hand, the speed of flame propagation of

larger particle become slower since lesser energy from outer source is used for overcoming activation energy of droplet since most part of energy is used for vaporizing liquid droplets. The fundamentals on flame structure and propagation are well explained by Fristrom (1995), Frohn and Roth (2000), and Turns (2000).

Flame propagation has been studied intensively and extensively. Burgoyne and Cohen (1954) developed a suspension of controlled uniform droplet size (7  $\mu\text{m}$  to 55  $\mu\text{m}$ ) from pure flammable liquid and investigated the flammability and flame propagation speed as a function of particle size. Their results shown in Fig. 2.4 indicate that below 10  $\mu\text{m}$  suspension behaves like a vapor and above 30  $\mu\text{m}$  drops burn individually which is explained in previous section. They postulated flame speed enhancement, or transition region, that occurs at the particle range of 10  $\mu\text{m}$  and 30  $\mu\text{m}$ . In this region, the flame speed is faster than that of a vapor. There was a controversial in this postulate since experimental conditions, air/fuel ratio and liquid droplet/vapor ratio, were not consistent during experiments at that time.

The postulate of Burgoyne and Cohen (1954) has been investigated by several researchers. Polymeropoulos (1984) numerically studied flame enhancement region and showed a good agreement. Chan and Jou (1988) investigated experimentally and showed the transition region. A condensation aerosol generator was applied and produced mono-disperse aerosol particle of Tetralin with droplet range of 8 - 50  $\mu\text{m}$ . Chan and Wu (1989) proposed numerical model based on their previous result. Bowen and Cameron (1999) reviewed theoretical, experimental and computational approaches relating aerosol explosions. They emphasized the importance of study of aerosol explosions as a function

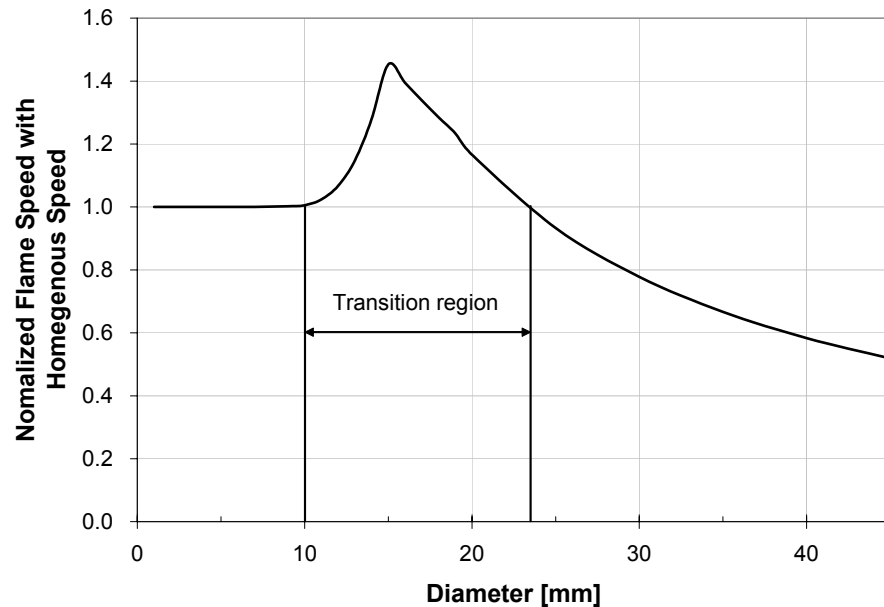


Fig. 2.4. Flame propagation speed as a function of particle diameter (Burgoyne and Cohen., 1954).

of droplet size. Cameron and Bowen (2001) developed the fixed volume chamber that can generate mono-disperse particle range of 5  $\mu\text{m}$  -15  $\mu\text{m}$  under the same Air/Fuel ratio. This kind of chamber offers opportunity to verify the proposition of Burgoyne and Cohen (1954). Although the reason of enhancing flame propagation at the transition region is not clearly known, it is clear that the mist having transition range of particles can cause more devastating results than that of vapor since the speed of flame propagation of mist is faster than that of vapor.

From above reviews, it is clear that the particle size has critical role in flame propagation of liquid droplet. In order to have knowledge on the flame behavior of a mist formed by HTFs, their characteristics of aerosol formation should be well defined.



### 2.3 Atomization Process

The transformation of bulk liquid into sprays and other physical dispersions of small particles in a gaseous atmosphere is called as the atomization. It has a significant role in different kinds of interesting areas, such as combustion and manufacturing industries, safety process for extinguishing fire, medicine for spray-type products, and so on.

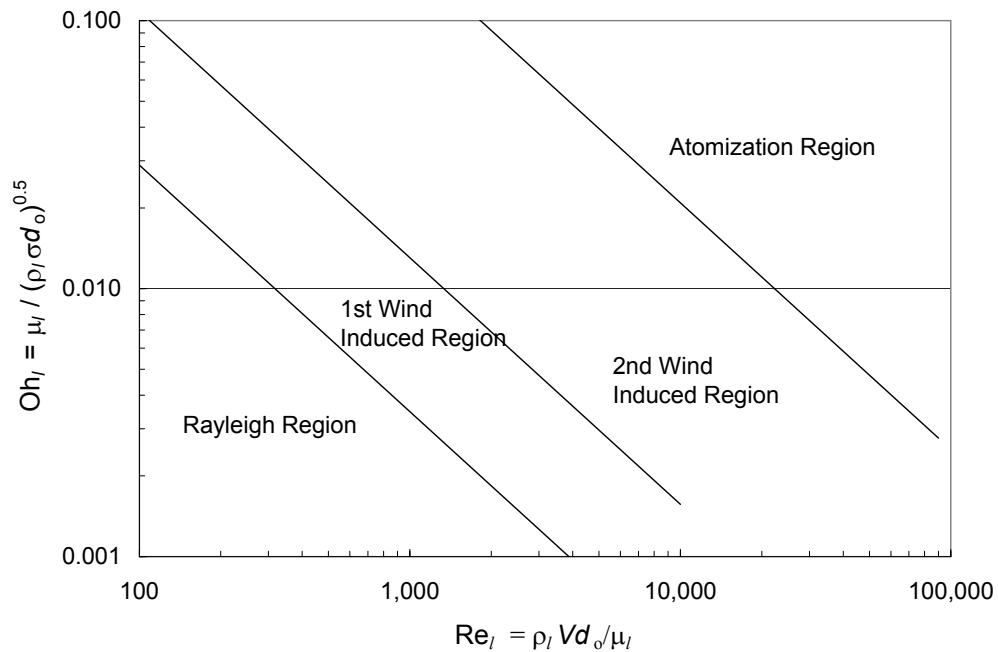
There are several analysis parameters, such as liquid break up length, break up regimes, and atomized droplet size depending on its area of interest. As the principle of flame propagation is discussed in previous section, an atomized particle size is the most important parameter on flame behavior of liquid droplets. The study of atomization process has focused on the parameters that decide atomized particle size. Several interacting mechanisms have been found to understand atomization process. Flüsener (1933) set up the relation between internal droplet pressure and ambient pressure and surface tension pressure. He showed that atomized particle size is proportional to surface tension. Hinze (1955) experimentally showed three deformation processes of atomization and introduced the relationship between aerodynamic stress and viscous stress. He showed that the atomized particle size is inversely proportional to aerodynamics and proportional to viscous stress.

Ohnesorge (1936) proposed the most commonly quoted criteria for classifying jet disintegration depending upon the conditions of stability and instability of process. Ohnesorge number,  $\mu_l / \sqrt{\rho_l \sigma d}$ , followed his name and expressed by two well known non-dimensional numbers, Reynolds and Weber number, explains the characteristics of

atomization. In his analysis, the breakup of atomization with higher Ohnesorge number easily occurs since the process becomes more instable condition, where atomized droplet tends to be smaller, than that of lower Ohnesorge number.

When a liquid jet emerges from a nozzle as a continuous body of a cylindrical form, the competition set up on the surface of the jet between the cohesive and disruptive forces gives rise to oscillations and perturbations. Under certain conditions, liquid jets disintegrate into smaller droplets or remain as larger droplets. Ohnesorge (1936), Miesse (1955), and Reitz (1978) explained disintegration regimes by Ohnesorge number ( $Oh$ ) and Reynolds number ( $Re$ ). Figure 2.5 shows four regimes of atomization process and their characteristics showing the classification of modes of disintegration as a function of  $Oh$  and  $Re$  and their characteristics. Figure 2.5-a explains the behavior of atomization process. At the higher  $Oh$  where the liquid jet is the unstable condition (highly oscillated and perturbed status), lower inertia (lower  $Re$ ) is needed for liquid jet to reach atomization regime where finer droplets are produced. On the other hand, the liquid jet of lower  $Oh$  condition needs higher inertia (higher  $Re$ ). Figure 2.5-b explains their description and droplet formation mechanism. Figure 2.6 shows the images of liquid disintegration of water. The images are recorded by high-speed CCD at 500 frames per second. In Reyleigh- and 1<sup>st</sup> wind induced-regimes, the surface tension force is dominant producing relatively larger particles than the size of nozzle orifice. In 2<sup>nd</sup> wind induced- and atomized-regimes, dynamic force becomes dominant resulting in the formation of finer particles. In this research, 2<sup>nd</sup> wind induced breakup- and atomization-

regimes are of interest domain since the formation of mist can form under these conditions.



(a) Classification of modes of disintegration

Regime	Description	Drop Formation Mechanism
1	Rayleigh breakup	Surface tension force
2	First wind-induced breakup	Surface tension force; dynamic pressure of ambient air
3	Second wind-induced breakup	Dynamic pressure of ambient air opposed by surface tension force initially
4	Atomization	Unknown

(b) Characteristics

Fig. 2.5. Classification of disintegration modes and their characteristics (Reitz, 1978).

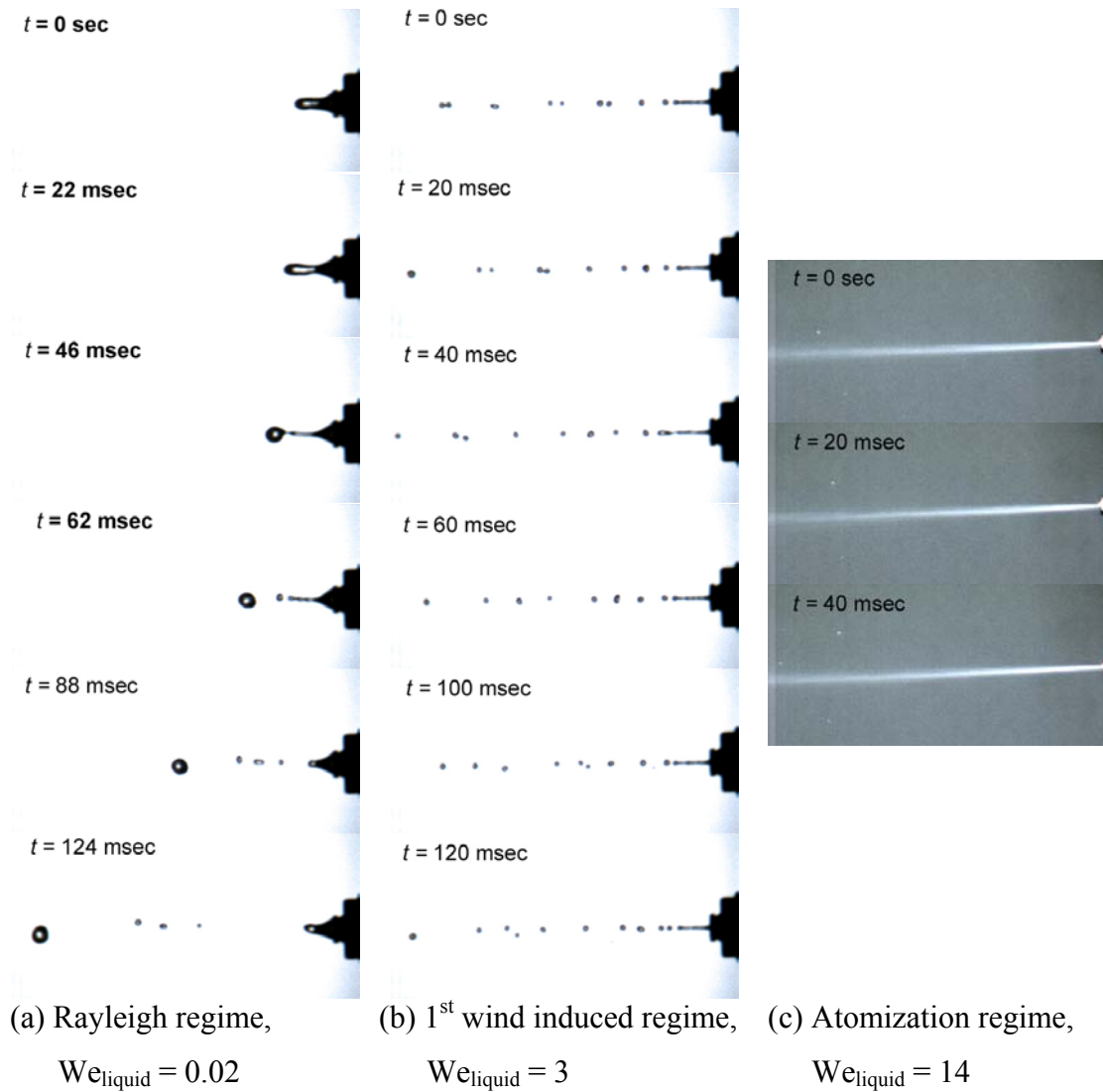


Fig. 2.6. Images of three liquid disintegration processes recorded by high-speed CCD camera at 500 frames per second (nozzle diameter is 0.33 mm for all three cases).

## 2.4 Aerosol Particle Distribution

The size distribution of an aerosol can be modeled by the analytical functions based on statistical analysis on empirical data. Rosin and Rammler (1933) proposed the most widely used expression for coarsely dispersed dusts and spray drop size distribution. Rosin-Rammler model is the two parameter model that can predict aerosol particle distribution using two independent parameters as

$$Q = 1 - \exp\left[-(d_p / X)^q\right] \quad (2.2)$$

where  $Q$  is the normalized weight fraction below the particle size,  $d_p$ , and  $X$  and  $q$  are constants which are determined empirically. In Eq. (2.2), the  $X$  responds approximately with the peak of the weight frequency distribution and the  $q$  indicates the width of distribution. In Eq. (2.2), large  $q$  gives narrow distribution and vice versa. Figure 2.7 shows the effect of varying  $q$  value. In Fig. 2.7,  $X$  is 40  $\mu\text{m}$ .

The representative diameters have been applied since it is convenient to work only with mean or average diameters instead of the complete drop size distribution. Mugele and Evans (1951) generalized the concept of mean diameter as following;

$$D_{ab} = \left[ \frac{\sum N_i D_i^a}{\sum N_i D_i^b} \right]^{1/(a-b)} \quad (2.3)$$

where  $a$  and  $b$  are any values corresponding to the effect investigated,  $i$  donates the size range considered,  $N_i$  is the number of drops in size range  $i$ , and  $D_i$  is the middle of diameter of size range  $i$ . Table 2.2 (Lefebvre, 1989) shows some mean diameters and their applications. In Table 2.2, Sauter Mean Diameter (SMD) that represents the ratio of the total volume to the total surface area of all droplets in the test set will be applied in

this research since it is suitable for the study of flame propagation related with mass transfer.

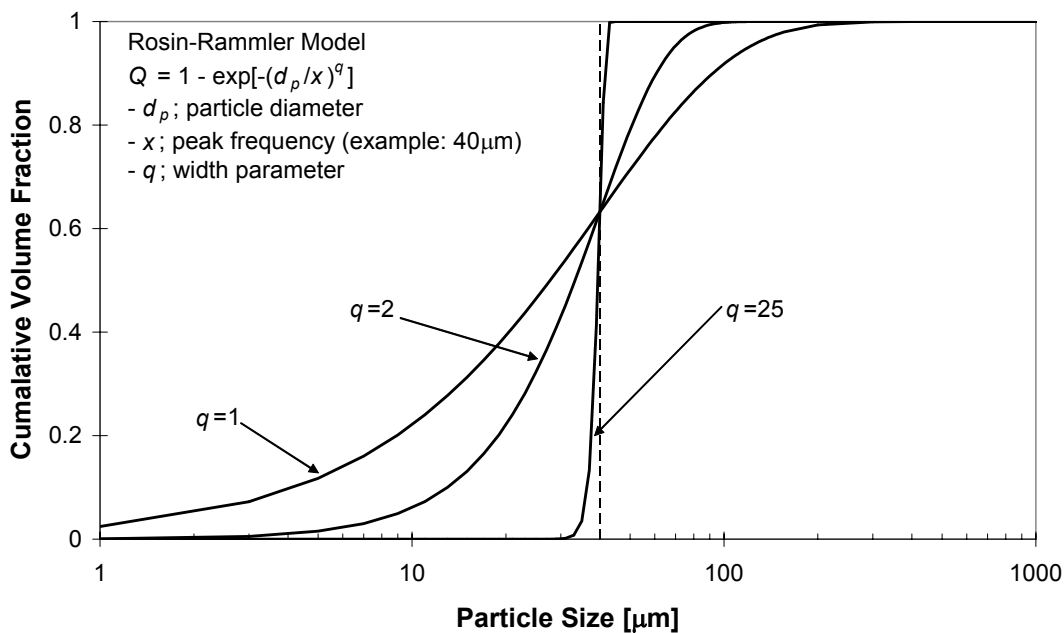


Fig. 2.7. Different aerosol particle distribution by Rosin-Rammler analytical model with different values of the constant  $q$  ( $x = 40 \mu\text{m}$ ).

## 2.5 Particle Size Measurement

There are several methods of measuring an aerosol particle size. Optical sizing measurement is the one of the methods and has beneficence since it is the non-intrusive and real-time-based method. The fundamental principle of several optical methods is well explained by Hirleman et al. (1990), Hirleman (1994), and Koo and Hirleman (1996).

Table 2.2

Examples of mean diameters and applications (Lefebvre, 1989)

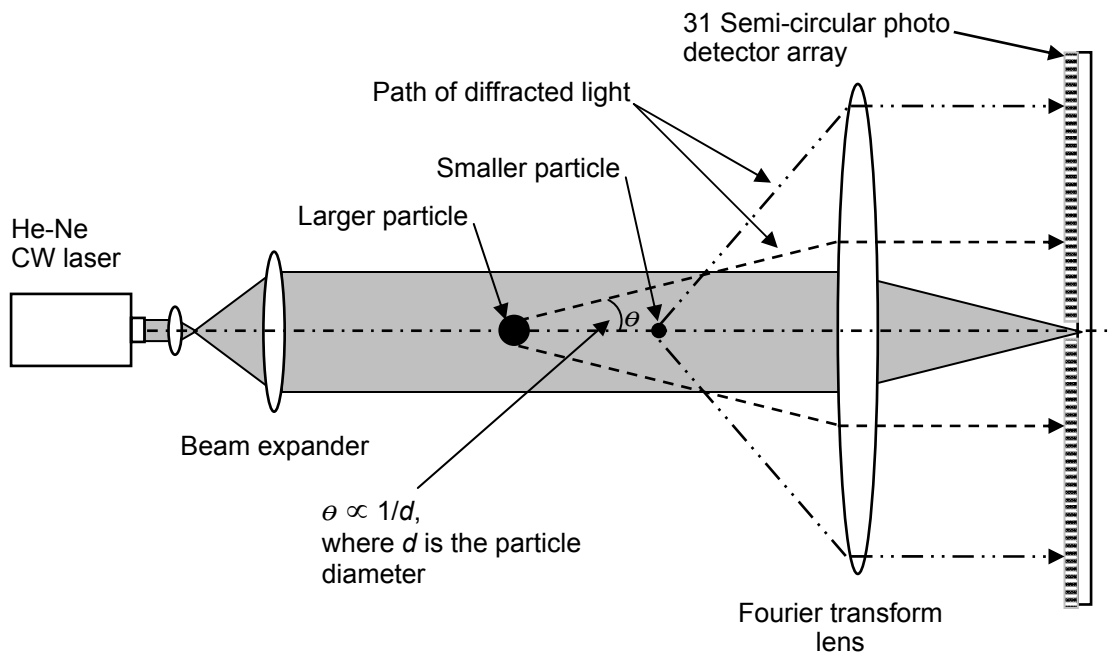
a	b	a+b (order)	Symbol	Name of Mean Diameter	Expression	Application
1	0	1	$D_{10}$	Length	$\frac{\sum N_i D_i}{\sum N_i}$	Comparisons
2	0	2	$D_{20}$	Surface Area	$\left(\frac{\sum N_i D_i^2}{\sum N_i}\right)^{1/2}$	Surface Area Controlling
3	0	3	$D_{30}$	Volume	$\left(\frac{\sum N_i D_i^3}{\sum N_i}\right)^{1/3}$	Volume Controlling
2	1	3	$D_{21}$	Surface Area-length	$\frac{\sum N_i D_i^2}{\sum N_i D_i}$	Absorption
3	1	4	$D_{31}$	Volume-length	$\left(\frac{\sum N_i D_i^3}{\sum N_i D_i}\right)^{1/2}$	Evaporation, Molecular Diffusion
3	2	5	$D_{32}$	Sauter (SMD)	$\frac{\sum N_i D_i^3}{\sum N_i D_i^2}$	Mass Transfer, Reaction
4	3	7	$D_{43}$	De Brouckere or Herdan	$\frac{\sum N_i D_i^4}{\sum N_i D_i^3}$	Combustion Equilibrium

Malvern Instrument Ltd. utilized the application of Fraunhofer diffraction theory to measure drop size initiated by Swithenbank et al. (1977) and has intensively developed devices. Figure 2.8 schematically illustrates the applied principle and shows its photo detector. When a collimated laser beam passes through particles, it is diffracted. The angle of diffraction is inversely proportional to diameter of particles. The diffracted rays hit the detector where semi circular photo diode arrays are located.

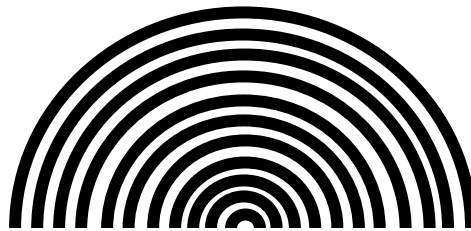
The collected data containing an aerosol particle size distribution is converted into the form of light intensity distribution and is sent to computer for analysis. A computer calculates an initial size distribution from which it constructs the corresponding light energy distribution. This ‘calculated’ distribution is then compared with the measured distribution. This method, a least squares technique, repeats until the best fitting particle size distribution is obtained. When the final result of particle size distribution is obtained, its accuracy is shown as the least squares fitting parameter. More detail description on the least squares fitting parameter will be introduced in Chapter IV.

There are numerous numbers of applications of Malvern system. Kihm et al. (1995) experimentally investigated droplet-size characteristics of DF-2 fuel near the spray tip of intermittent sprays of diesel fuel using Malvern system. They established the predicted atomized particle size of DF-2 using correlation between injecting pressure, gas density, and axial distance from the tip. Sukmarg et al. (2002) investigated the formation behavior of one of HTFs, alkylated aromatic. They also utilized Malvern





(a) The principle of diffraction



(b) 31 semi-circular ring diodes in detector (front view)

Fig. 2.8. Fraunhofer diffraction particle size analyzer; Malvern system (the light diffracted by smaller particle have larger diffracted angle. Without particles, collimated beam will focus into center ring diode).

system and measured the particle size distribution as a function of temperatures, injecting pressures, and distance from the nozzle orifice.

## 2.6 Atomization Analysis on Empirical Data

Without proper interpretation on empirical data, this data is difficult in readable form. Dimensional analysis (Buckingham, 1915) provides a strategy for choosing a relevant data and how it should be presented. This is a useful technique in all experimentally based areas of engineering. If it is possible to identify the factors involved in a physical situation, dimensional analysis can form a relationship between them.

To apply dimensional analysis to atomization process, the physical factors discussed in previous section need to be setup. These parameters are

$$d = f(d_o, x, V, \sigma, \mu_l, \mu_g, \rho_l, \rho_g) \quad (2.4)$$

where  $d$  [L] is the atomized mean droplet diameter (SMD),  $d_o$  [L] is the nozzle orifice diameter,  $x$  [L] is the axial distance from the nozzle orifice,  $V$  [L/T] is the initial velocity of the liquid at nozzle orifice,  $\sigma$  [L/T<sup>2</sup>] is the liquid surface tension,  $\mu_l$  [M/LT] is the dynamic liquid viscosity,  $\mu_g$  [M/LT] is the dynamic ambient gas viscosity,  $\rho_l$  [M/L<sup>3</sup>] is the atomized liquid density, and  $\rho_g$  [M/L<sup>3</sup>] is the ambient gas density. Brackets indicate dimension of parameters: L (Length), T (Time), and M (Mass).

From Buckingham pi theorem, 6 pi groups can be formed by power products since there are 9 variables and three dimensions. In this research,  $d_o$ ,  $V$ , and  $\rho_g$  are designated as repeating variables. The final form of correlation is set up as

$$\frac{d}{d_o} = Cont. (We_g)^{e1} (Re_l)^{e2} \left(\frac{\mu_l}{\mu_g}\right)^{e3} \left(\frac{\rho_l}{\rho_g}\right)^{e4} \left(\frac{x}{d_o}\right)^{e5} \quad (2.5)$$

where all parameters except  $d$  are known values under given experimental conditions and  $d$  will be measured during experiments. One constant and five exponents can be obtained using a regression method of statistics. Eq. (2.5) will be applied to research as an analysis tool. Details on procedures about Buckingham pi theorem for establishing final form of correlation are explained in the Appendix A.

## CHAPTER III

### EXPERIMENTAL CONDITIONS AND SETUP

Chapter III shows experimental setups for characterizing atomization process of HTFs and explains experimental setup conditions: temperature, injecting pressure, and orifice nozzle diameter.

#### 3.1 Test Heat Transfer Fluids

Six different HTFs which are most widely and commonly used in process industries are investigated. Table 3.1 shows their characteristic temperatures and range of use. To change fluid properties which affect the formation of liquid particles, three experiment temperatures for each fluid are established based on their flash points. For the safety purpose, the established highest temperature condition for each fluid has been setup as 90% (with respect to absolute temperature) of its flash point. Table 3.2 shows experimental conditions of temperature.

To establish correlations, physical properties of fluid (density, viscosity, and surface tension) as a function of temperature are needed for analyzing empirical results. Data on density and viscosity variations with temperature are obtained from manufacturers or Material Safety Data Sheets (MSDS). Figures 3.1 - 3.2 show the variations of density and viscosity with temperature. Interpolations have been applied to each fluid to define correlations as a function of temperature. Table 3.3 shows the results

Table 3.1  
Characteristic temperature of Heat Transfer Fluids

Fluids \ Temperature	Flash Point [ °C ]	Fire Point [ °C ]	Auto Ignition [ °C ]	Range of Use [ °C ]
Alkylated Aromatic (AAR)	177 <sup>(a), (b)</sup>	218 <sup>(a), (b)</sup>	343 <sup>(c)</sup>	-25 – 290
Bi-/Di-phenyl Oxide (BDP)	124 <sup>(a), (b)</sup>	127 <sup>(a), (b)</sup>	612 <sup>(d)</sup>	12 – 400
Diaryl Alkyl (DAL)	194 <sup>(a), (c)</sup>	206 <sup>(a), (b)</sup>	385 <sup>(c)</sup>	0 – 350
Di-/Tri-aryl Compounds (DTA)	124 <sup>(a), (c)</sup>	128 <sup>(a), (b)</sup>	584 <sup>(c)</sup>	29 – 371
Modified Terpenyl Oxide (MTO)	184 <sup>(a), (b)</sup>	212 <sup>(a), (b)</sup>	373 <sup>(c)</sup>	0 – 345
White Mineral Oil (WMO)	171 <sup>(a), (b)</sup>	196 <sup>(a), (b)</sup>	366 <sup>(d)</sup>	-25 – 316

<sup>(a)</sup> The American Society For Testing and Materials (ASTM) D-92

<sup>(b)</sup> Cleveland Open Cup (COC) Method

<sup>(c)</sup> ASTM E-659

<sup>(d)</sup> ASTM D-2155

<sup>(e)</sup> Pensky-Martens Closed Tester (PMCC) Method

Table 3.2

Established experimental temperature conditions

Condition	AAR			BDP		
	Experiment temperature	Ratio* with flash point (177 °C)	Ratio* with fire point (218 °C)	Experiment temperature	Ratio* with flash point (124 °C)	Ratio* with fire point (127 °C)
# 1	80 °C	0.78	0.72	50 °C	0.81	0.76
# 2	100 °C	0.83	0.76	70 °C	0.86	0.81
# 3	120 °C	0.87	0.80	90 °C	0.89	0.84
	DAL			DTA		
	Experiment temperature	Ratio* with flash point (194 °C)	Ratio* with fire point (206 °C)	Experiment temperature	Ratio* with flash point (124 °C)	Ratio* with fire point (128 °C)
# 1	90 °C	0.78	0.77	50 C	0.81	0.71
# 2	110 °C	0.82	0.81	70 C	0.86	0.86
# 3	130 °C	0.86	0.85	90 C	0.91	0.91
	MTO			WMO		
	Experiment temperature	Ratio* with flash point (184 °C)	Ratio* with fire point (212 °C)	Experiment temperature	Ratio* with flash point (171 °C)	Ratio* with fire point (196 °C)
# 1	95 °C	0.81	0.76	90	0.82	0.57
# 2	120 °C	0.86	0.81	110	0.86	0.60
# 3	135 °C	0.89	0.84	130	0.91	0.63

\* Ratio is calculated based on absolute temperature.

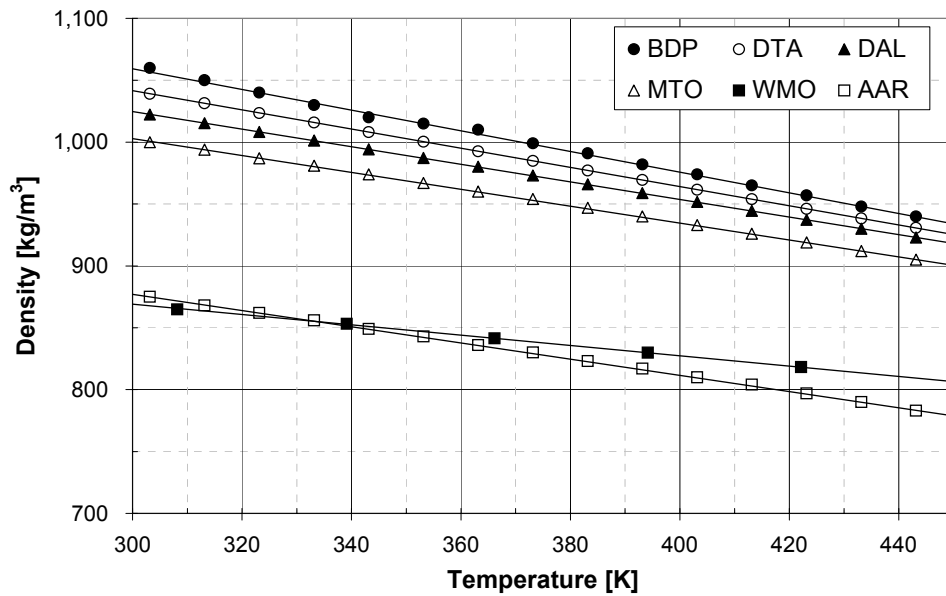


Fig. 3.1. Properties of density variation of six Heat Transfer Fluids as a function of temperature.

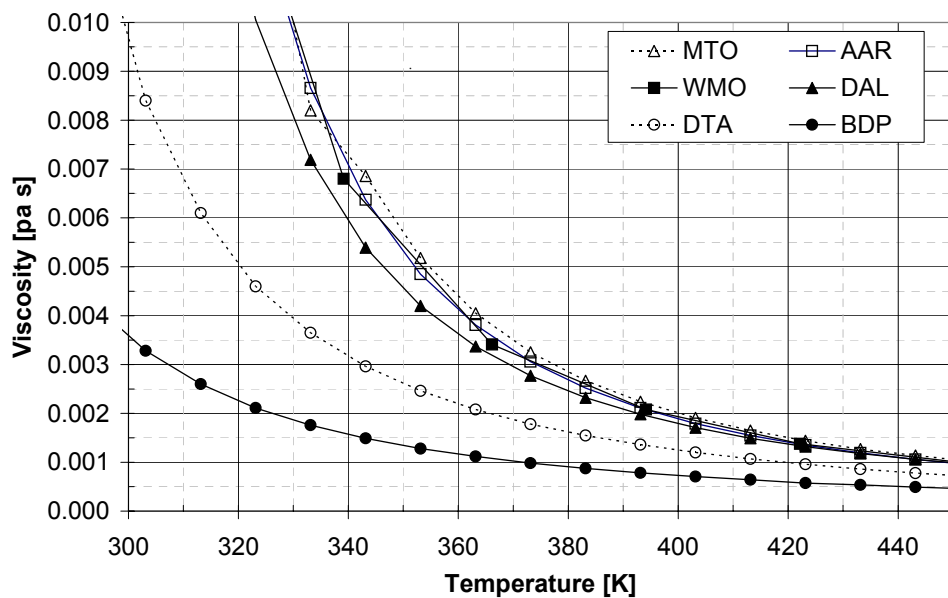


Fig. 3.2. Properties of viscosity variation of six Heat Transfer Fluids as a function of temperature.

Table 3.3

Correlated properties of Heat Transfer Fluids as a function of temperature

Property	Density [kg/m <sup>3</sup> ]		Viscosity [Pa · s]			Surface Tension [N/s]	
Equation	$d1 \times T + d2$		$v1 \times (T)^{v2} + v3$			$s1 \times T + s2$	
Variable	$d1$	$d2$	$v1$	$v2$	$v3$	$s1$	$s2$
AAR	-0.6511	1073.3	$2 \times 10^{15}$	-6.9315	0.00010	-0.00009	0.0573
BDP	-0.8379	1311.1	$2 \times 10^{10}$	-5.1838	0.00007	-0.00008	0.0560
DAL	-0.7103	1237.7	$3 \times 10^{13}$	-6.2399	0.00009	-0.00010	0.0713
DTA	-0.7748	1274.0	$8 \times 10^{11}$	-5.6838	-0.00010	-0.00010	0.0710
MTO	-0.6857	1209.4	$7 \times 10^{14}$	-6.7336	0.0	-0.00009	0.0656
WMO	-0.4167	994.2	$8 \times 10^{11}$	-5.6182	0.0	-0.00007	0.0510

of interpolations. The overall error of correlated density and viscosity as a function of temperature with respect to obtained data is  $\pm 0.5\%$  and  $\pm 8\%$ , respectively.

Since data on viscosity of some HTFs are not sufficient and available from manufacturers or MSDS, they have been measured using Fisher Surface Tensiomat, Model 20. The details on measurement in surface tension are described in the Appendix B. Figure 3.3 shows the result of measurements on surface tension. To make sure of measurement accuracy, distilled water whose property is well known has been measured. The overall error with respect to known data is less than 5.5%. Table 3.3 also shows the correlation result of viscosity as a function of temperature.



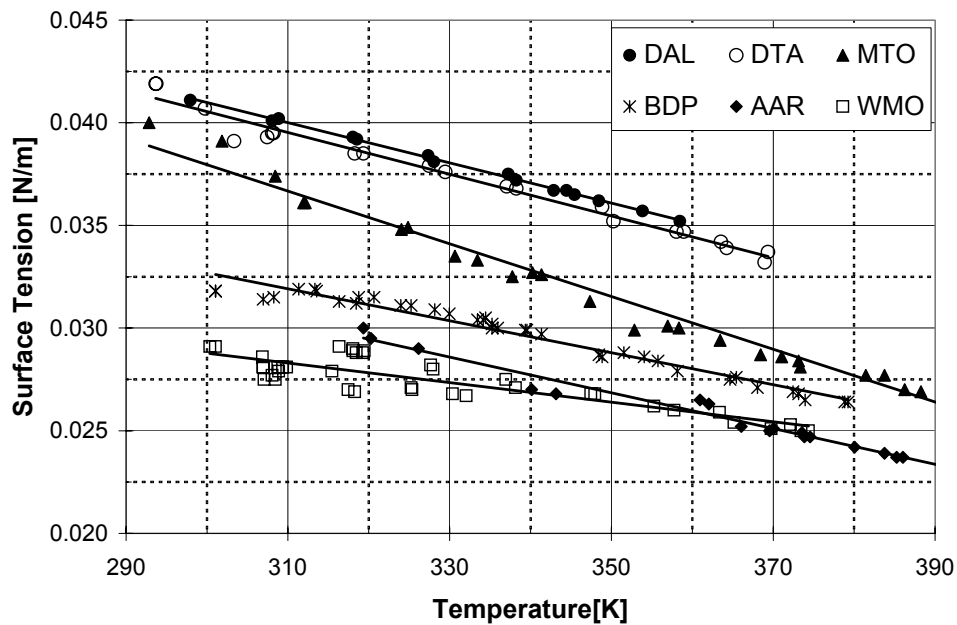


Fig. 3.3. Result of measurement on the surface tension of six Heat Transfer Fluids.

## 3.2 Experimental Setup

### 3.2.1 General Description of System

The applied method of atomization to simulate HTFs leakage resulting mist formation is a plain-orifice nozzle. Figure 3.4 shows the general apparatus of experimental setup applied in this research. It consists of 4 subsystems: atomization, temperature control, collection & exhaust, and Malvern-system.

The atomization system has a nitrogen tank, fluid delivery pipe system, and fluid cell. The fluid cell is a 5.9 liter aluminum cylinder and positioned on the two dimensional positioning mount which offers varying and adjusting the investigated

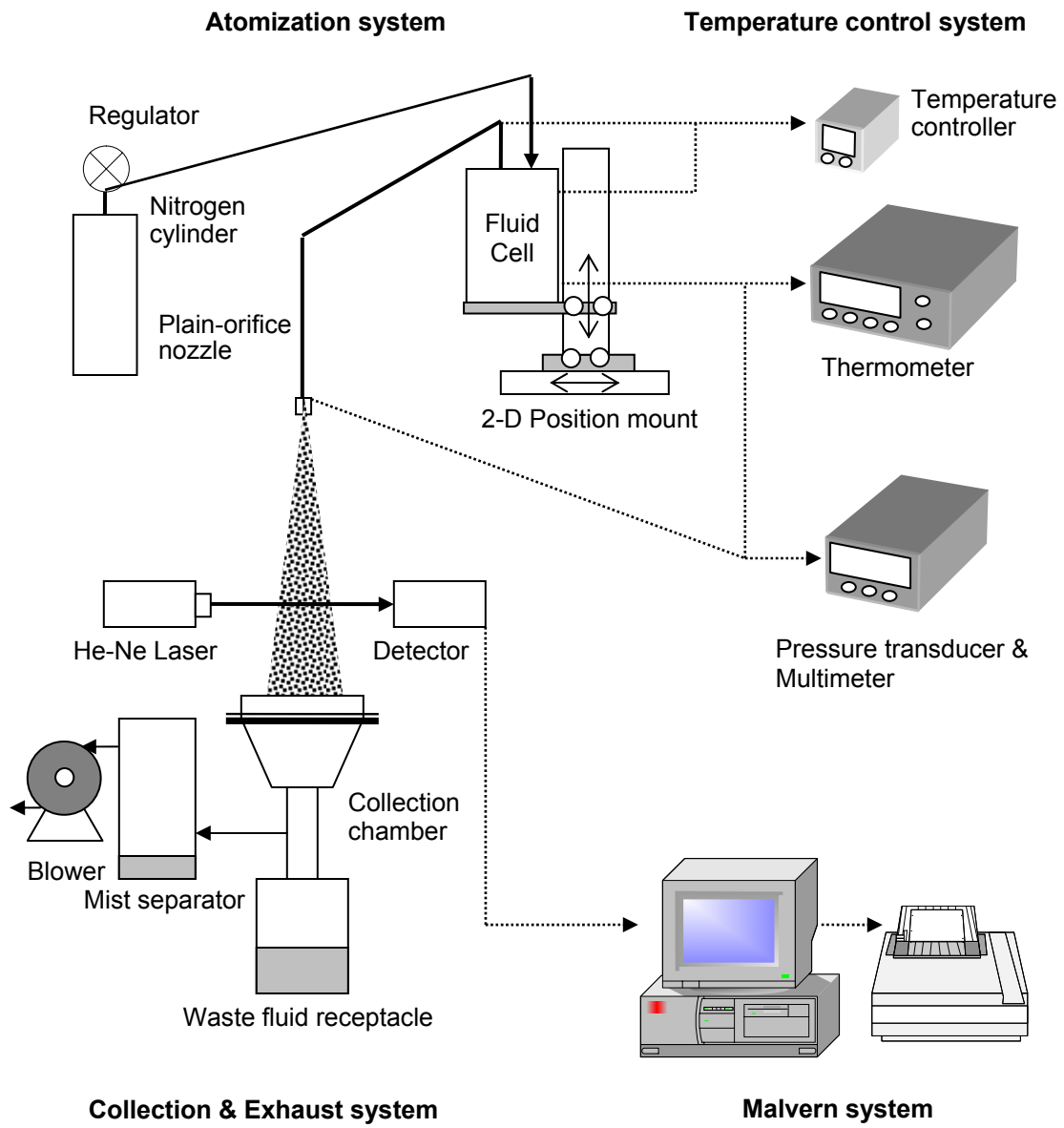


Fig. 3.4. Experimental setup.

location. The applied plain-orifices are drilled into brass plugs. The details of nozzle will be discussed in following section.

Temperature control system consists of temperature controller, thermometer, pressure transducer & multimeter, and heat strips. Heat strips controlled by temperature controller, Omega CN76000, wrap the fluid cell and fluid delivery pipe system. In order to maintain a stable temperature condition, insulation materials are applied. Fluid temperatures are read at fluid cell and nozzle by thermometer, Omega DP80, and recorded by multimeter digital scanner, Keithley 2000. The injection pressure is converted into electric signal by transducer. The calibration for correlation between injecting pressure and generated electric signal has been conducted.

The collection & exhaust system consists of collection chamber, fluid waste receptacle, mist separator, and blower. For the safety purpose during experiments, the mist separator and the explosion proof blower are applied. The mist separator removes aerosol larger than the particle size of 5  $\mu\text{m}$ . The suction line that connects the blower and the separator is anti-static plastic pipe.

### **3.2.2 Plain-Orifice Nozzle**

Three different diameters of plain-orifice nozzles are applied to simulate leakage of HTFs under different conditions of temperatures and injecting pressures. Figure 3.5 shows the diagram of applied plain-orifice nozzles and nozzle diameters used in this research.

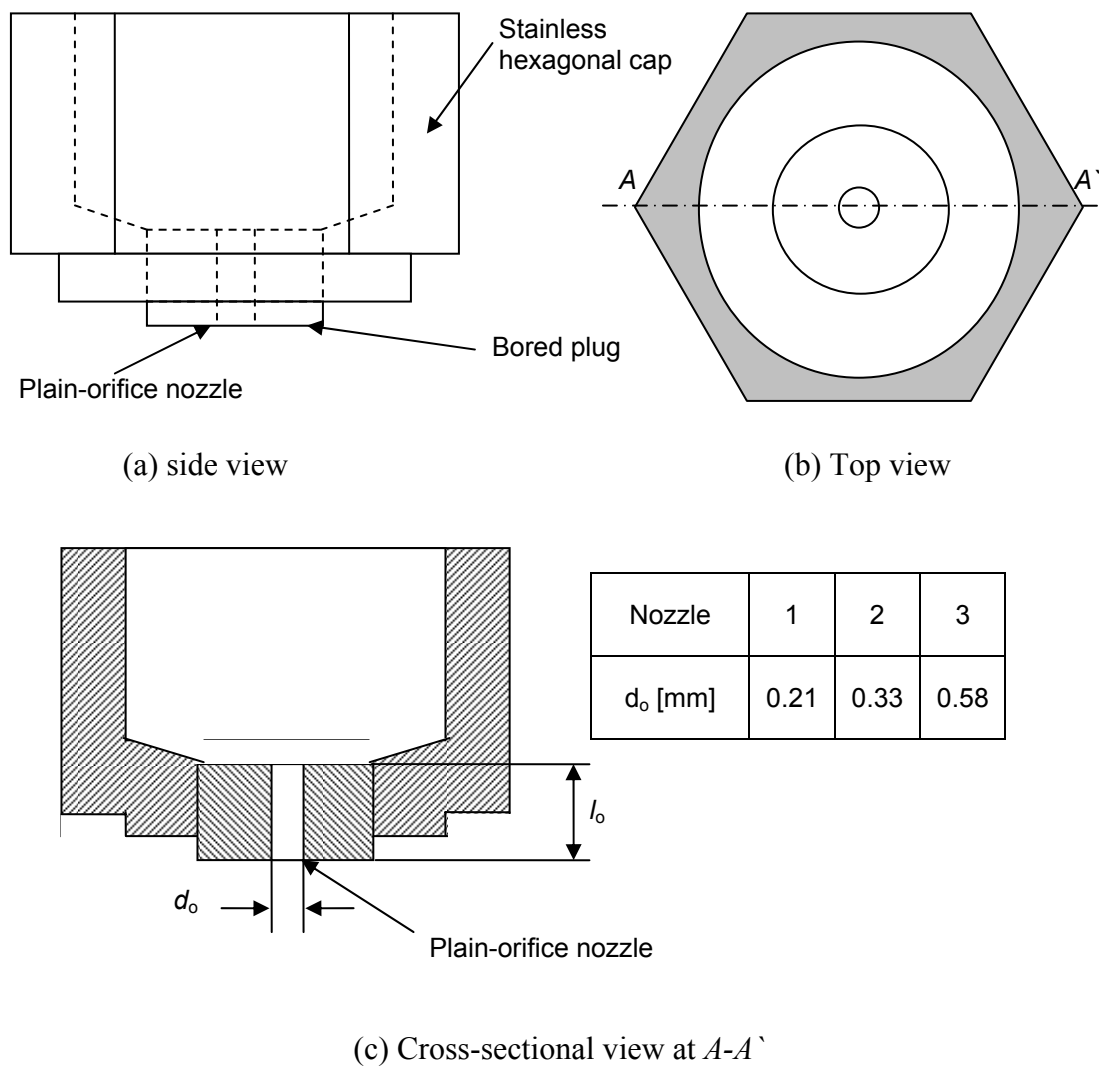


Fig. 3.5. Apparatus of plain-orifice nozzle (table shows the fabricated nozzle diameters.).

To achieve correlations, actual nozzle velocities should be known. Nozzle exit velocity of fluids, however, is function of the shape of inside nozzles since there is a pressure loss incurred in the nozzle passages and geometric configuration of nozzle throat. The actual exiting liquid velocity can be calculated by following relations;

$$V_{actual} = C_D V_{theory} \quad (3.1)$$

where  $C_D$  is the discharge coefficient and  $V_{theory}$  is the theoretical velocity calculated by Bernoulli equation.  $V_{theory}$  is expressed as

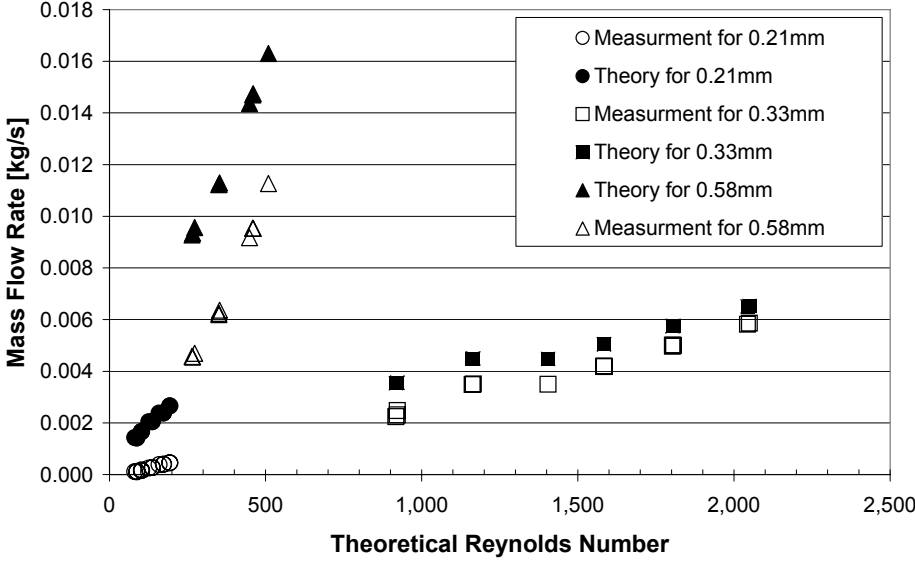
$$V_{theory} = \left( \frac{2 \Delta P}{\rho_{liq}} \right)^{0.5} \quad (3.2)$$

where  $V_{theory}$  is the theoretical velocity,  $\Delta P$  is the pressure difference between nozzle exit and ambient (gage pressure at the exit), and  $\rho_{liq}$  is the liquid density. Using Eqs. (3.1) and (3.2),  $V_{actual}$  can be obtained if  $C_D$  is known for a given experimental condition.

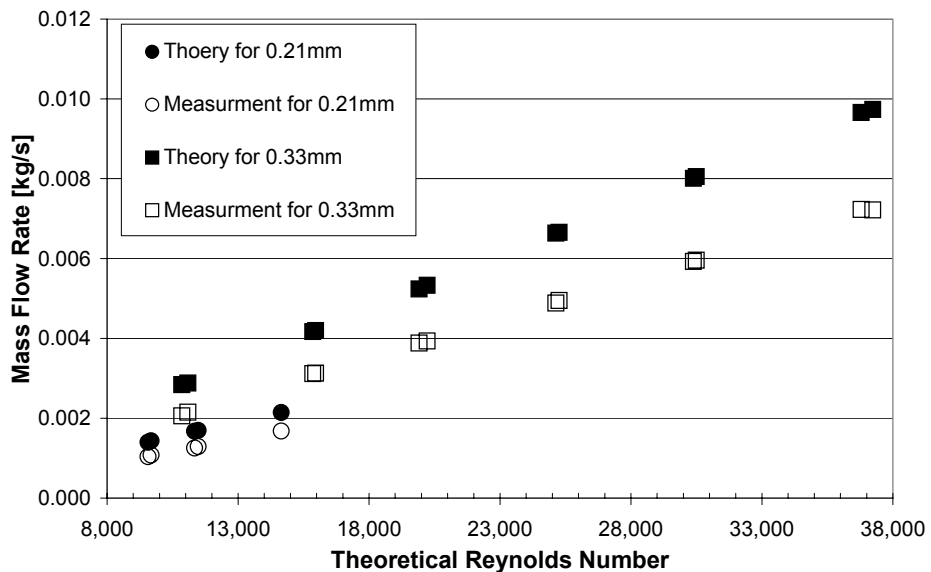
The actual mass flow rates for each nozzle have been measured under different injecting pressures in order to get  $C_D$ . Figure 3.6 shows the result of measured mass flow rate and theoretical mass flow rate ( $\dot{m}_{theory} = \rho_{liq} V_{theory} A_{nozzle}$ ) as a function of theoretical Reynolds number ( $Re_{theory} = \rho_{liq} V_{theory} d_o / \mu_{liq}$ ). Then  $C_D$  can be calculated from following relations under given  $Re_{theory}$ ;

$$C_D = \frac{\dot{m}_{measured}}{\dot{m}_{theory}} \quad (3.3)$$

Although  $C_D$  can be obtained using Eq. (3.3) under a given specific flow condition, the empirical expression for  $C_D$  is needed in order to apply to correlation of



(a) Lower Reynolds number



(b) Higher Reynolds number

Fig. 3.6. Mass flow rate as a function of Reynolds number (solid polygons indicate theoretical mass flow rate based on Bernoulli equation and blank polygons indicate actual measurement).

droplet formation. There are several empirical expressions on  $C_D$  (Nakayama and Tanida (1961), Asihmin et al. (1961), and Varde and Popa (1984)). Asihmin's (1961) correlation has been adopted since its result is well fitted to the current result of measurement. It's expressed as

$$C_D = \left[ 1.23 + \frac{58 \left( l_o / d_o \right)}{\text{Re}} \right]^{-1} \quad (3.4)$$

where  $l_o$  is the orifice length. He claimed that an accuracy is within 1.5 % for  $l_o/d_o$  in the range 2 to 5 and Re from 100 to  $1.5 \times 10^5$ . Figure 3.7 shows the comparison between measured  $C_D$  and calculated  $C_D$  by Eq. (3.4). In Fig. 3.7, the result shows the good agreement between measured- and calculated- $C_D$ . From this conclusion, Eq. (3.4) will be applied to this research. Figure 3.8 shows the  $C_D$  as a function of  $\text{Re}_{\text{theory}}$ . In Fig. 3.8, the maximum value of  $C_D$  is 0.81 for all three cases at higher Reynolds number.

### 3.2.3 Malvern System

Malvern system consists of He-Ne laser and photo detector, and computer. The He-Ne laser generates wavelength of 632.8 nm continuous light (red) with the intensity of 2mW. Current system can measure the size of particle range between 5  $\mu\text{m}$  and 550  $\mu\text{m}$ .

As the principle of measurement is explained in previous chapter, optical alignment of system is critical to ensure the accuracy of measurement. The calibration of Malvern system has been conducted whenever measurement begins in order to ensure

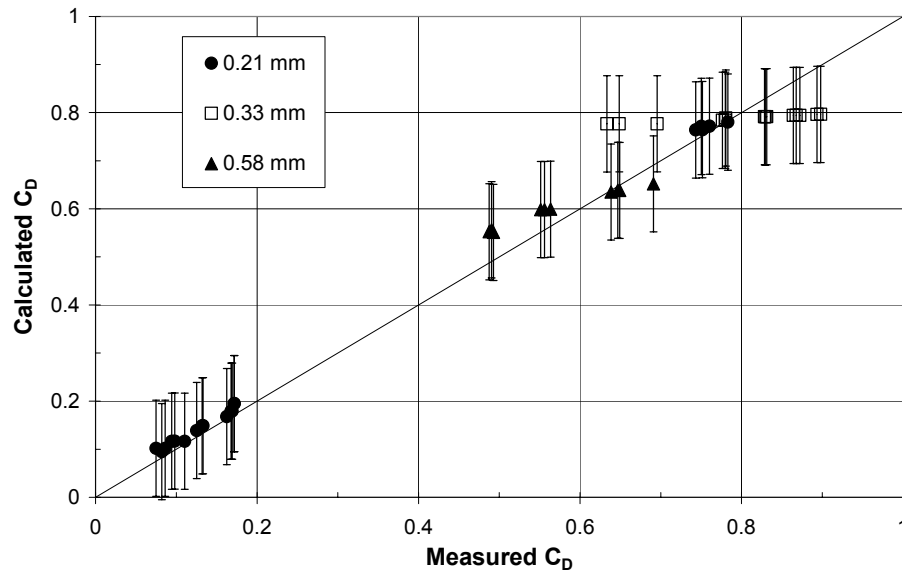


Fig. 3.7. Comparison of  $C_D$  between measurement and calculation of Eq. (3.3).

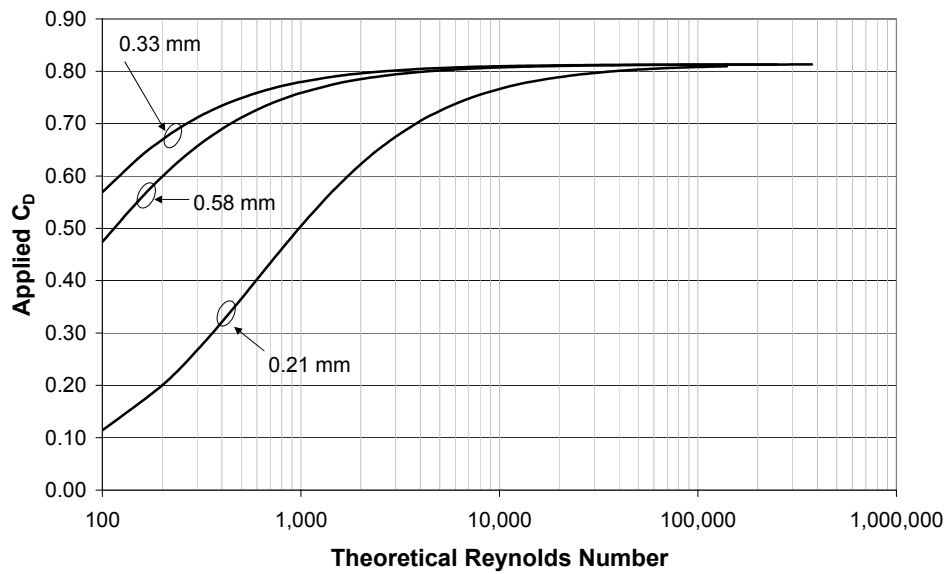


Fig. 3.8. Applied  $C_D$  for research as a function of theoretical Reynolds number.



the correct alignment of Malvern system setup. The reticle which has known solid particle size distribution on its surface is applied for the purpose of calibration. When calibration result shows big difference (more than  $\pm 3 \mu\text{m}$ ) with reference diameter (46.5  $\mu\text{m}$ ) and/or abnormal particle distribution, realignment of Malvern system has been taken until result reaches criteria mentioned above. Only when above conditions are satisfied, experiments begin. Figure 3.9 shows the particle size distribution of actual measurement result.

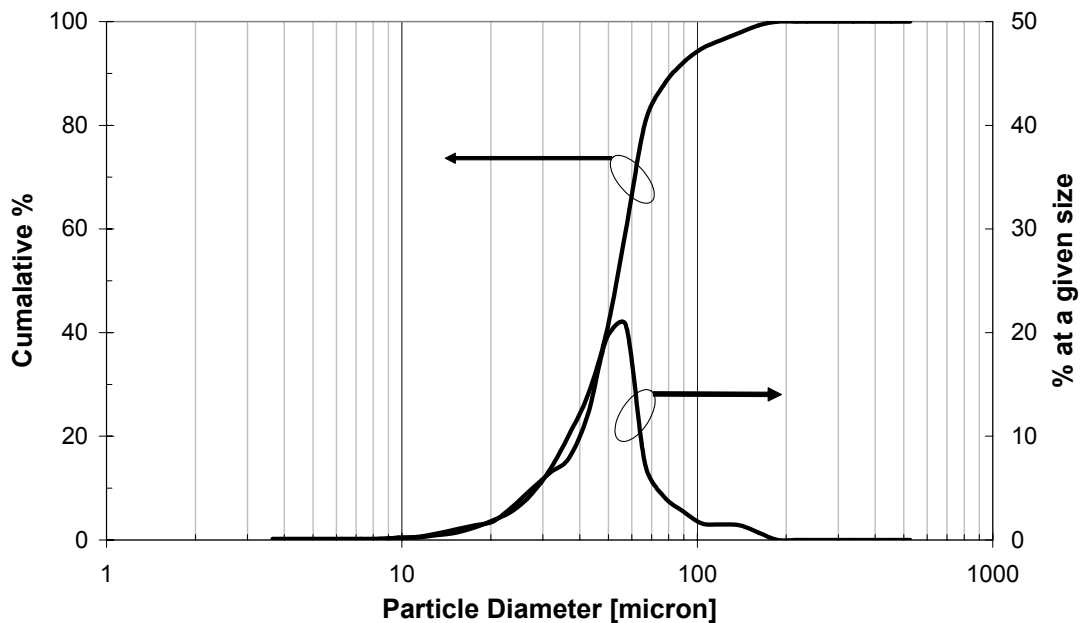


Fig. 3.9. Example of calibration result of particle distribution of reticle.

### 3.3 Experimental Conditions

To run experiments effectively, the matrix of experimental condition shown in Table 3.4 has been applied in order to change parameters that have an effect on droplet formation. By applying Table 3.4 to research, seven combinations for each fluid shown in Table 3.5 are applied. These conditions well represent different condition of atomization process and can produce effective correlation result.

Table 3.4  
Matrix for experimental condition

Parameters		1	2	3
Temperature	AAR	80 °C	100 °C	120 °C
	BDP	50 °C	70 °C	90 °C
	DAL	90 °C	110 °C	130 °C
	DTA	50 °C	70 °C	90 °C
	MTO	95 °C	120 °C	135 °C
	WMO	90 °C	110 °C	130 °C
Nozzle Orifice Diameter		0.21 mm	0.33 mm	0.58 mm
Injecting Gage Pressure		933 kPa	1,967 kPa	3,346 kPa

Table 3.5  
Combinations of seven experimental conditions

Description	Pressure	Nozzle Diameter	Temperature (in Table 3.4)
Reference Condition	1,967 kPa	0.33 mm	2
Pressure Effect	933 kPa		
	3,346 kPa		
Nozzle Diameter Effect	1,967 kPa	0.21 mm	
		0.58 mm	
Temperature Effect		0.33 mm	
	3		

## CHAPTER IV

### RESULTS AND ANALYSIS

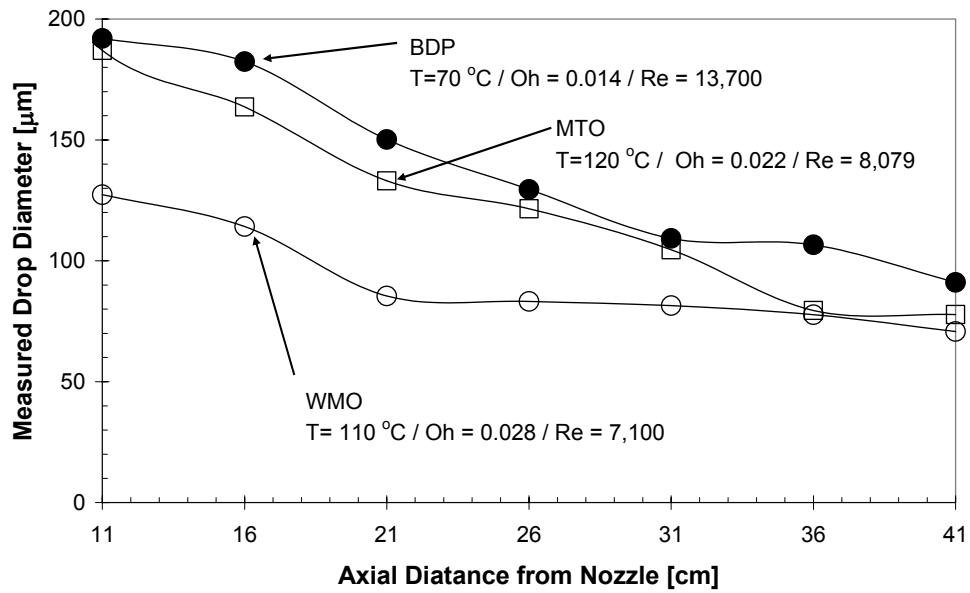
Chapter IV will discuss the result of liquid droplet formation of HFTs and their analysis. In order to interpret atomization process, disintegration of the liquid jet which was explained in Chapter II will be applied.

#### 4.1 Results and Analysis of Measurements

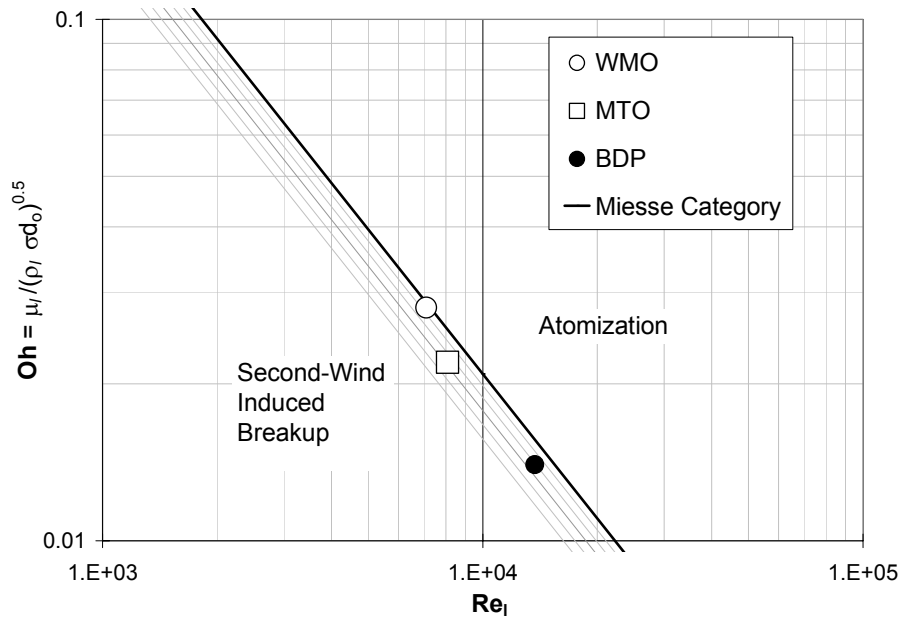
##### 4.1.1 Analysis at the Reference Condition

The analysis on a reference condition tells the effect of liquid properties on the droplet formation since the injecting pressure and the nozzle diameter for all three fluids is the identical as 1,967 kPa and  $d_o = 0.33$  mm and only temperatures which change the value of liquid properties are different depending on their experimental conditions shown in Table 3.4.

The measurement results and analysis of three HTFs at their reference conditions are shown in Fig. 4.1. Figure 4.1-a shows the result of experimental measurement. At the early stage of disintegration (shorter axial distance), the atomized droplet sizes of WMO are smaller than two other fluids and those of BDP and MTO show similar size distribution of larger particles. At the last stage of atomization, particle diameters of all three have similar sizes.



(a) Measured droplet SMD



(b) Disintegration regime of tested fluids

Fig. 4.1. Measurement result and analysis on three Heat Transfer Fluids at their reference condition.

As the effect of properties on atomization was mentioned in Chapter II, particle size is proportional to liquid surface tension and viscosity and is inversely proportional to liquid density. The comparisons of three properties (density, viscosity, and surface tension) of three HTFs at their reference temperature are as follows:

Density: BDP ( $974 \text{ kg/m}^3$ ) > MTO ( $940 \text{ kg/m}^3$ ) > WMO ( $834 \text{ kg/m}^3$ )

Viscosity: BDP ( $0.00592 \text{ pa}\cdot\text{s}$ ) > WMO ( $0.00245 \text{ pa}\cdot\text{s}$ ) > MTO ( $0.00237 \text{ pa}\cdot\text{s}$ )

Surface Tension: BDP ( $0.0347 \text{ N/m}$ ) > MTO ( $0.0302 \text{ N/m}$ ) > WMO ( $0.0242 \text{ N/m}$ )

The simple comparison of properties, however, does not give a clear understanding on aerosol formation since comparison of a specific property of each fluid shows different rank. To resolve this, the comparison using Ohnesorge- and Reynolds-number should be considered as mentioned in Chapter II. Figure 4.1-b shows analysis of Ohnesorge- and Reynolds-number. In Fig. 4.1-b, a solid line indicates Miesse's category dividing atomization and 2<sup>nd</sup> wind induced breakup regime. Dotted lines which are simply parallel to the Miesse's category line are drawn for viewer's convenience. The combination value of Oh- and Re-number of WMO almost reaches at the atomization region resulting in early disintegration of atomization. Those of MTO and BDP indicate that their disintegration status is located at the second-wind induced breakup regime implying that their initial particle sizes are larger than that of WMO. The disintegration status between MTO and BDP, however, is located similar regime of second-wind induced breakup resulting similar particle size distribution at a given location. The measurement results and analysis of the reference condition show good agreements with analysis of Ohnesorge (1926) on atomization process.

#### 4.1.2 Pressure Effect on Atomization

The effect of injecting pressure on atomization has been analyzed. Under this analysis, fluid properties remain since temperature is fixed. The only changed parameter to atomization is the inertia force caused by changing injecting velocity. Figure 4.2 shows the result and analysis of three HTFs. Their experimental conditions are following;

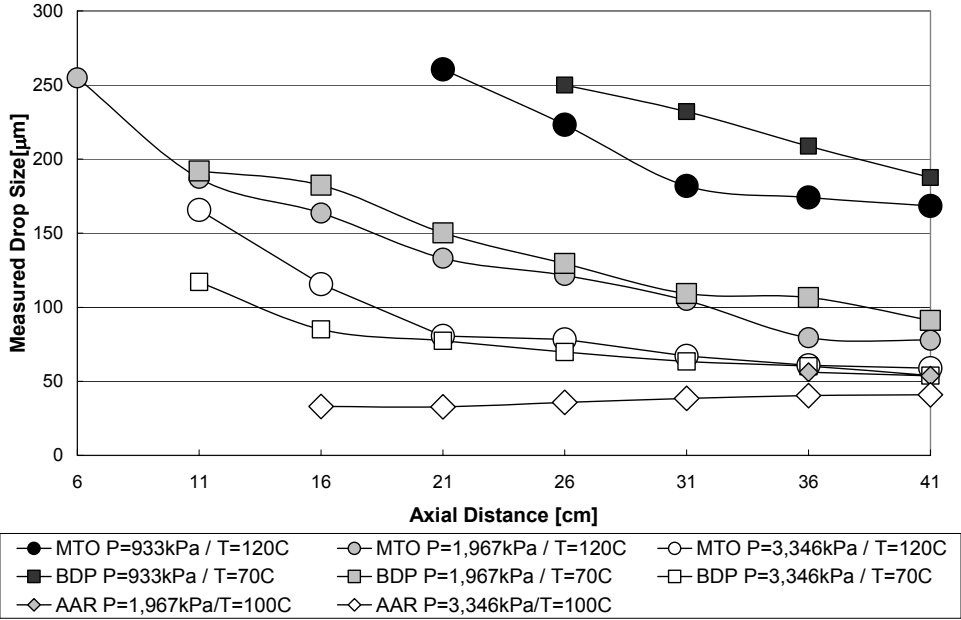
$$d_o \quad : 0.33 \text{ mm}$$

$$T \quad : 100 \text{ }^\circ\text{C for AAR / } 70 \text{ }^\circ\text{C for BDP / } 120 \text{ }^\circ\text{C for MTO}$$

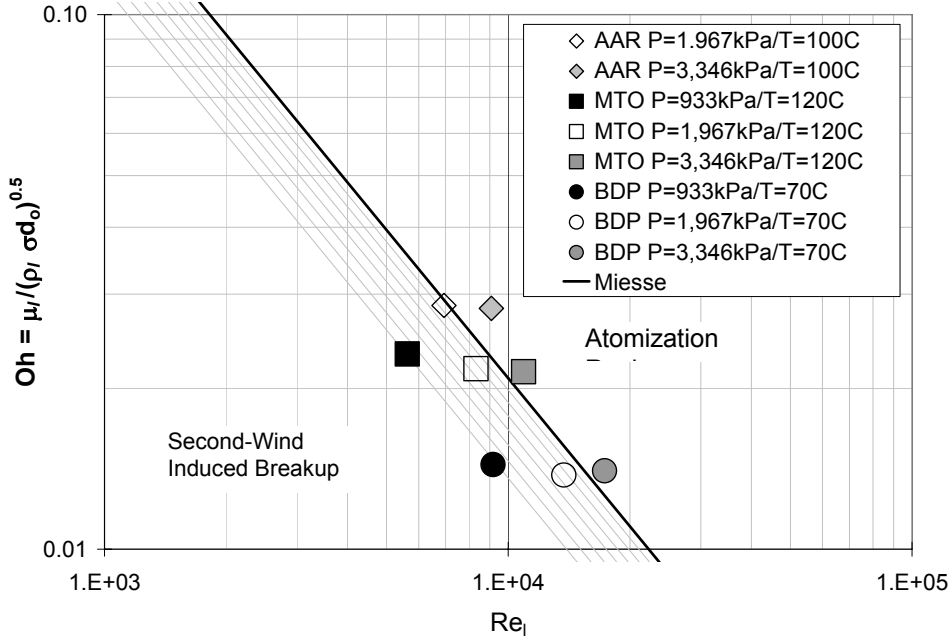
$$P \quad : 1,967 \text{ kPa, } 3,346 \text{ kPa, and } 3,346 \text{ kPa}$$

Figure 4.2-a shows measured actual droplet sizes. It is clear that the atomized particle size is inversely proportional to injecting pressure. Figure 4.2-a also indicates that the change of particle size at lower pressure region is more dependent on pressure effect than that of higher region since increasing pressure has a significant effect on reducing droplet size at lower pressure range. However, pressure change has lesser effect on changing particle size at higher pressure range.

Figure 4.2-b shows the atomization status. As injecting pressure increases, liquid disintegration status moves toward atomization regime from second-wind induced regime. For a given liquid, varying injecting pressure does not have effect on Ohnesorge number which indicates stable or unstable condition of liquid jet but does have effect on



(a) Measured droplet SMD



(b) Disintegration regime of tested fluids

Fig. 4.2. Measurement result and analysis of pressure effect.

changing Reynolds number which indicates inertia force exerted on liquid jet. From this observation, pressure effect on liquid droplet formation affects the inertia force that tends to make large particle smaller.

Since the breakup regime is similar for BDP and MTO, their particle sizes are similar at given conditions as shown in previous section. For AAR, its breakup conditions are more favorable than other two fluids, thus its droplet sizes are smaller under the same injecting pressure.

All three fluids show that their disintegration status is categorized at atomization regime at 3,346 kPa. Other injecting pressure conditions, their atomization regimes belong to the second-wind induced breakup. AAR of 1,967 kPa injecting condition, however, is located between atomization- and the second-wind induced breakup-regime resulting in the smallest size among them at a given injecting pressure. BDP and MTO show that their atomization statuses are similar at given experimental conditions.

#### **4.1.3 Temperature Effect on Atomization**

Two fluids have been analyzed in order to investigate the effect of temperature on liquid droplet formation. The measurement conditions are;

$$d_0 : 0.33 \text{ mm}$$

$$P : 1,967 \text{ kPa}$$

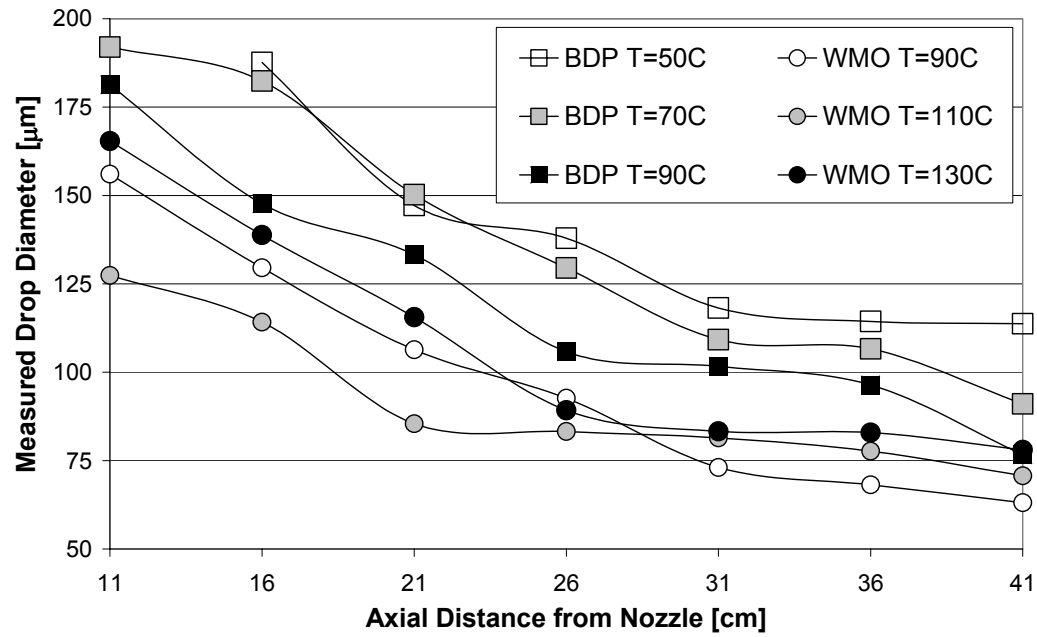
$$T : 50 \text{ }^\circ\text{C} / 70 \text{ }^\circ\text{C} / 90 \text{ }^\circ\text{C} \text{ for BDP}$$

$$90 \text{ }^\circ\text{C} / 110 \text{ }^\circ\text{C} / 130 \text{ }^\circ\text{C} \text{ for WMO}$$

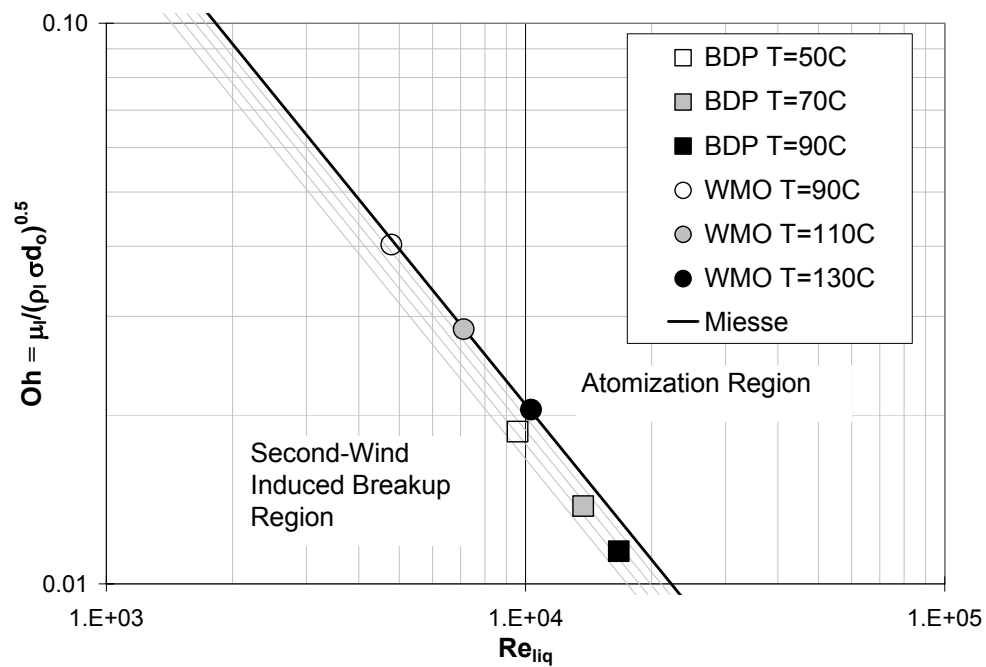


The analysis is shown in Fig. 4.3. According to experimental results shown in Fig. 4.3-a, it is very difficult to define what effect was found on a single fluid since its particle size distributions does not show consistent trend with temperatures. At some areas, higher temperature makes smaller particles, but at some places doesn't. This can be explained by Fig. 4.3-b. In Fig. 4.3-b, the disintegration regimes of BDP and WMO for three different temperature conditions are located at the same conditions resulting in complicated particle distribution of liquid. Unlikely injecting pressure, temperature has effect on both Ohnesorge number and Reynolds number. These phenomena can be explained by studying physical meaning of two non-dimensional parameters. Under a given condition of nozzle orifice diameter and injecting pressure, two non-dimensional parameters are only function of liquid properties (density, surface tension, and viscosity) which are governed by temperature. According to applied fluid properties shown in Table 3.3 and Figs. 3.1 - 3.2, the fluid viscosity in this research range is more dependent on temperature than other two properties. Thus, increasing temperature decreases the value of fluid viscosity resulting in decreasing Oh number and increasing Re number. Thus, it is not simple to say the effect of temperature on atomization process unless Ohnesorge- and Reynolds-number are considered.

Although temperature effect on a single fluid is not simple, its effect on different fluids is clear. Figure 4.3-b shows the particle distributions of WMO at three different temperature conditions are always smaller than those of BDP since three disintegration statuses of BDP are more favorable conditions than those of BDP.



(a) Measured droplet SMD



(b) Disintegration regime of tested fluids

Fig. 4.3. Measurement result and analysis of temperature effect.

## 4.2 Correlation on Predicted Particle Diameter

In Chapter II, correlation for research has been set up based on non-dimensional analysis (Buckingham, 1915) as

$$\frac{d}{d_o} = Cont. (We_g)^{e_1} (Re_l)^{e_2} \left(\frac{\mu_l}{\mu_g}\right)^{e_3} \left(\frac{\rho_l}{\rho_g}\right)^{e_4} \left(\frac{x}{d_o}\right)^{e_5} \quad (2.5)$$

One constant and five exponents can be obtained under known values by the statistical method of the regression. The regression analysis is performed by the linear least squares method to fit a line through a set of empirical data. More details are explained in Appendix C. Table 4.1 shows the result of regression. In Table 4.1,  $R^2$  is the coefficient of determination indicating estimates of the 'goodness of fit' of the line. They represent the % variation of the data explained by the fitted line. The higher value of  $R^2$ , the better the fit. The mathematical expression of  $R^2$  is followed;

$$R^2 = 1 - \frac{\text{Sum of Squares Error (SSE)}}{\text{Sum of Squares Total (SST)}} \quad (4.1)$$

$$SSE = \sum (Y_i - \hat{Y}_i)^2 \quad \text{and} \quad SST = \sum (Y_i^2) - \frac{(\sum Y_i)^2}{n}$$

where  $Y_i$  is the actual value and  $\hat{Y}_i$  is the predicted value by correlation at a given condition  $i$ . In Eq. (4.1),  $SSE$  describes the variation of observed  $Y$  from estimated  $\hat{Y}_i$ . It is derived from the cumulative addition of the square of each residual, where a residual is the distance of a data point above or below the fitted line.  $SST$  describes the variation within the values of  $Y$ , and is the sum of the squared difference between each value of  $Y$  and the mean of  $Y$ . In Table 4.1, the lowest value of  $R^2$  is 0.78 for BDP and the highest

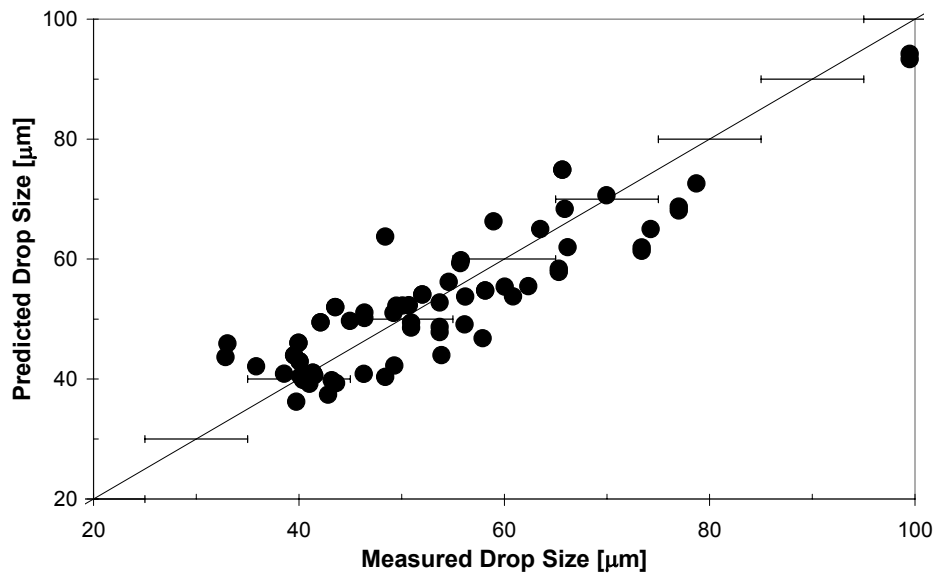
Table 4.1

Result of correlation for predicting droplet size using Eq. (2.5)

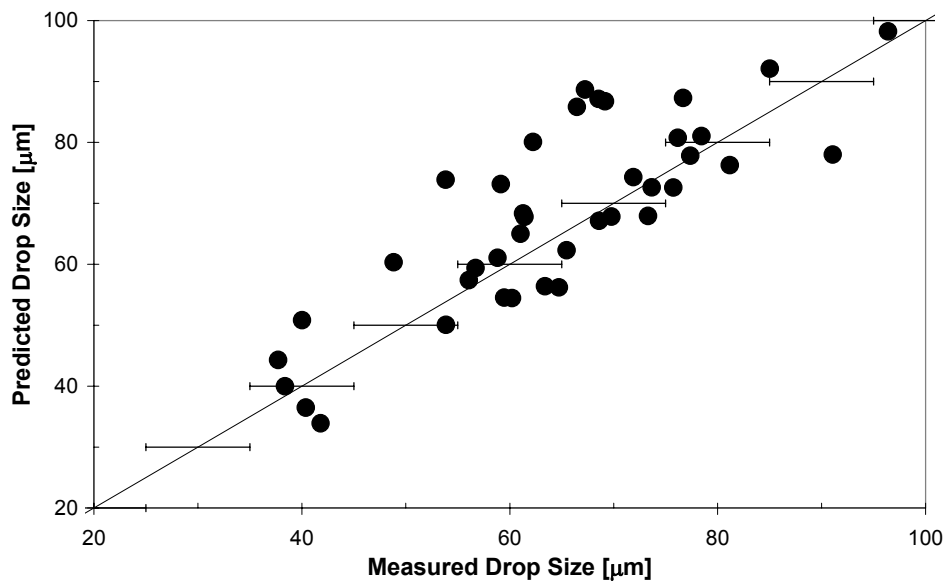
Liquid	AAR	BDP	DAL	DTA	MTO	WMO
Constant	3.9E+34	1.4E+49	1E+43	0.1723	46073.1	8.8E+31
$e1 (We_{air})$	-0.3239	-1.1216	-1.5272	-1.9157	-1.2249	-1.1148
$e2 (Re_{liq})$	-0.5271	0.3994	1.1555	1.8879	0.4926	0.4373
$e3 (\mu_{liq}/\mu_{air})$	-0.2026	0.8711	1.6372	1.8939	0.6624	0.5006
$e4 (\rho_{liq}/\rho_{air})$	-11.2582	-16.8878	-16.3309	-2.5911	-1.7504	-11.4290
$e5 (x/d)$	-0.1746	-0.5787	-0.5947	-0.2462	-0.5262	-0.2931
$R^2$	0.91	0.78	0.95	0.92	0.79	0.90

value of  $R^2$  is 0.95 for DAL. Although the lowest value of  $R^2$  may look lower, it is relatively good number for analysis since atomization process is random process which is very difficult to predict.

The results of correlations have been compared with experimental data on measured particle size under a given atomization conditions. Figure 4.4 shows the comparisons. In Fig. 4.4, ordinate indicates predicated particle size by correlation result and abscissa indicates experimentally measured particle size under given atomization conditions. Six different HTFs are shown in separate chart. Results show relatively good predictions comparing experimental data.

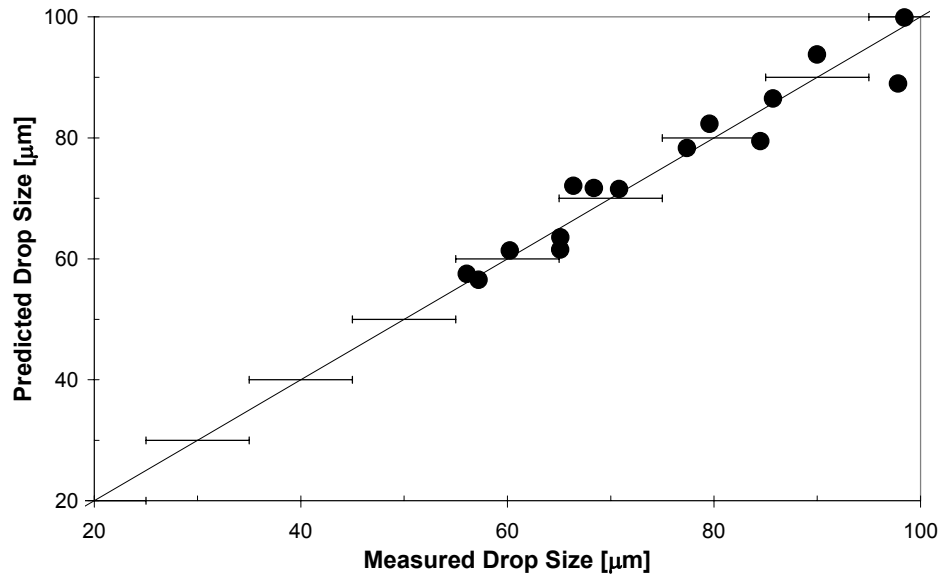


(a) AAR;  $\frac{d}{d_o} = 3.9E + 34(We_g)^{-0.3239} (Re_l)^{-0.5271} \left(\frac{\mu_l}{\mu_g}\right)^{-0.2026} \left(\frac{\rho_l}{\rho_g}\right)^{-11.2582} \left(\frac{x}{d_o}\right)^{-0.1746}$ ,  $R^2 = 0.91$

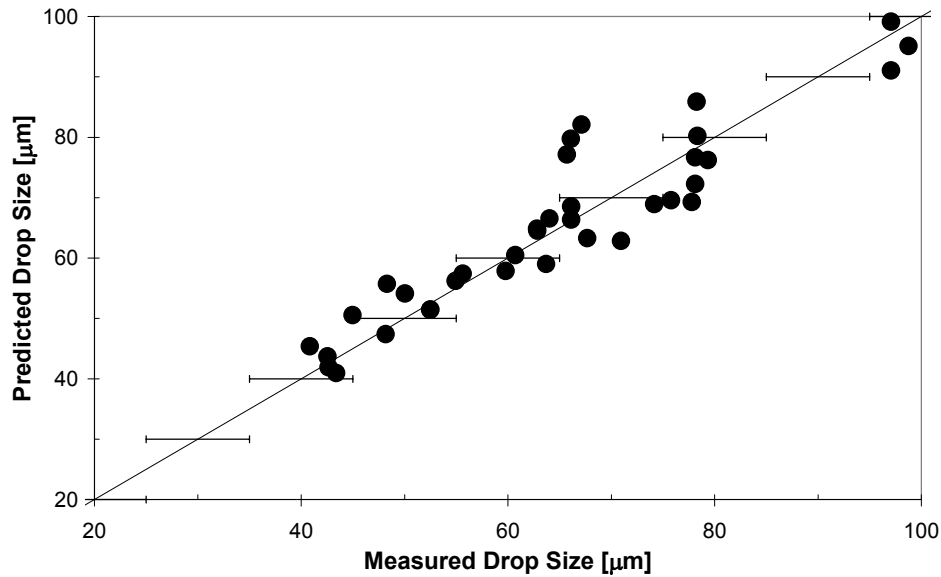


(b) BDP;  $\frac{d}{d_o} = 1.4E + 49(We_g)^{-1.1216} (Re_l)^{0.3994} \left(\frac{\mu_l}{\mu_g}\right)^{0.8711} \left(\frac{\rho_l}{\rho_g}\right)^{-16.8878} \left(\frac{x}{d_o}\right)^{-0.5787}$ ,  $R^2 = 0.78$

Fig. 4.4. Correlation results for six Heat Transfer Fluids compared with measured drop size at a given droplet formation condition.

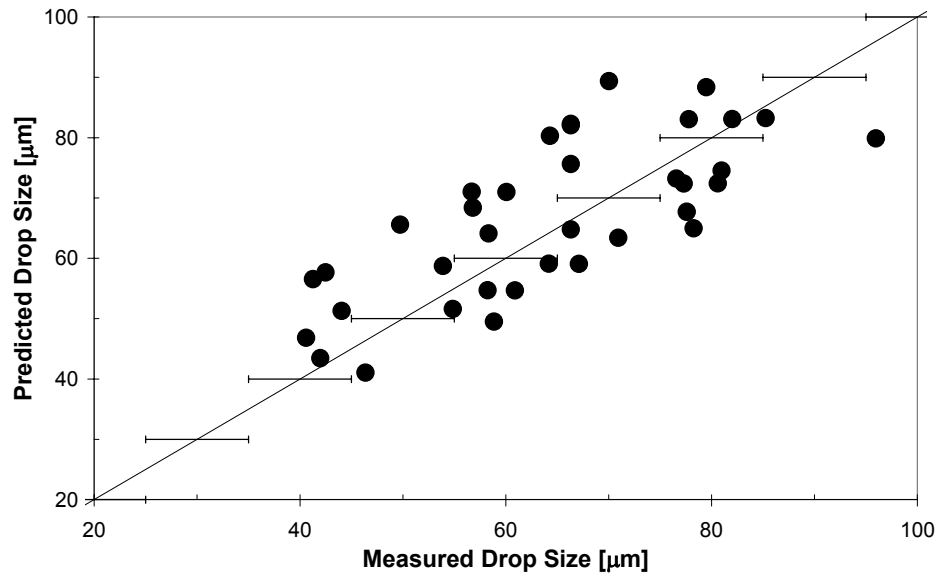


(c) DAL;  $\frac{d}{d_o} = 1E + 43(We_g)^{-1.5272} (Re_l)^{1.1555} \left(\frac{\mu_l}{\mu_g}\right)^{1.6372} \left(\frac{\rho_l}{\rho_g}\right)^{-16.33092} \left(\frac{x}{d_o}\right)^{-0.5947}$ ,  $R^2 = 0.95$

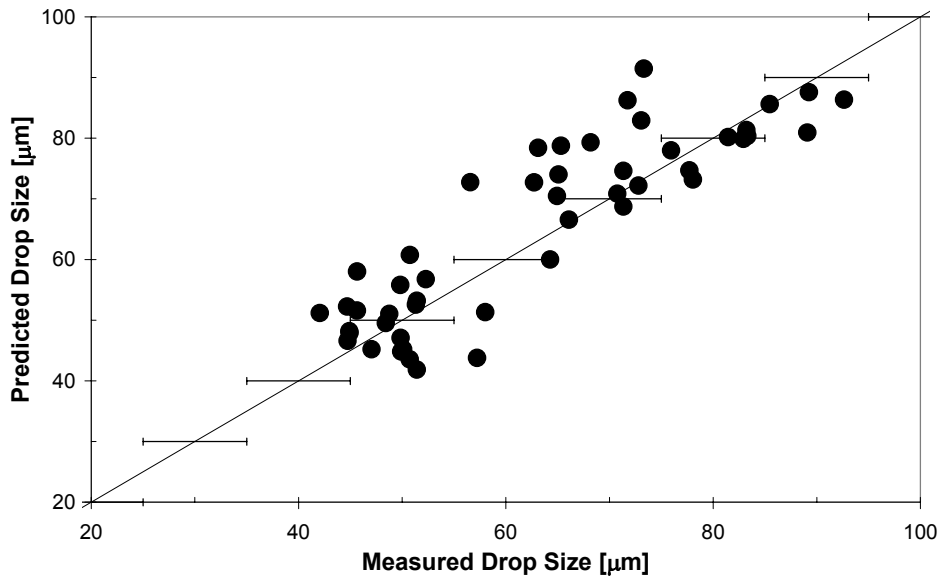


(d) DTA;  $\frac{d}{d_o} = 0.1723(We_g)^{-1.9157} (Re_l)^{1.8879} \left(\frac{\mu_l}{\mu_g}\right)^{11.8939} \left(\frac{\rho_l}{\rho_g}\right)^{-2.5911} \left(\frac{x}{d_o}\right)^{-0.2462}$ ,  $R^2 = 0.92$

Fig. 4.4. (Continued).



(e) MTO;  $\frac{d}{d_o} = 46073 (We_g)^{-1.2249} (Re_l)^{0.4926} \left(\frac{\mu_l}{\mu_g}\right)^{0.6624} \left(\frac{\rho_l}{\rho_g}\right)^{-7.7504} \left(\frac{x}{d_o}\right)^{-0.5269}$ ,  $R^2 = 0.79$



(f) WMO;  $\frac{d}{d_o} = 8.8E + 31 (We_g)^{-1.1148} (Re_l)^{0.4374} \left(\frac{\mu_l}{\mu_g}\right)^{0.5006} \left(\frac{\rho_l}{\rho_g}\right)^{-11.4290} \left(\frac{x}{d_o}\right)^{-2931}$ ,  $R^2 = 0.90$

Fig. 4.4. (Continued).

### 4.3 Validation of Correlation Results

In order to make sure of accuracy on correlations, two validation processes are conducted on empirical data obtained from Malvern system and correlation results.

The validation on empirical data is named as an instantaneous validation. During this process, the main objective is to determine whether the conditions of measurement are correct to be accepted as representative experimental data at a given experimental condition. This can be done by data analysis offered by Malvern system. When the final result of particle size distribution is obtained, the accuracy of measurement is shown by the least squares fitting parameter, '*Log Diff*', shown in the result page of Malvern output. '*Log Diff*' indicates the goodness between measured particle distribution by photo diode array and calculated-particle distribution by a given mathematical model, the Rosin-Rammler model for this research. Table 4.2 shows the indication of this parameter. Whenever each measurement is completed, validation process is conducted. The measurement result is accepted as an empirical data when the value of '*Log Diff*' is between 4 and 5.5.

Table 4.2

Description of indication of '*Log diff*' for reliability on experimental data

Log Diff (LD)	Description
$6 < LD$	Model not appropriate or experiment incorrectly performed
$5.5 < LD < 6$	Poor fit. (May be adequate for trend analysis only)
$5 < LD < 5.5$	Adequate fit but look for evidence of systematic mis-fitting
$4 < LD < 5$	Good fit. Well presented sample
$LD < 4$	Very unlikely with measured data by normal with analytic data



The second validation process is conducted after achieving correlation result. Two kinds of method will be applied to validate the established correlation results. The one is to compare the measured- and predicted- aerosol drop size under the identical conditions which are shown in previous section. The other way is to check the physical role of properties in atomization process by rearranging Eq. (2.5) as fluid properties and atomization condition. This will be

$$d_p \propto (\rho_l)^{p1} (\mu_l)^{p2} (\sigma_l)^{p3} (v)^{p4} (d_o)^{p5} (x)^{p6} \quad (4.2)$$

In Eq. (4.2), properties of fluid have a significant role in atomization process and their roles have been identified as mentioned in Flüsener (1933), Hinze (1955), Ohnesorge (1936) in Chapter II. Followings are summaries:

1. Atomized particle size is proportional to liquid surface tension and viscosity and nozzle diameter.
2. Atomized particle size is inversely proportional to liquid density, liquid exit velocity, and axial distance.

From above knowledge, the result of correlation is correct if exponential parameters have follows:

1. Positive:  $p2, p3, p5$  (particle size is proportional)
2. Negative:  $p1, p4, p6$  (particle size is inversely proportional)

Table 4.3 shows the result of rearrangement for the purpose of validation. The result of fluid properties' role in validation has fully followed the analysis summarized above indicating that correlation results of predicting the characteristics of mist formation of

HTFs can be applied. Table 4.3 also shows dependency of parameters on generated particle size. For liquid properties, density is the most dependent parameter for size distribution. Between viscosity and surface tension, surface tension has more effect on particle size.

Table 4.3

Exponential value of correlation for Eq. (4.2) (shaded cells indicate positive value)

Heat Transfer Fluid		AAR	BDP	DAL	DTA	MTO	WMO
Liquid properties	Density ( $p1$ )	-11.785	-16.488	-15.176	-0.703	-1.258	-10.992
	Viscosity( $p2$ )	0.325	0.472	0.482	0.006	0.170	0.633
	Surface Tension( $p3$ )	0.324	1.122	1.527	1.916	1.225	1.115
Atomization conditions	Velocity ( $p4$ )	-1.175	-1.844	-1.899	-1.944	-1.957	-1.792
	Nozzle Orifice Diameter ( $p5$ )	0.324	0.857	1.223	1.218	0.794	0.616
	Axial Distance from orifice ( $p6$ )	-0.175	0.579	-0.595	-0.246	-0.526	-0.293

## CHAPTER V

### DISCUSSION AND FURTHER STUDY ON LIQUID FORMATION OF HTFS

The mist formations of six different types of HTF have been intensively investigated by means of optical measurement method, the Fraunhofer diffraction. The results show that mist can form under a given favorable conditions which will lead disastrous accident results in process industries. The obtained correlation can be used for predicting the characteristics of formed mist when leakage occurs.

The most preferable condition of explosion is the flame enhancement region postulated by Burgoyne and Cohen (1954). It is explained that the particle size of enhancement region is between 10 and 30  $\mu\text{m}$  in Chapter II. Using achieved correlation results shown in Table 4.3, the condition that forms mist having enhancement region can be predicted. Figure 5.1 shows the result of prediction for six fluids using correlations. The applied conditions for injecting pressure, liquid temperature, and orifice diameter are 500 psig, 130  $^{\circ}\text{C}$ , and 0.21 mm, respectively. Figure 5.1 shows that two fluids, DTA and DAL, can form the flame enhancement region under given conditions. Their particle sizes are below 30  $\mu\text{m}$  range.

To avoid having flame enhancement region for the safety concerns in process industries, formed particle size should be larger when it happens. The proper selection of a heat transfer fluid in process may avoid detrimental effects of flame enhancement by considering parameters in correlations shown in Table 4.3. The considerations on

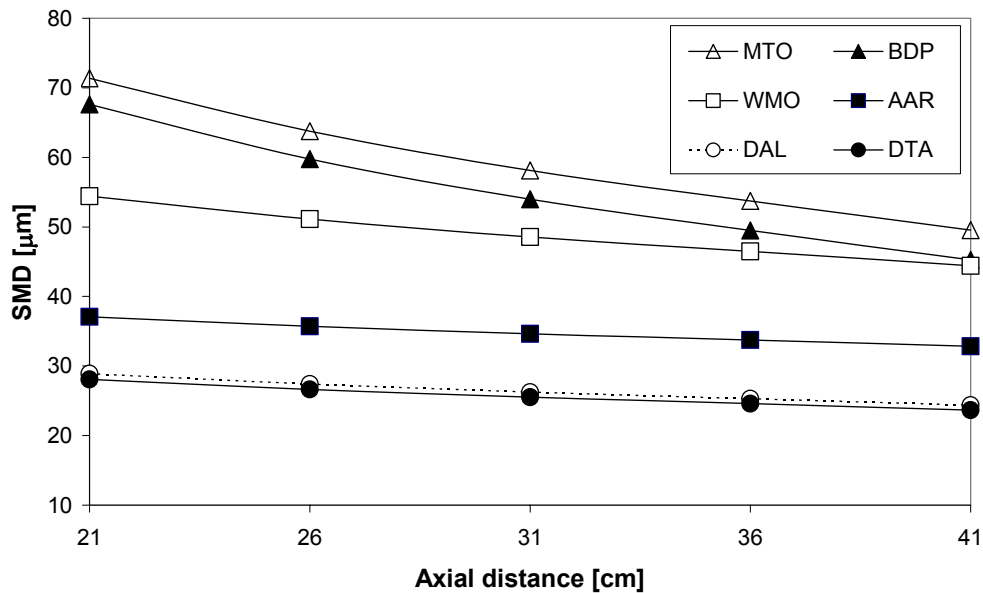


Fig. 5.1. Prediction of SMD for six different Heat Transfer Fluids under 500 psig, 130 °C, and 0.21 mm of nozzle diameter.

selecting fluid under a given working conditions (liquid volume flow rate and working temperature) is established from experimental results as follows:

### 1. Liquid Density

At given working conditions of process, the first priority to be considered is a fluid whose density is lower than others when there are more than two available fluids. The density is the most effective parameter to change diameter of formed liquid particles. The lower density is applied, the larger atomized liquid particles are generated.

The other effect of density on atomization of HTFs is a change of volume flow rate caused by friction. The Moody chart, well known chart for friction, shows that the liquid density is the one of parameters that affects friction in pipe flow. The volume flow rate of liquid in pipe is expressed as

$$\dot{V}_{liq} \propto \frac{\Delta P}{\rho_{liq}} \frac{d_{pipe}^5}{\mu_{liq} L} \text{ for turbulent flow} \quad (5.1)$$

where  $\dot{V}_{liq}$  is the volume flow rate,  $\Delta P$  is the pressure difference,  $d_{pipe}$  is the pipe diameter,  $\rho_{liq}$  is the liquid density,  $\mu_{liq}$  is the liquid viscosity, and  $L$  is the pipe length. Under a required volume flow rate and pipe system (diameter and length of pipe system), the condition of working pressure decreases as density decreases. Thus, using lower density has the best selection on generating larger liquid droplets.

## 2. Liquid Surface Tension

The second parameter is the surface tension that affects the formation of liquid particles as shown in Table 4.5. Unlike to the density, the surface tension does not change liquid flow condition as shown in Eq. (5.1). The additives are applied to investigate the formation of liquid by Christanti and Walker (2001). They observed that higher surface tension makes larger particles than lower one. To change surface tension of a given fluid, applying additive to increase surface tension would be good technique since it does not change flow conditions but change particle size.

### 3. Liquid Viscosity

The third parameter is the viscosity. Table 4.5 shows that the higher viscosity tends to make larger particles. Viscosity, however, causes opposite effect on predicting particle size as shown in Eq. (5.1). Eq. (5.1) shows that flow rate is inversely proportional to viscosity. It indicates that using higher viscosity requires higher working pressure which makes smaller particles in order to have the same liquid volume flow rate. Thus, applying higher viscosity fluid may not be good choice.

From result and analysis on the characteristics of liquid droplet formation, liquid properties have critical role in atomization. By considering their effect on particle size, a proper selection of working fluid can significantly reduce danger of mist explosion.

The ignition energy and flame propagation research on HTFs under different sets of air/fuel ratio and monodisperse particle sizes are good examples of the further study. To conduct these topics, generating known size of monodisperse liquid droplet is essential. Without monodisperse particles, the research can not be accomplished. The proper method of generating monodisperse particles would be condensation method as proposed by Cameron and Bowen (2001). It can generate monodisperse particles and can control A/F (air/fuel) ratio. Thus, the monodisperse particle of different sizes can be generated under the identical A/F. To analysis this, the high speed camera is required. Figure 5.2 shows the example of using high speed camera for the study of flame propagation. The cylindrical test chamber contains butane gas which is ignited by

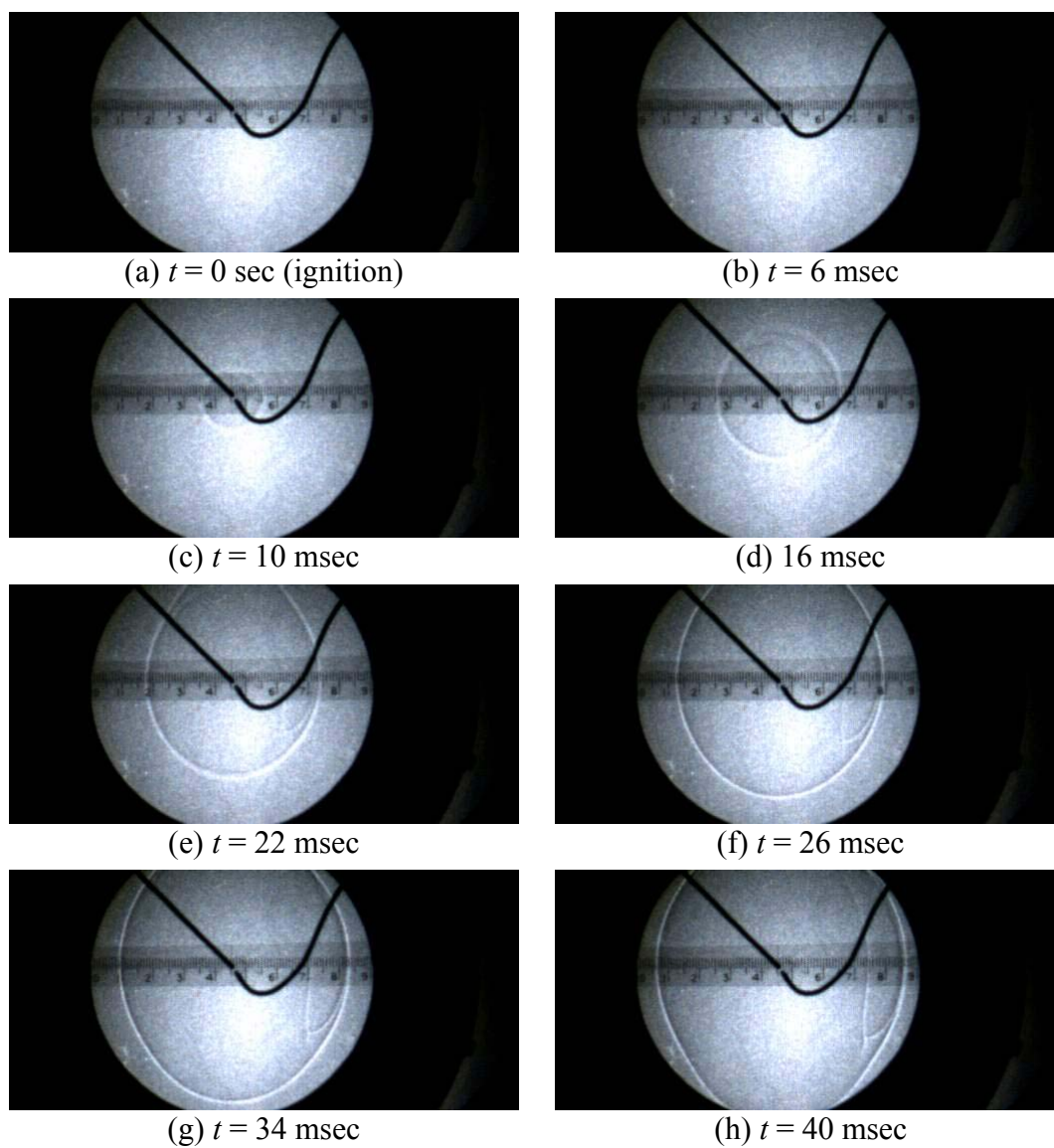


Fig. 5.2. Images of captured flame propagation using butane gas.

electrical spark. The speed of applied CCD camera is 500 frames per second. The propagation of flame front as a function of time is clearly shown in Fig. 5.2. Images are captured by the method of a visualization technique of the Schlieren optics. With proper method of generating monodisperse particles and imaging recoding system, data on ignition energy and flame propagation speed of HTFs mist can be achieved. Also, the effect of additive on changing surface tension would be another good further study on the formation of mist formed by HTFs.



## CHAPTER VI

### THE CHARACTERISTICS OF CONVECTIVE TRANSPORT OF SOLID PARTICLES IN VIRTUAL IMPACTOR: RESEARCH BACKGROUND FOR PART II

Part II will focus on the characteristics of convective transport of solid particles in VI. Chapter VI will explain the motivation on this topic and describe some backup theories to conduct research.

#### 6.1 Motivation

A solid aerosol particle has critical role in a number of applications. For example, semiconductor industries have tried to remove very fine particles from their manufacturing process. The dimension of semiconductor is much smaller than that of a dust particle and if not removed during manufacturing may lead to product failure. Environmental and health researches have focused on small particles of pollutions that deposit in our lung, resulting in serious health problems.

In the area of superconductor manufacture, a particle size is also great concerns to improve its performance. The powder-in-tube (PIT) processing is the one of methods to fabricate multi-filament superconducting wire and tape. Figure 6.1 shows the process of a multi-filament wire. Figure 6.1-a shows the first step in the process that fabricates the synthesis by a variety of chemical processes of a powder. The powder may contain a

finally desired material to form the superconductor. The second step shown in Fig. 6.1-b is to pack the powder into a metal tube typically silver and to seal to form a billet. The

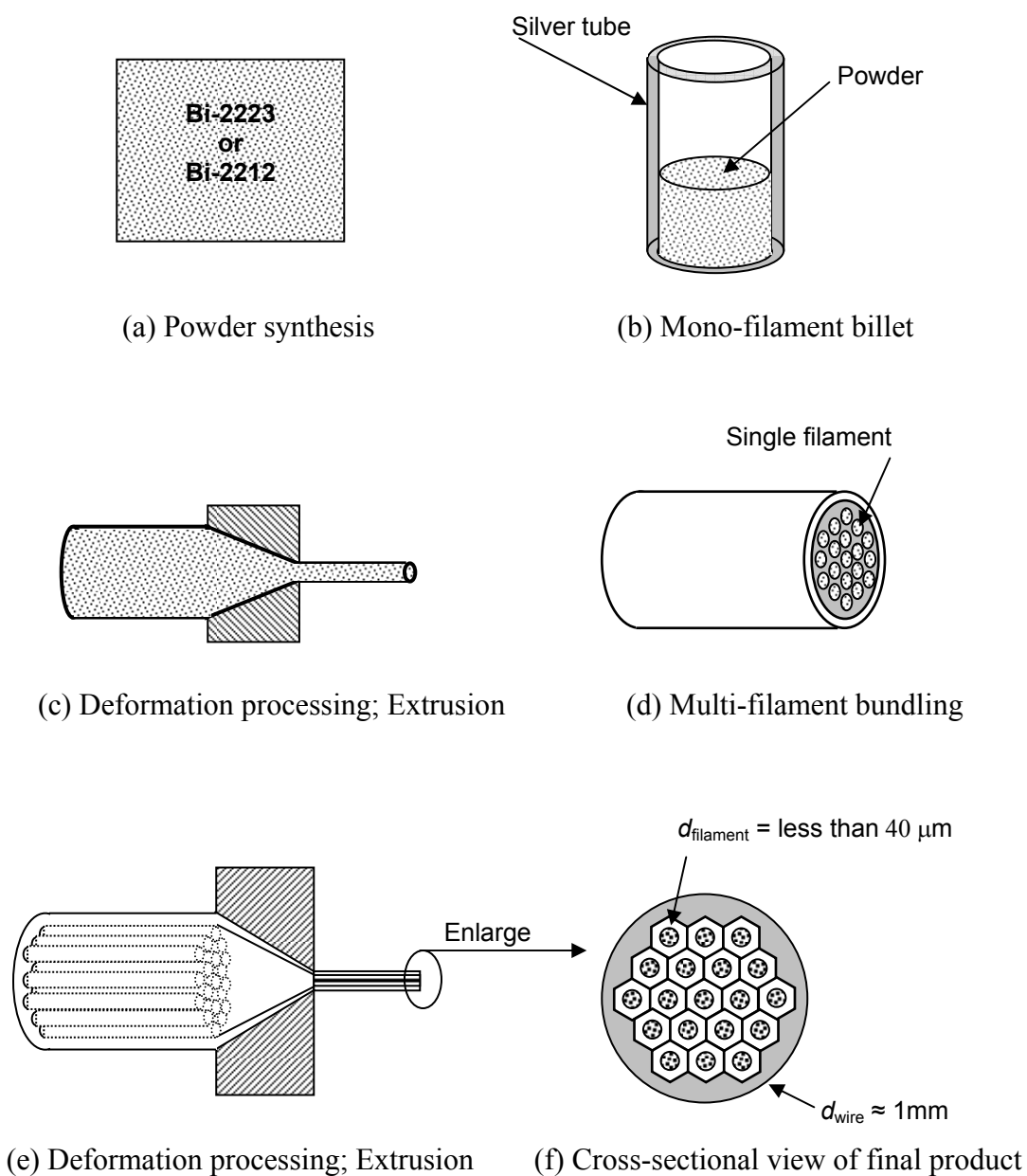
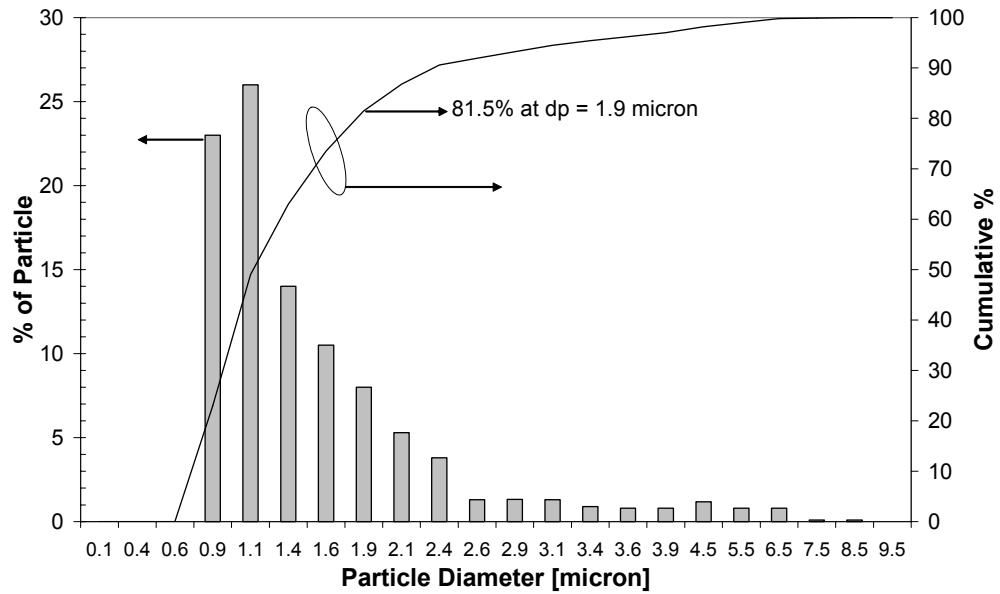


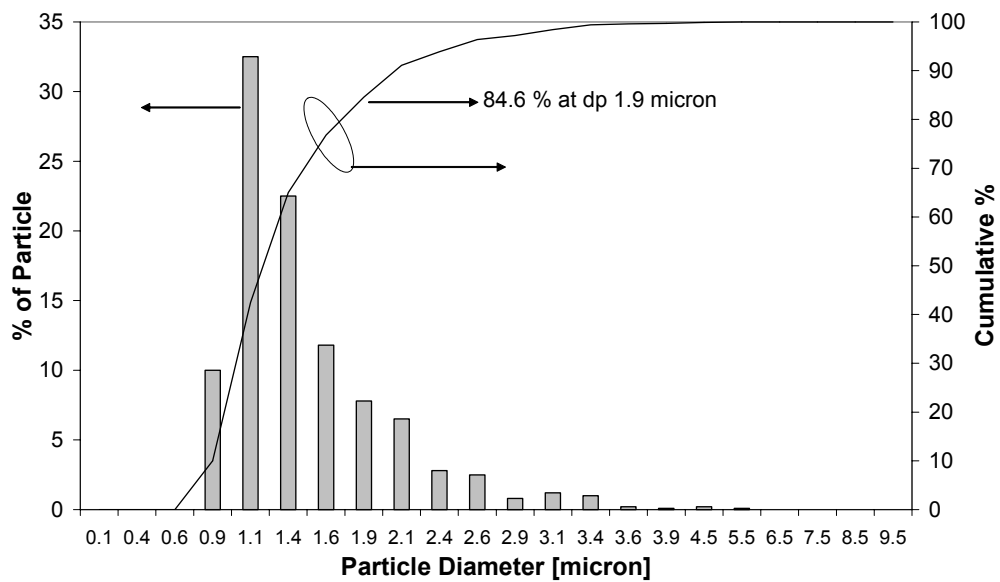
Fig. 6.1. Process of fabrication of superconductor wire.

transformation of the billet into a mono-filamentary wire is the third step shown in Fig. 6.1-c. The approach usually involves the use of dies, which are simply blocks of high strength metal with a tapered hole through which the billet is pulled (drawn) to a narrower cross-section. The fourth step shown in Fig. 6.1-d is a multi-filamentary bundling. In this stage, a number of mono-filament wires formed from individual billets are bundled together. The final step is the deformation into a multi-filamentary wire which is then forced through a series of successively smaller dies until it reaches the proper diameter. The final configuration of wire is shown in Fig. 6.1-f. The diameter of a single filament is about 40  $\mu\text{m}$  and that of wire is less than 1 mm.

During process, achieving the objective of superconductor, the ultimate current density, depends on many factors such as final phase purity, grain alignment or texture, inter-grain connectivity, cracks, porosity, and so on. Among them, the precursor particle size has a critical role since all those factors have a strong bearing on its particle size distribution. The particle size of grain has another role in lifetime of superconducting wire. The pinhole defects caused by larger particles have been observed and reduce its lifetime (Haugan et al., 1995). Therefore, to enhance performance and lifetime of superconducting tape or wire, smaller particle should be used. The particle size distribution of raw precursor, however, has relatively larger particles since it has poly-dispersed particle distribution. Figure 6.2 shows examples of the particle distributions of two precursor powders. 18.5 % and 15.4 % of raw material particles is larger than 2.0  $\mu\text{m}$  for Bi-2223 and Bi-2212, respectively. Hence, those larger particles should be removed before it forms billet.



(a) Bi 2223



(b) Bi 2212

Fig. 6.2. Two examples of particle size distribution of precursor (from Superconductive Components, Inc., Columbus, OH).

Recently, Fu et al. (2003) applied a virtual impactor (VI) to sort precursor powder for the superconductor wire production process. A VI is a device that separates different size of particles and has been developed for collecting aerosol particles. Although the general principle of a VI has been well defined in numerous papers, the characteristic of actual particles' behavior during the process of separation that has a significant effect on the efficiency of performance has not been studied. In this dissertation, one of the solid aerosol behaviors, convective transport, in the VI will be intensively studied by means of the visualization technique. The convective transport is of importance since it gives an opportunity to have better knowledge on a solid particle motion in the separation process establishing optimized VI performance condition.

## **6.2 The Effect of Particle Size on Superconductor Wire and Tape**

PIT process for superconductor wire and tape has been well recognized as one of the promising materials for conductor applications since the middle of 1980s. There are many factors to optimize its design and performance. The effect of precursor phase assemblage on 2223 phase formation and transport properties of Ag/(Bi,Pb)-2223 tapes fabricated by PIT technique was examined by Syamaprasad et al. (1998). Precursors of six different phase assemblages were applied. They showed that the choice of phase assemblage of the powder at the filling stage vis-à-vis the level of reaction it has undergone during calcinations has profound influence on the quality of the final tapes.

The effect of precursor powder size on properties of superconducting tapes and wires has been investigated by Guo et al. (1996). They found that fine particles increase

critical current density,  $J_C$ , since they accelerate the high- $T_c$  (critical temperature) phase formation rate and improve grain alignment, density and connectivity between grains. Jiang and Abell (1998) studied the effect of particle size distribution on the nature of the precursor powder and the subsequent phase formation and the critical current density of a silver sheathed Bi-2223. Three precursor powders with different particle size distributions were applied. Their results indicate that the phase formation, microstructure evolution, and critical current density are sensitive to the precursor particle size distribution. It has been shown that a small size of particle promotes the formation of the Bi-2223 phase. They showed that the critical current density tends to increase when the amount and size of non-superconducting phase decrease in the final tapes.

The pinhole defects in the silver sheath of PIT fabricated Bi-2212 tapes was observed by Haugan et al. (1995). They found that material from the oxide core exits through these pinholes that play a significant role in the mass transfer process between the core and the ambient during annealing, resulting a detrimental effect on the transport  $J_c$ . They explained that the formation of these pinholes is attributed to the PIT mechanical deformation of the precursor powders, which contain a few relatively large ( $> 30\mu\text{m}$ ) and hard (relative to silver) ratio of particles to aggregates.

From above results, it is clear that particle size has a critical effect on superconducting wire and tape. Researchers have recommended that smaller particle of precursor powder should be used for enhancing performance and life time of superconductor wire and tape.

### 6.3 Sorting Particles by Virtual Impactor

The applied basic physics of separating particles by VI is inertia difference between larger- and smaller-particles. The definition of inertia is described as the tendency of objects to resist changes in their state of motion. This inertia is dependent upon mass: the more mass, the more inertia having more tendencies to resist changes in its state of motion.

To have better understanding, the inertia impactor that was developed prior to advent of VI to collect larger particles will be introduced as an example. Figure 6.3 schematically illustrates the concept of inertia impactor. The curvilinear motion is the basic principle to be applied in the inertia impactor. When the gas is deflected by the surface, a rapid deceleration of the flow along the centerline occurs and a rapid acceleration along the impinging surface occurs shown in solid lines in Fig. 6.3. As explained above, the behavior of particles differs from their size under a given flow condition. Larger particles deviate from air stream lines and keep trying to maintain their original direction, making their new trajectories shown in the dotted line in Fig. 6.3 and deposit on the surface of impinging plate. For smaller particles, however, they follow the air stream since their inertia is dominated by air flow.

From the basic concept of inertia, an analytical criterion is needed to analyze inertia impactor. Fuchs (1964) and Hinds (1999) explain general physics of aerosol behavior regarding curvilinear motion of particle in terms of Stokes number (Stk) defined as

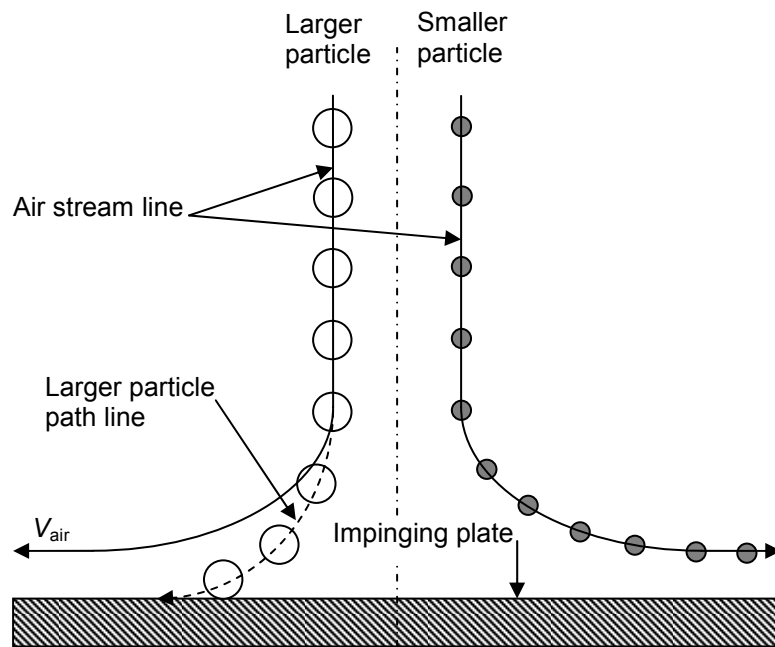


Fig. 6.3. Principle of inertial impactor (solid lines indicate stream lines that are deflected by impinging plate. Small particles can flow the streamline while larger particles move away from streamline, resulting deposit on impinging plate).



$$Stk = \frac{d_p^2 \rho_p V_{gas}}{9 \mu_g w} \quad (6.1)$$

where  $d_p$  is the particle aerodynamic diameter,  $\rho_p$  is the particle density,  $V_{gas}$  is the relative velocity of the gas and particle,  $\mu_g$  is the absolute viscosity of the gas, and  $w$  is the characteristic scale of the features on the solid. Physical meaning of Stokes number is the ratio of inertia force to viscous force. In Eq. (6.1), Stoke number is the only function of particle size under identical conditions. It indicates that larger particles have higher number indicating they have larger inertia than lower Stokes number.

The effect of Stokes number on dispersion of particles was investigated by Wen et al. (1992). They examined the dispersion of particles in a plane mixing layer between two air streams using experimental and numerical techniques. They explained particle dispersion process by the time scale ratio of the particle aerodynamic response time to a time scale associate with the large-scale organized vortex structure (original definition of Stokes number). Their results shows that particles with smaller Stokes number (less than 1) are found to concentrate near the outer edge of the vortex, but particles with larger Stokes number (larger than 1) tend to move away from the mixing layer.

The effect of inertial impactor has been numerically and experimentally examined as a function of several parameters, such as jet-to-plate distance, jet Reynolds number, and jet throat length by Marple et al. (1974) and Marple and Liu (1974). They found that the jet throat has a negligible influence, but Reynolds number has a substantial effect below a value of 500. Conner (1966) developed two-stage inertial-type impactor and examined its cutoff size as a function of varying flow rate. He found the

defects of inertial impactor that the sharpness of the particle cutoff size is varying depending on its flow conditions.

To eliminate the defects of conventional impactor (Conner, 1966), VI has been developed. The VI utilizes the additional air flow instead of using impinging wall to achieve in deflecting air flow. Figure 6.4 shows the schematic of VI. In Fig. 6.4, the majority portion of inlet air flow streamlines are deflected by one of the outlet called as major flow and the small portion will go to another outlet called as minor flow. As explained in inertia impactor, larger particles can not ride a gas streamline resulting in deviation from its inlet gas stream.

Marple and Chien (1980) numerically examined the characteristics of VI using following parameters; nozzle Reynolds number, the fraction of flow passing through the collection probe, collection probe diameter, nozzle throat length, nozzle-to-collection probe distance, and collection probe inlet design. They concluded that the most important parameter is the nozzle Reynolds number for collecting the large particles efficiently. However, they found that many of those parameters have a significant effect on collecting smaller particles. Loo and Adachi (1979) and Chen and Yeh (1987) investigated the collecting efficiency of dichromatic slit VI as a function of Stokes number. Their 50% cutoff Stokes numbers are 0.4761 and 0.6889, respectively. Ding and Koutrakis (2000) examined the size cut-off and particle loss characteristics of slit VI. They found that the effects of the flow volume and Reynolds number on the cut-off behavior and particle losses are pronounce. Recently, performance of VI focuses on separating micro- and nano-size particles. Sioutas et al. (1994) developed a sub-micro

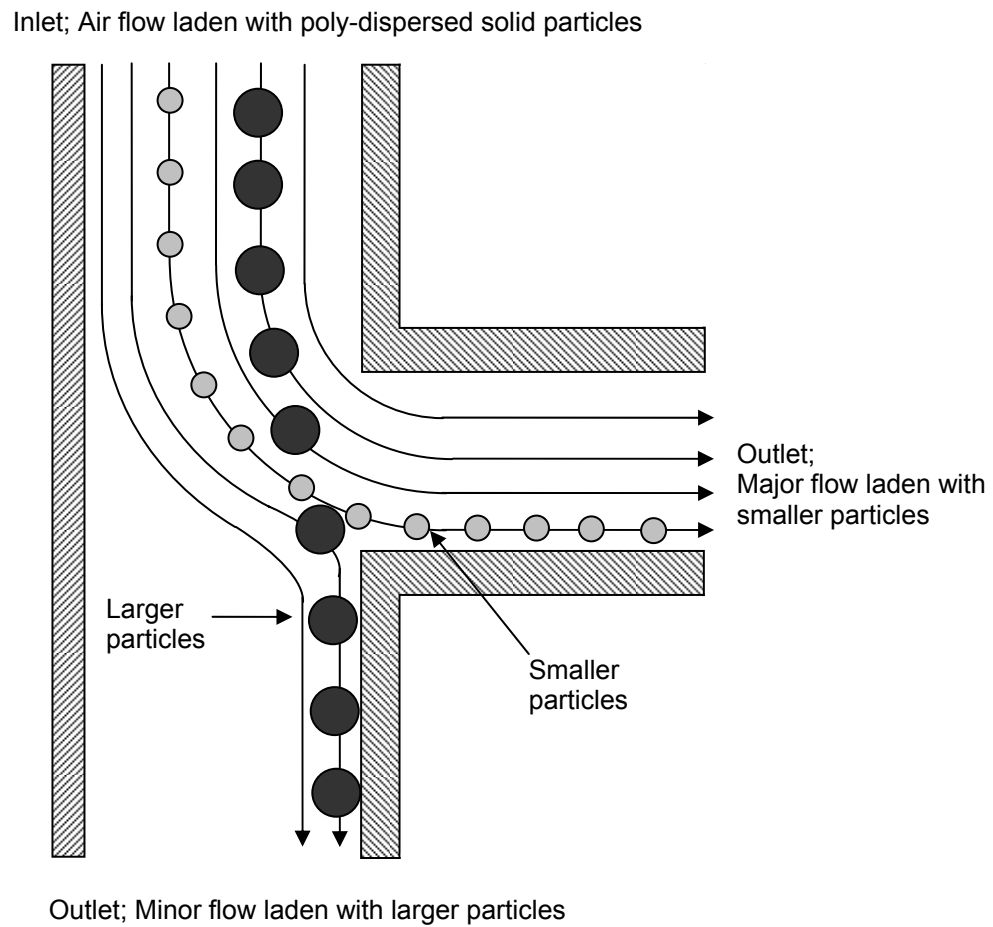


Fig. 6.4. Principle of virtual impactor on separating poly-dispersed solid particles using inertia difference between larger and smaller particles (arrows indicate the air stream lines).

cut-off size slit-nozzle VI. They demonstrated a 50% cut-point of particles in the range 0.1  $\mu\text{m}$  - 0.25  $\mu\text{m}$ . Lee et al. (2003) constructed VI that has 50% cutoff size ranging 15 nm - 60 nm.

To have better understanding on the characteristics of particle convective transport in a VI, transport behavior of separating particles needs to be visualized. There, however, are limited numbers of study on visualization on VI. Marple and Chien (1980) visualized the streamlines in a water model using an electrolytic flow visualization technique for verifying their generated numerical flow field. Han and Moss (1997) visualized the flow streams inside the VI with water flow. The generation of dye streams was applied to their study. Those two papers had been conducted to study the streamline of gas in VI. Recently, the attempt to visualize particles motion in VI has been conducted by Gotoh and Masuda (2000). They visualized solid particles of aluminum powder in rectangular jet VI. Although this research gives knowledge of transport behavior of actual solid particles in VI, it does not precisely represent actual images since the applied method of experiment was simulation of particle motion using similarity. The needs for visualization on moving solid particles in gas flow inside VI are demanded since no attempt has been made for visualizing behavior of a real solid particle in VI.

#### **6.4 Visualization on Micro Size Solid Particles in VI**

Visualization on micro size solid particles in VI has great advantage on characterizing its performance. The conventional way of study on characterization of

VI is to apply particle size analysis device, such as Coulter counter. It, however, does not offer the behavior of particle motion but gives only particle distribution at given location. The application of visualization can offer the things that can not be achieved by Coulter counter. Applying visualization not only characterizes the behavior of particle motion in system but also can count accurately number of particles with a real time.

A proverb says seeing is believing. The problem, however, is that seeing exactly and correctly is not easy work to be achieved. Visualization is the method to achieve seeing and the science that makes invisible information to be visible and valuable data. The first scientific visualization was conducted by Prandtl (1904). He studied the structure of the steady- and unsteady-water flow in a channel. The water flow was visualized by distributing a suspension of mica particles on the surface of water.

The basic rule of thumb for visualization is to achieve contrast defined as the difference in light intensity between the image (object) and the adjacent background in order to distinguish the object. The contrast can be achieved by following physical phenomena; absorption of light, brightness, reflectance, birefringence, light scattering, diffraction, florescence, or color variation. In terms of a formula, contrast can be described as;

$$\text{Percent Contrast } (C) = \frac{I(o) - I(b)}{I(b)} \times 100 \quad (6.2)$$

where  $I(o)$  is the object intensity and  $I(b)$  is the intensity of the background. In general, a minimum value of 2 percentile of  $C$  is needed by the human eye to distinguish

differences between the image and its background. In this study, two visualization techniques, light scattering and fluorescence, will be applied to achieve required contrast.

Light scattering results in the directional change of the light propagation. Mie scattering is one of scatterings and is applied to this research. Mie scattering occurs when the incident light beam scatters from a particle whose diameter is comparable to the incident beam wavelength ( $d \geq \lambda$ ). Typical example of Mie-scattering is the using headlight of a vehicle under the fog weather condition. At night without fog, the high light beam reaches longer than lower light beam and allows better range of sight. Under the fog condition, however, the range of sight using high light beam would be reduced because the scattered light by fog interrupts vision. Kihm et al. (1999) investigated the structure of water spray by high-speed gas jets using Mie-scattering technique. They visualized the water spray structures from scattered light by atomized water inside jets using green laser sheet (532 nm of wavelength) generated by a pulsed Nd:Yag laser.

The image quality of visualized objects depends on the scattered light intensity, achieving higher percentage of contrast. Although the mathematical calculation of scattering intensity requires the computation of a potentially large number of series expansions, the simplified scattered light intensities by spherical shape can be used for helping understand on physical concepts (van de Hulst, 1981).

$$I_s = I_1 \lambda_1^2 i_s(d, n, \theta) N / (4\pi^2 L^2) \quad (6.3)$$

where  $I_s$  is the scattered light intensity,  $I_1$  is the intensity of incident light,  $\lambda_1$  is the wavelength of the incident light,  $i_s$  is the scattering parameter that is a function of particle diameter ( $d$ ), refractive index ( $n$ ), and angle ( $\theta$ ),  $N$  is the particle number

concentration, and  $L$  is the distance between the positions of light scattering and observation. Under the identical experimental conditions, such as light source, observation location, and single particle, the intensity is the only function of particle size. Thus the scattered light intensity is proportional to the particle size since the intensity increases as cross sectional area increases.

The other technique applied in research is laser induced fluorescence (LIF). In the middle of 1800s, Stokes observed and studied extensively that the emitted light from a substance has a longer wavelength than the light absorbed, the so-called Stokes' shift. His paper was published in 1852. Jabłoński developed a modern theoretical understanding of Stokes observation some 70 years later. In the 1920s and 1930s Jabłoński investigated polarized light and fluorescence and was able to show that the transition moments in absorption and emission are two different things. The established principle of fluorescence is schematically illustrated in Fig. 6.5. The fluorescence consists of 4 procedures; absorption, internal conversion, emission and relaxation. During absorption process, an atom of ground status ( $S_0$ ) absorbs energy from external exciting source and becomes an excited status ( $S_2$ ) within  $10^{-15}$  sec. The amount of absorbed energy is calculated by  $h\nu_{\text{abs}}$  where  $h$  is the plank's constant ( $6.626 \times 10^{-34}$  J-s) and the  $\nu$  is the exciting source light frequency. In the next  $10^{-12}$  sec, the excited atom relaxes to the lower energy level of  $S_1$ , a process called internal conversion. Internal conversion process is caused by energy loss that is thermally transferred to environment. The status of  $S_2$  is very unstable since population of electron is inverted. Thus, the atom returns to the ground status ( $S_0$ ) where it is stable condition by emitting energy ( $h\nu_{\text{ems}}$ )

and is relaxed. Typically emission occurs after  $10^{-9}$  sec the atom is fully relaxed. The total fluorescent process takes place within about  $10^{-7}$  sec (Hecht, 1998).

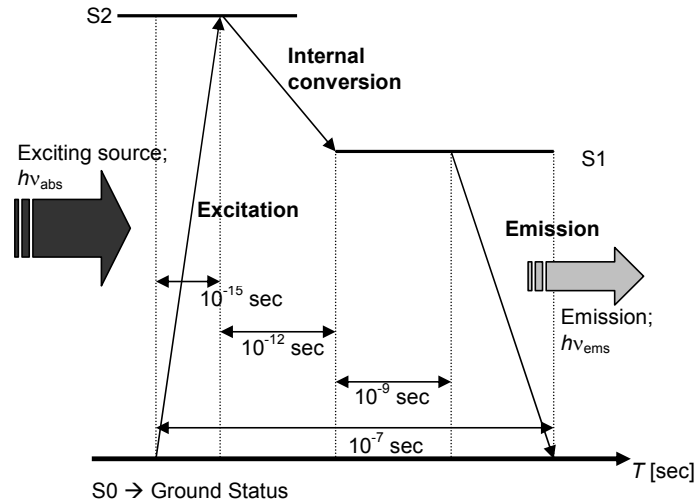


Fig. 6.5. Principle of fluorescence process.

Figure 6.6 shows the example of the characteristic spectra of fluorescent particles. The particle shown in Fig. 6.6 is excited by green light and emits red light.

The fluorescent intensity at a specific point is expressed as (Herman, 1998)

$$I_F = I_I \varepsilon [c] Q \quad (6.4)$$

where  $I_F$  is the fluorescent intensity,  $I_I$  is the incident light intensity,  $\varepsilon$  is the absorptivity,  $[c]$  is the fluorescent particle concentration, and  $Q$  is the quantum efficiency. The quantum efficiency,  $Q$ , is defined by

$$Q = \frac{\text{emitted photons}}{\text{absorbed photons}} \quad (6.5)$$



where the value of  $Q$  can not be higher than 1 as shown in Fig. 6.5.

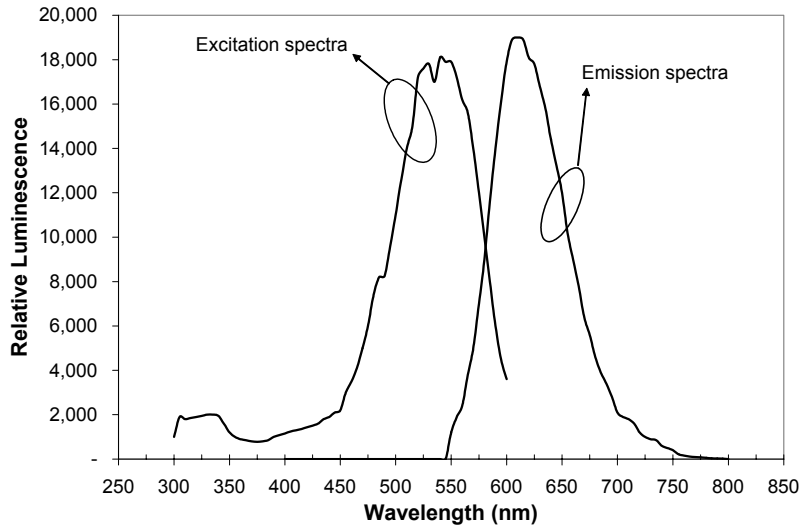
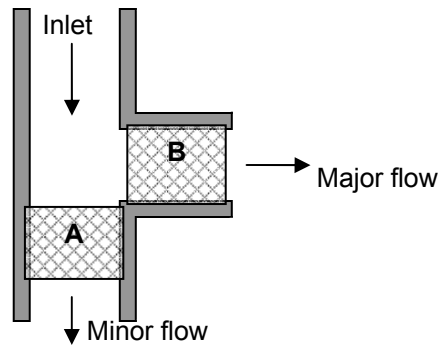
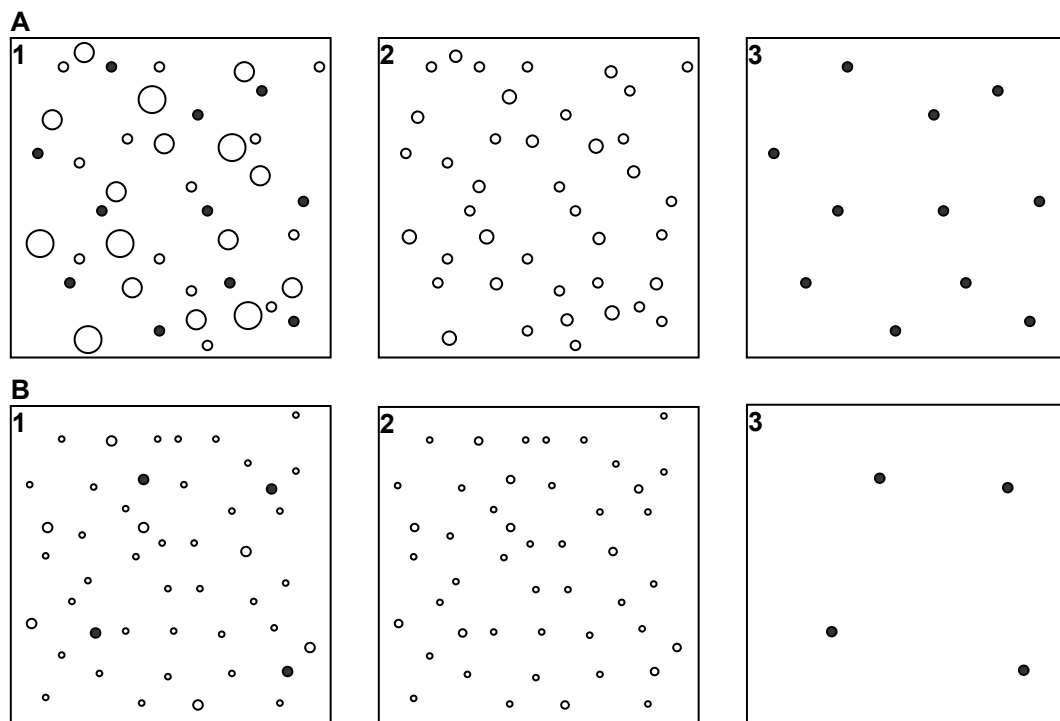


Fig. 6.6. Example of the characteristic spectra of fluorescent particles.

The application of LIF for this research gives great opportunity to discover the characteristics of particle motion as a function of particle size. Figure 6.7 explains its benefit for this research. In Fig. 6.7-a illustrates VI that separates polydisperse dust solid particles with monodisperse fluorescent particles. Larger particles (higher Stokes number) go to the minor flow and are investigated by CCD at area of A. Smaller particles (lower Stokes number) go to the major flow and are investigated at area of B. Figure 6.7-b shows the images that we can obtain from area of A and B. The first column (1) indicates the presence of all particles including dust and fluorescent particles at both areas of A and B. Blank circles indicate polydisperse dust particles and solid circles indicate monodisperse fluorescent particles. The second column (2) indicates the



(a) Particle separation in VI (A and B are investigated area)



(b) Particle images under different conditions ( 1) actual particle presence at the system, 2) recorded image by Mie-scattering, 3) recorded image using optical filter by fluorescent, different sizes of solid circle represent polydisperse dust particles and uniform size of black circles represents monodisperse fluorescent particles).

Fig. 6.7. Examples of using fluorescent particles in polydisperse dust particles for the study of the characterization on particle behavior and investigating efficiency of system.

images that are detected by CCD under Mie-scattering method. Under this condition, distinguishing particle sizes is not possible since the size of detected particles look similar unless microscope is applied. The third column (3) shows the image obtained by applying optical filter that blocks the wavelength of illumination light. In this condition, the Mie scattering signals from dust particles can be excluded since their wavelength is the identical as that of illumination. The fluorescent particles, however, emit longer wavelength shown in Fig. 6.6 than those of dust particles. Thus, only monodisperse fluorescent particles can be detected by using a proper filter. This can offer better analysis on VI since the characteristic of system can be analyzed as a function of fluorescent particle size which is known monodisperse diameter.

The applications of fluorescent particles have been used for biologist to dye cells in order to see through microscope for a long time. As an engineering application, it has been recently used for micro-scale fluidics. Park et al. (2000) investigated velocity inside heated capillary pore by LIF technique. Visualization was achieved by two different types of light; ultraviolet light (355 nm) by pulsed Nd:Yag laser and blue light (488 nm) by continuous wave (CW) Argon-ion laser. Nakayama and Tanida (1997) have listed more applications of visualization using fluorescence for engineering purpose.

### **6.5 Particle Generation of Monodisperse Size**

To characterize the convective transport behavior in VI and evaluate the performance of VI, the known size of mono-disperse particles is essential. Most of all available atomizers generate poly-disperse particles except a vibrating orifice aerosol

generator (VOAG). The criteria of VOAG regarding capability of mono-disperse particle is well investigated by Berglund and Liu (1973) and Levendis and Flagan (1987).

The principle applied to VOAG is oscillations and perturbations exerting the instability on the surface of cylindrical liquid jet column. Figure 6.8 schematically illustrates the instability on the liquid surface producing liquid droplets. In Fig. 6.8, wavelength,  $\lambda$ , is the distance between disturbances,  $d_j$  is the diameter of liquid jet, and  $d_p$  is the diameter of generated liquid particle. The formation of liquid droplets from liquid jet breakup was well explained by Rayleigh (1878) as mentioned in Chapter II. He theoretically explained the optimum wavelength where the disintegration is the most unstable condition and his result was verified experimentally by Tyler (1933). Tyler investigated the frequency of formation of drops as a function of the wavelength of the disturbance. Their results are following;

$$\begin{aligned}\lambda_{opt} &= 4.51 d_j \text{ by Rayleigh} \\ \lambda_{opt} &= 4.69 d_j \text{ by Taylor}\end{aligned}\tag{6.6}$$

It is possible that uniform size of droplet can be produced by the disturbances under a certain instability condition. Schneider and Hendricks (1964) experimentally examined the formation of monodisperse particles and determined that uniform droplets could be produced by varying  $\lambda$  within the following limits

$$3.5 d_j < \lambda < 7 d_j ,\tag{6.7}$$

VOAG utilizes a piezoelectric device to generate and control wavelength for favorable condition of generating monodisperse particles. Detail schematic on VOAG system will be shown in chapter VII.

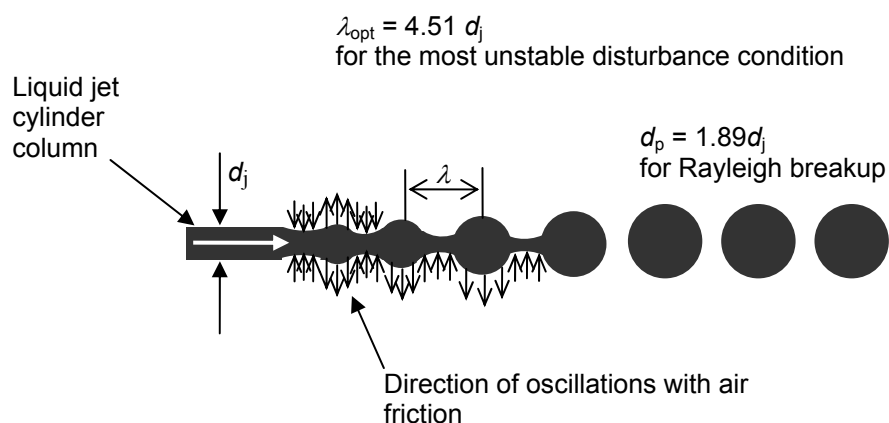


Fig. 6.8. Diagram of the instability on the liquid surface of a cylindrical jet column producing liquid droplets.

To satisfy research objectives, solid particles should be applied. Since VOAG initially generates liquid solution of uniform size particles, the method of converting solid particles from liquid particles is needed. The feasible way to achieve solid particle generation is to use solution of solid solute and volatile solvent. Figure 6.9 shows the procedure of generating solid particles from liquid solution particles. Figure 6.9-a shows the initial particle shape. In this stage, generated particles consist of volatile solvent and molecule size of solid solute. The concentration of solute is much lesser than that of solvent. During vaporization process shown in Fig. 6.9-b, volatile solvent vaporizes leaving higher concentration of solute and smaller particle size than initial stage. Either isopropanol or ethanol can be applied as a solvent for experiments. At the last stage shown in Fig. 6.9-c, volatile solvent totally evaporates and only solid molecules of solute remain. These solid molecules of solute form solid particle of

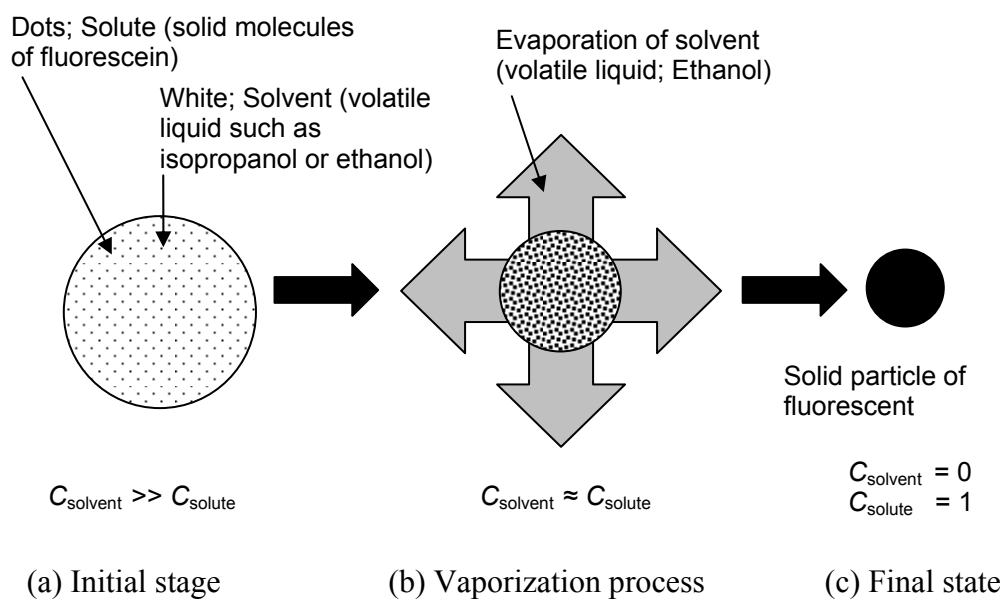


Fig. 6.9 Process of generating monodisperse solid particles from uniform size of liquid particles generated by VOAG. (a) Initial stage is the liquid solution of uniform size particles where solute concentration is much lesser than that of solvent. (b) During vaporization process, solvent vaporizes resulting higher concentration of solute and smaller particle size. (c) When solvent totally vaporizes, solid particle of solute forms.

monodisperse particles. Thus, selecting proper solvent and solute can provide monodisperse fluorescent particles that can satisfy research objectives.

## CHAPTER VII

### EXPERIMENTAL SETUP

In this chapter, experimental setup for investigating the characteristics of convective transport of solid particles in VI by using visualization techniques and experimental conditions will be introduced.

#### 7.1 General Apparatus

Figure 7.1 shows overall apparatus of experiment setup. It consists of 5 subsystems: light illumination optics, virtual impactor, image recording/processing, particle imaging, and particle generation system. For different batches of monodispersed aerosols generated by the generator, experiments have been performed to visualize their detailed trajectories in the virtual impactor using the laser sheet illumination and the cinematographic recording of multiple image frames. Details on each system will be introduced in following sections.

##### 7.1.1 Light Illumination Optics System

The main purpose of illumination system is to offer proper intensity of light inside VI for achieving higher contrast ratio to detect particles. Light source utilizing

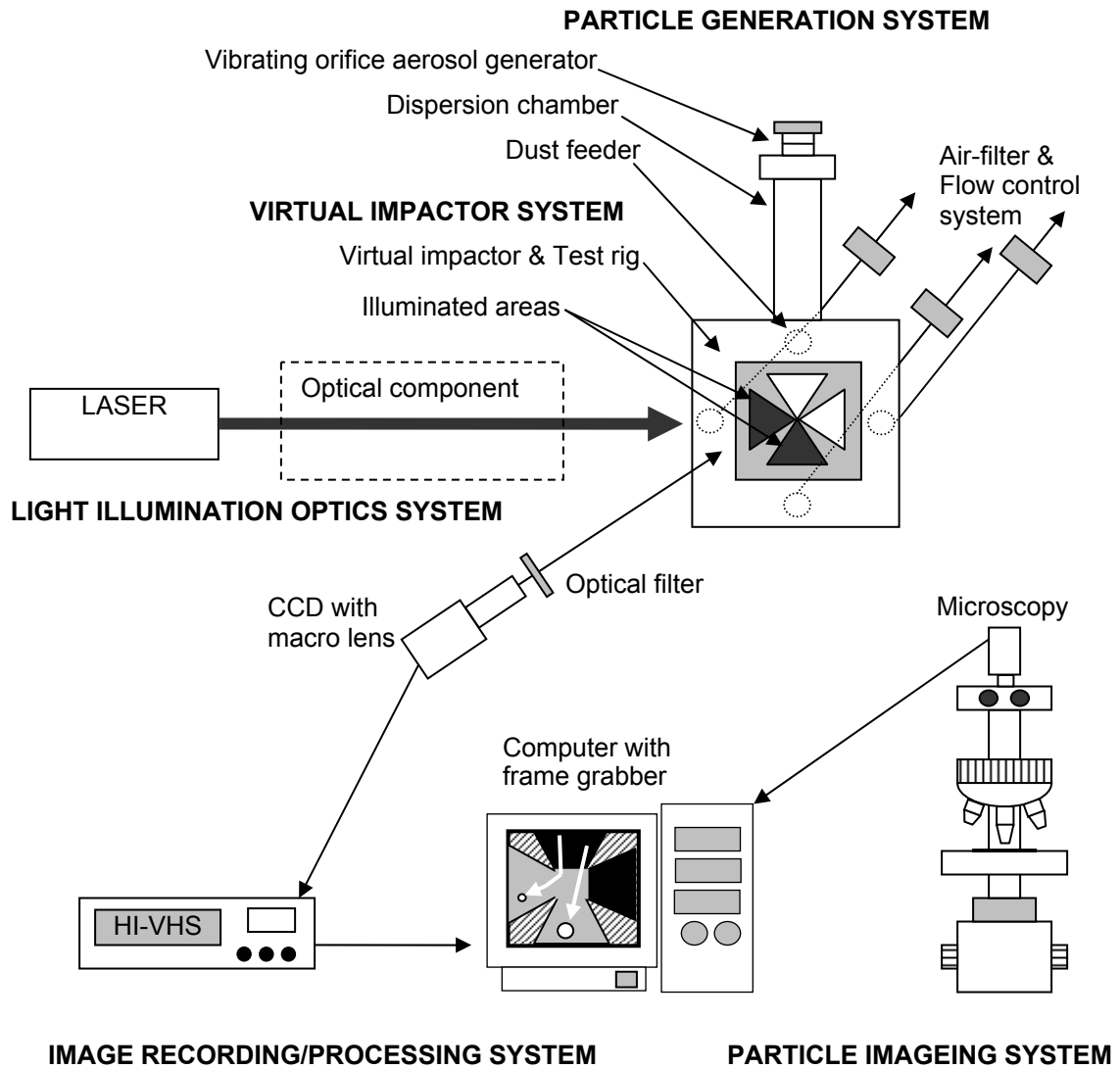


Fig. 7.1. General apparatus of experimental setup for investigating the characteristics of convective transport behavior of different sizes of solid particles in virtual impactor using visualization techniques.

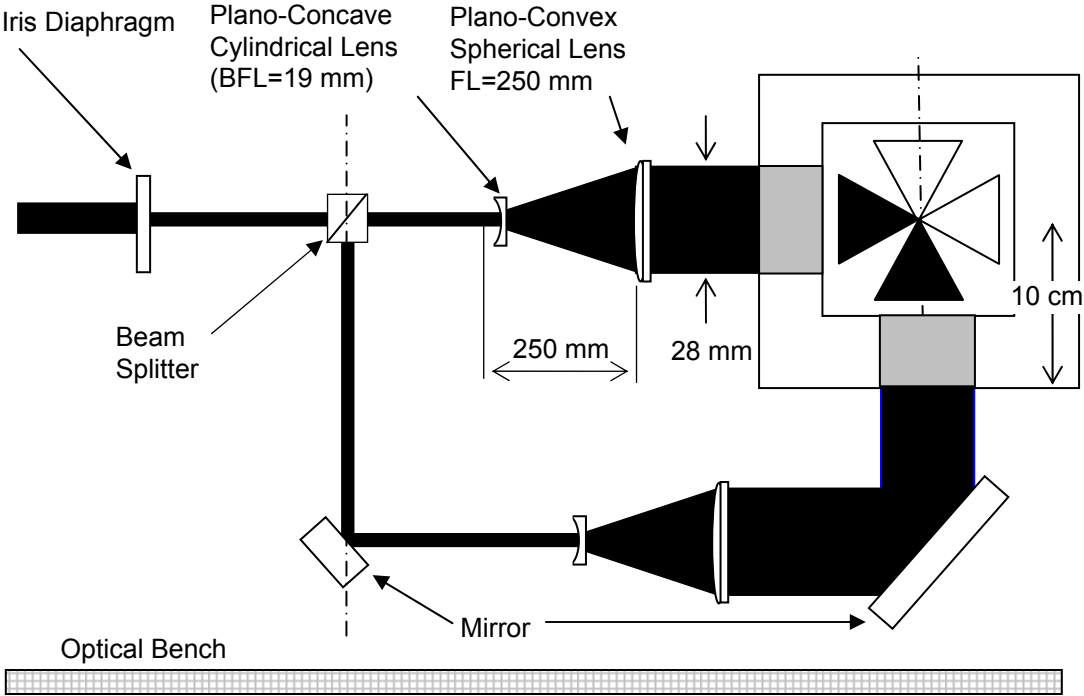


two different types of laser and optical components having several optical lenses are applied to this system.

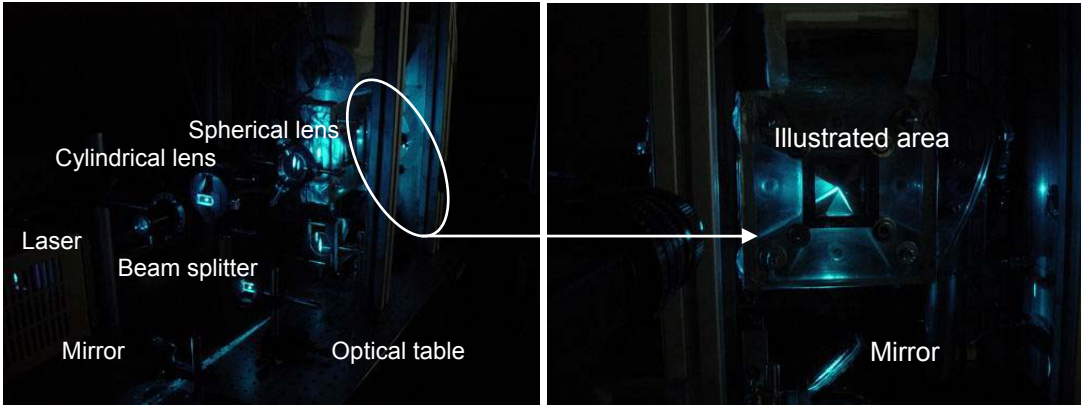
Pulsed Nd:Yag laser and Ar-ion continuous wave (CW) laser are illumination sources. Nd:Yag laser, Spectra-Physics GCR-12, is a solid state laser whose the beam diameter is 8 mm and the light intensity is  $155 \text{ mJ/cm}^2$  at 532 nm of wavelength. It can generate four different wavelengths; 1064 nm, 532 nm, 355 nm, and 266 nm. During experiments, 532 nm of wavelength (green light) has been applied. Nd:Yag laser has great advantage on freezing any fast moving particles within a single pulse since its duration of illumination is about 7 nsec. Within this time, the light travels only about 2 meters. Thus, Nd:Yag laser is applied to measure number of particles in a specific field of view to gather data, such as collecting efficiency and mass loading effect.

Argon-ion laser is applied as a CW laser. It generates wavelength between 488 nm and 515nm with beam diameter of 2 mm. Its power is 210 mW at whole spectrum and 38 mw at wavelength of 488 nm. The advantage of using CW laser is that it can tract the motion of particles for a given illumination time. This laser is applied to find a trajectory of a specific particle in order to know the characteristics of convective transport behavior.

The system of optical components has been designed according to geometric optics (Hecht, 1998) in order to generate two laser sheets from a single laser beam with proper illumination volume. Figure 7.2 shows optical components consisting of the iris diaphragm, the beam splitter, two mirrors, two cylindrical plane-concave lenses, the optical filter, and several mounting components. In Fig. 7.2-a, the beam diameter of laser



(a) Component design based on geometric optics



(b) The apparatus of implemented setup

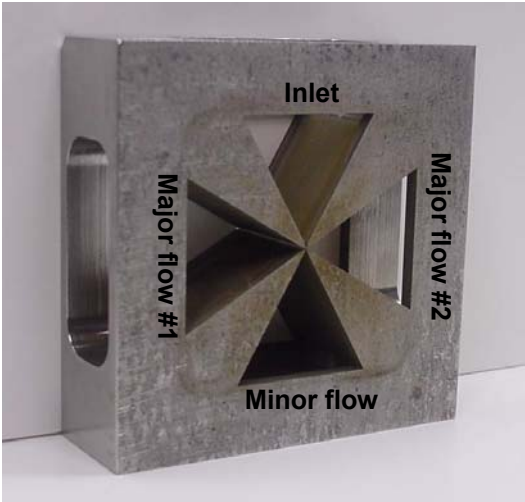
Fig. 7.2. Design of geometric optics for illuminating two test areas and images of implemented setup (BFL: Back Focal Length, FL: Focal Length).

beam coming from laser is adjusted by the iris diaphragm. The designed beam diameter is 2 mm for Nd:Yag laser and 1 mm for Ar-ion laser. Then, this beam is split by beam splitter having 50% of incoming laser beam. Two split beams pass through plano-concave cylindrical lens whose back focal length is 19 mm and is diverged in only 1-D direction (vertical direction as shown in Fig. 7.2) forming diverging laser sheet from laser beam. The plano-concave spherical lenses are applied since collimated laser sheet is needed. The focal length of the lens is 250 mm and is focused at the focal point of cylindrical lens to make collimated laser sheet. To change the light path for illuminating minor flow area, two surface coating mirrors have been applied. These whole parts are setup on the optical table for stable experimental conditions. Figure 7.2-b shows actual light path through the optical components.

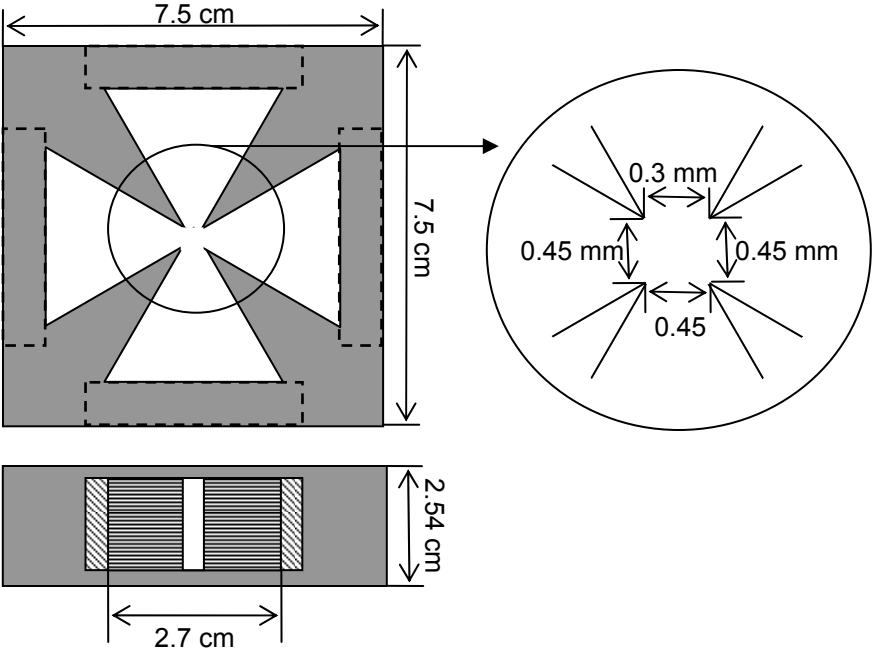
### 7.1.2 VI System

VI system includes VI, test rig, air filter, and flow system. VIs applied in this research have been designed and fabricated. Figure 7.3 shows the actual image of one of VIs and illustrates its dimensions. It is designed and fabricated to satisfy requirements shown in Table 7.1. The designed 99% of cutoff size at the Stokes number of 2 is 1.7 micron of precursor particle whose density is  $3\text{g/cm}^3$ .

To run experiments, VI should be housed in airtight test rig which allows air flow to only designated ports and offers optical windows for illuminations and observation. To satisfy these conditions, test rig shown in Fig. 7.4 has been designed and implemented. The applied material is a Plexiglas. Figure 7.4-a shows front view of



(a) Picture of VI



(b) The dimension of VI

Fig. 7.3. Virtual impactor applied to research.

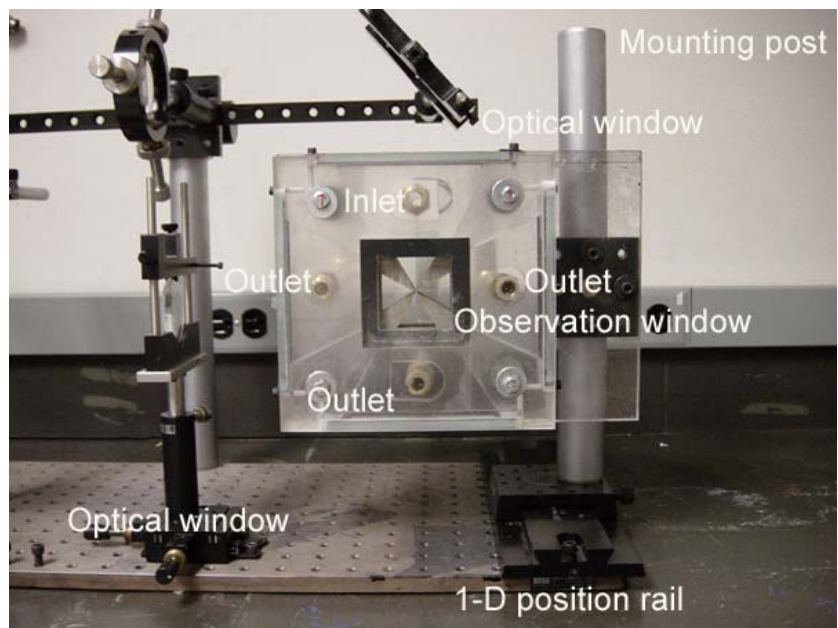
implemented test rig. The material of all windows is a glass and all windows can be removable. Test rig is placed 2-D positioning mounts (mounting post and 1-D position rail) in order to adjust its location according to the plane of illumination sheet. Figure 7.4-b shows a side view of the system. There are 4 ports on the back of the test rig for connecting inlet flow and three outlet flows. The dust particles are supplied through the inlet flow. The fluorescent particles are introduced through the upper window.

Table 7.1

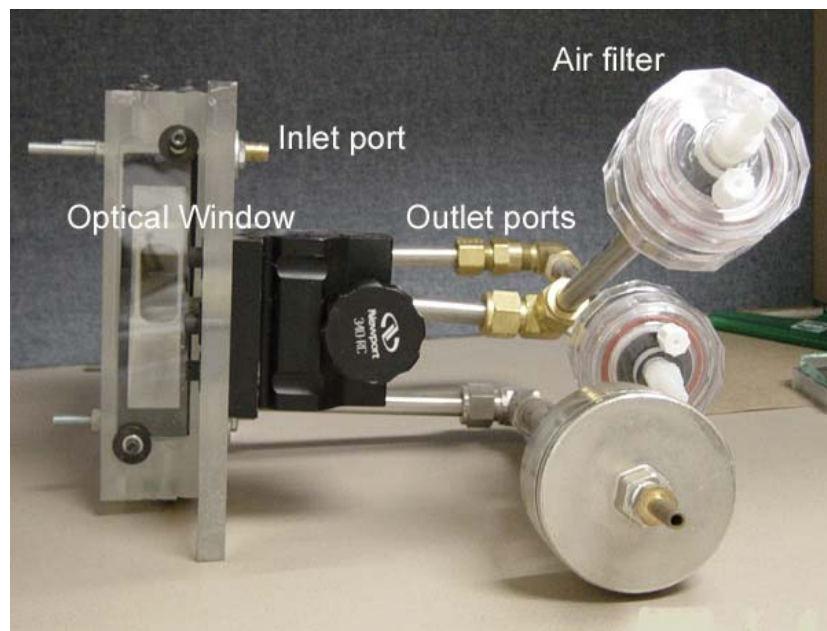
Design requirements for current virtual impactor

Description		Requirement
Applied particle density (Precursor)		3 g/cm <sup>3</sup>
Characteristic length (nozzle throat width)		0.3 mm
99 % cutoff Stokes number		2
particle size at Stk. <sub>99%</sub> cutoff		1.7 μm
Velocity at inlet nozzle throat		10.6 m/sec
Reynolds number at nozzle throat		224
Volume flow rate	Inlet	$8.07 \times 10^{-5} \text{ m}^3/\text{sec}$ (10.26 SCFH <sup>1</sup> )
	Major flow (90% of inlet flow)	$3.63 \times 10^{-5} \text{ m}^3/\text{sec}$ (4.617 SCFH) for each major flow
	Minor flow (10% of inlet flow)	$0.807 \times 10^{-5} \text{ m}^3/\text{sec}$ (1.026 SCFH)

<sup>1</sup> SCFH: Standard Cubic Feet per Hour



(a) Front view



(b) Side view

Fig. 7.4. Images of VI test rig.

To control air flow rate, one centrifugal pump, 5 air flow meters are applied. Fig. 7.5 illustrates the schematic of the applied air flow system. Inlet port is connected to particle seeding system to supply solid particles. 3 outlet ports are connected to the pump shown in Fig. 7.5. The amount of inlet air flow rate is controlled by air flow meters depending on experimental conditions. Under any inlet conditions, 45% of inlet flow goes to each major flow and 10% of inlet flow goes to minor flow. For two major flows, two different types of flow meter, larger and lower flow rate controller are applied to control flow rate accurately depending upon flow rate. The air filters are located between air flow meters and test rig to avoid particles to enter the flow meter.

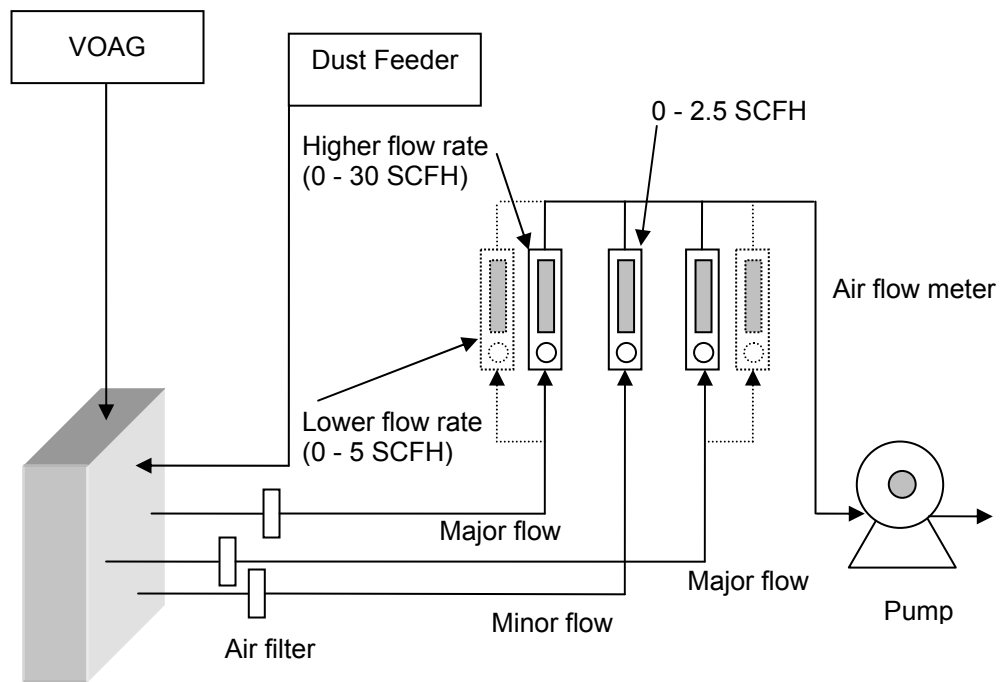


Fig. 7.5. Configuration of air flow control system.

### 7.1.3 Image Recording/Processing System

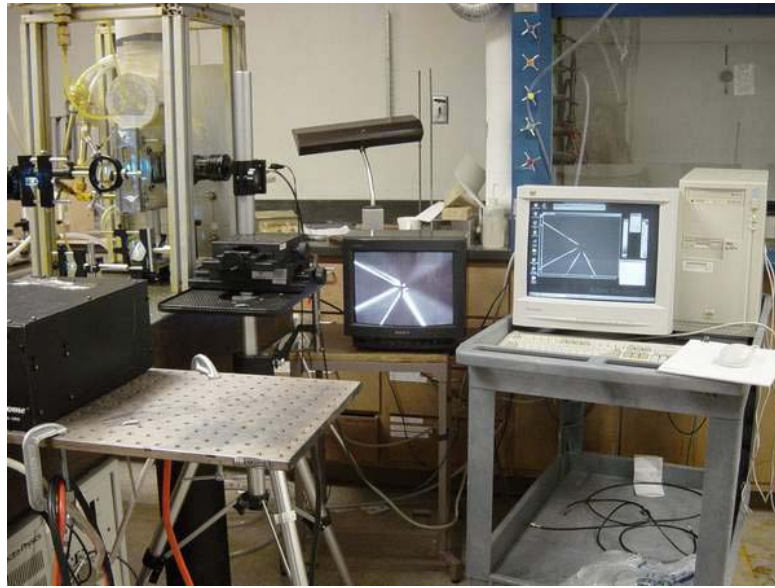
A CCD camera shown in Fig. 7.6 detects two types of images: (1) the scattered light images to record the frequency of the seeded particles in the measurement volume, and (2) their fluorescence emission to track the particle trajectories. The used CCD has a spatial resolution of  $640 \times 480$  pixels and a macro lens. The field of view of macro lens is  $1.6 \text{ cm} \pm 8 \text{ mm}$  for horizontal direction depending on its focal length. Applied optical filter is notch filter which blocks only 532 nm of wavelength.

Both images were recorded on a VHS tape recorder and transferred to a PC station using a frame grabber. Analog images from the VHS tape were later digitized for further analysis using a Sony digital video converter and the images were analyzed using Adobe Premiere<sup>tm</sup> 6, a movie editing software. Although using a PC with frame grabber can directly provide digital images (8-bit or 12-bit), VHS tapes were used to provide higher resolution images of 24-bit and also to store larger number of frames without being limited by the hard disk capacity. The digitized images obtained after conversion from the VHS tape are analyzed frame-by-frame to determine the particle counts or trajectories of individual particles.

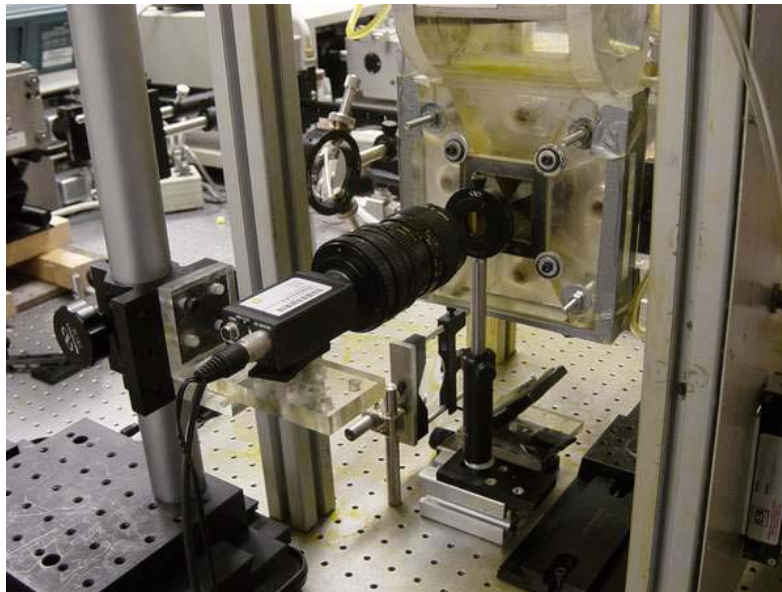
### 7.1.4 Particle Imaging System

The status of monodisperse and particle size should be verified to ensure the accuracy of experiment result. Particle imaging system offers above requirements. The reflected fluorescent microscope, Olympus BX61, is applied as a particle imaging system shown in Fig. 7.7. Figure 7.7-a shows its actual image. This microscope is



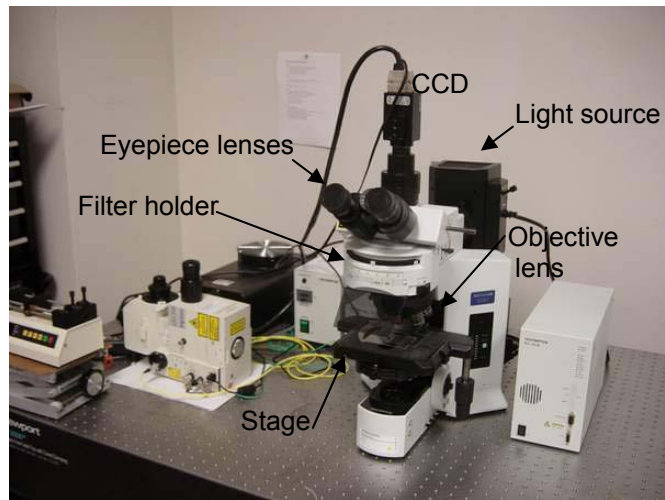


(a) Computer system with frame grabber

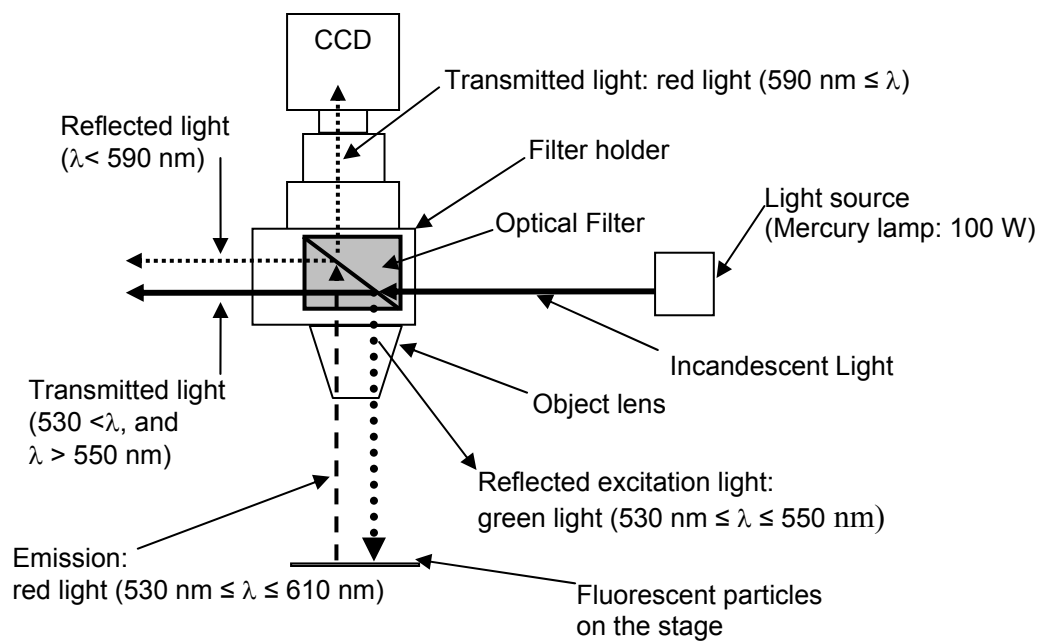


(b) CCD with macro lens

Fig. 7.6. Image recording/processing system.



(a) Reflected fluorescent microscope, Olympus BX61



(b) The schematic illustration of light path

Fig. 7.7. Particle imaging system of reflected fluorescent microscope.

equipped with CCD whose spatial resolution is  $1024 \times 1024$  pixels. The captured images of particles are recorded by computer for further analysis.

Figure 7.7-b schematically illustrates the unique way of detecting subjects. As mentioned in previous chapter, distinguishing object with background needs to achieve a contrast. The conventional method of reflected microscope to achieve contrast is to detect reflected light of illumination by objects. This method of achieving contrast has limited capacity to detect small particles since the intensity of smaller particle is too weak to be seen. Furthermore, if there are foreign particles with subjects, such as dusts, on the surface of investigated area, it is impossible to distinguish whether it is dust or subject. Using reflected fluorescent microscope can resolve above problems. It has special optical filters in its filter holder. The applied optical filter is a kind of beam splitters. This beam splitter has functions of reflecting and transmitting a specific wavelength of light. During research, applied fluorescent is the Rhodamine 590 whose the maximum excitation wavelength is 530 nm (green) and the maximum emission wavelength is 560 nm (red). To detect this fluorescent particle, a special filter is applied to reflect only green light from an incandescent light of mercury lamp to specimen stage and to transmit red light from fluorescent particles to CCD as shown in Fig. 7.7-b. Thus, only fluorescent particles can be detected by reflected fluorescent microscope.

### **7.1.5 Particle Generation System**

The particle generation system has two components; monodisperse particle generator (VOAG) and dust feeder. To analyze the performance of VI and characterize

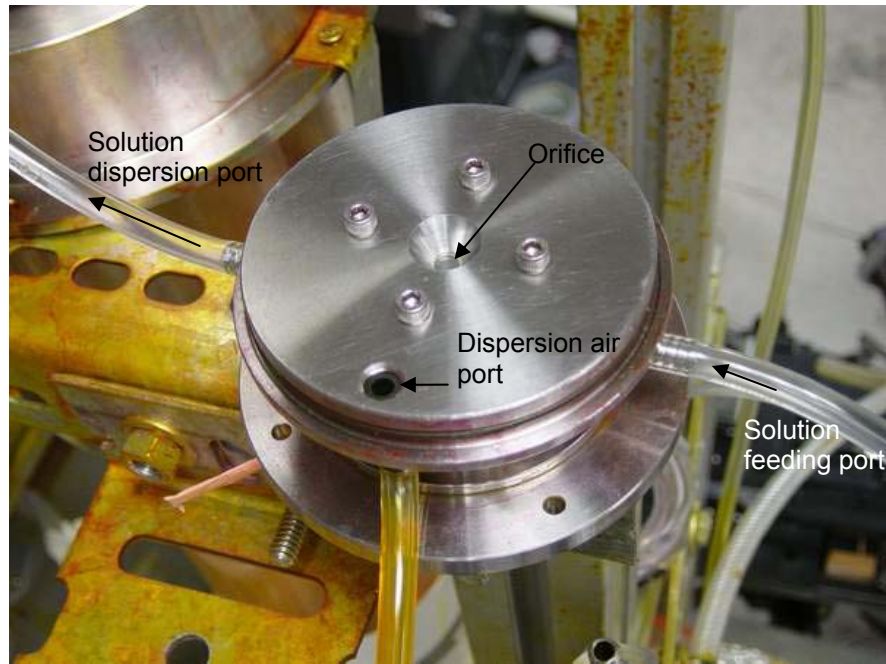
particle behavior as a function of particle size, the size and the monodisperse of generated particle are critical. Without these, analysis is not possible.

The particles that will be used as references are generated by VOAG system shown in Fig. 7.8. As explained in previous chapter, under given conditions of the flow rate and the concentration of solution, the orifice diameter, and the frequency of piezoelectric crystal, particle size and monodisperse can be controlled. During experiments, particle size is controlled by the concentration of solution and two different sizes of orifice under a fixed flow rate of solution. The applied orifice diameters are 10  $\mu\text{m}$  or 20  $\mu\text{m}$ . The status of monodisperse distribution is controlled by the frequency generated by signal generator. Several different sizes of fluorescent particle ranging from 1.2  $\mu\text{m}$  to 9  $\mu\text{m}$  are generated to satisfy research objective. The different size of generated monodisperse particles is applied to investigate collecting efficiency of VI and the trajectories of particles under different Stokes numbers.

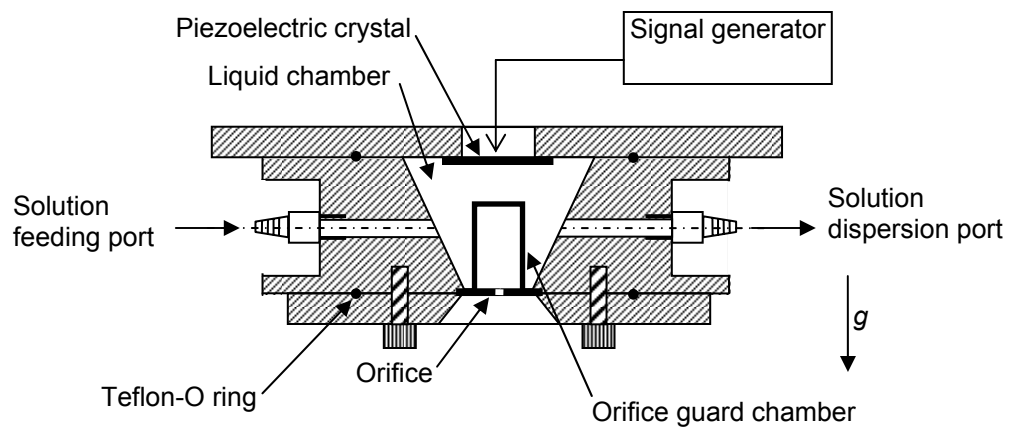
The applied material of fluorescent particles generated by VOAG is Rhodamine 590 whose density is 1.35  $\text{g}/\text{cm}^3$  manufactured by Excitation Inc. for dye laser. The reasons of selecting this dye are following:

1. Soluble

It can be totally dissolved in ethanol. Thus it can be used by VOAG resulting generation of solid particle as explained at the principle of VOAG in Chapter VI.



(a) VOAG head



(b) Cross-sectional view

Fig. 7.8. VOAG system.

## 2. The Characteristic of Spectrum

The characteristic spectrum is perfect for Nd:Yag laser with wavelength of 532 nm (green) since it is excited at 530 nm (green) and emits 560 nm (red).

Several different concentrations of solution (solute: Rhodamine 590, solvent: ethanol) are prepared. The calibration of particle size as a function of solution concentration has been conducted before running experiments. Table 7.2 shows equivalent particle sizes for precursor powder and Rhodamine 590 for a given Stokes number and designed air flow rates (10.6 m/sec for nozzle velocity). The density for precursor powder and Rhodamine 590 is  $3 \text{ g/cm}^3$  and  $1.35 \text{ g/cm}^3$ , respectively.

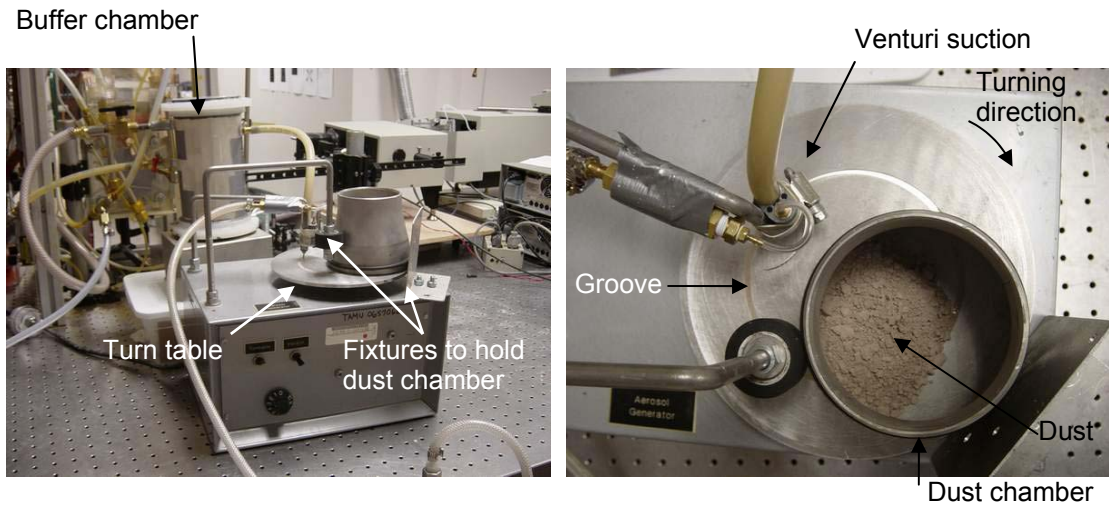
The dust feeder is applied to supply the controlled amount of mass loading into VI to investigate the interaction between particles to optimize mass loading condition. Figure 7.9 shows the apparatus of the dust feeder applied in research. In Fig. 7.9, a turn table has a groove that contains Arizona Road Dust (ARD) which is applied during research, and suction part has a venturi. The RPM of a turn table is controlled by motor. When turn table rotates, the dust chamber containing a stack of ARD is fixed by two fixtures. Thus, the dust chamber evenly levels the height of dust that is filled in the groove supplying the same amount of dust to the suction part. The concentration of dust particle can be controlled by the RPM of turn table and suction air pressure. The different mass loadings have been calibrated.

Since the particle size distribution of ARD is polydisperse, ARD can not be used as a reference particle for the purpose of analysis. Figure 7.10 shows the particle number

Table 7.2

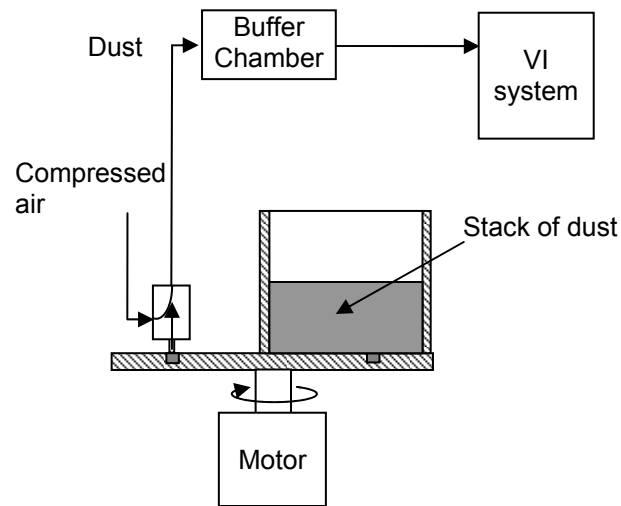
Equivalent particle sizes for precursor and Rhodamine 590 for a given Stokes number and designed air flow rate (10.26 SCFH)

Stokes Number	Precursor Powder [ $\mu\text{m}$ ]	Rhodamine 590 [ $\mu\text{m}$ ]
0.30	0.658	0.981
0.50	0.850	1.267
0.82	1.089	1.623
1.00	1.202	1.792
1.50	1.472	2.195
2.00	1.700	2.534
4.00	2.404	3.584
8.00	3.400	6.068
16.00	4.808	7.168
25.00	6.010	8.960



(a) General apparatus

(b) Top view



(c) Cross-sectional view

Fig. 7.9. Dust feeder system.



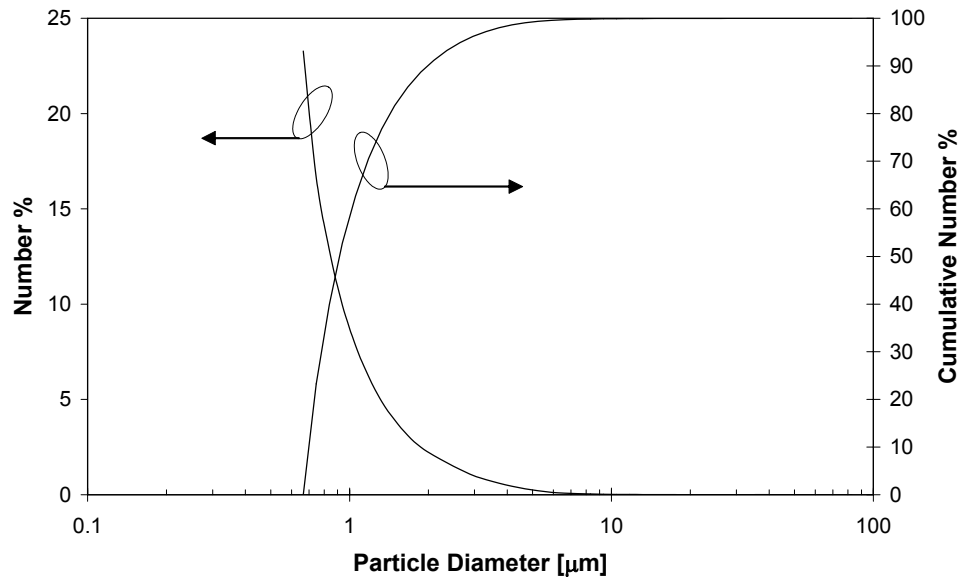


Fig. 7.10. Particle distribution of Arizona Road Dust (from Powder Technology Inc., Burnsville, MN).

distribution of ARD from manufacturer. In Fig 7.10, the particle size distribution is between  $0.666 \mu\text{m}$  and  $89.13 \mu\text{m}$ . Its volume mean and median diameter is  $8.909 \mu\text{m}$  and  $8.927 \mu\text{m}$ , respectively. The main purpose of using ARD is the background signal for investigating particles' interaction to optimize mass loading condition for current VI system. To do this, ARD will be mixed with monodisperse fluorescent particle generated by VOAG for the analysis as it was previously shown in Fig. 6.7. The particle size of the generated fluorescent particle by VOAG is little larger than 100% cutoff size. Theoretically, this particle should not be detected in major flows. It, however, can be detected at the major flow because of the interaction between ARD particles. Thus,

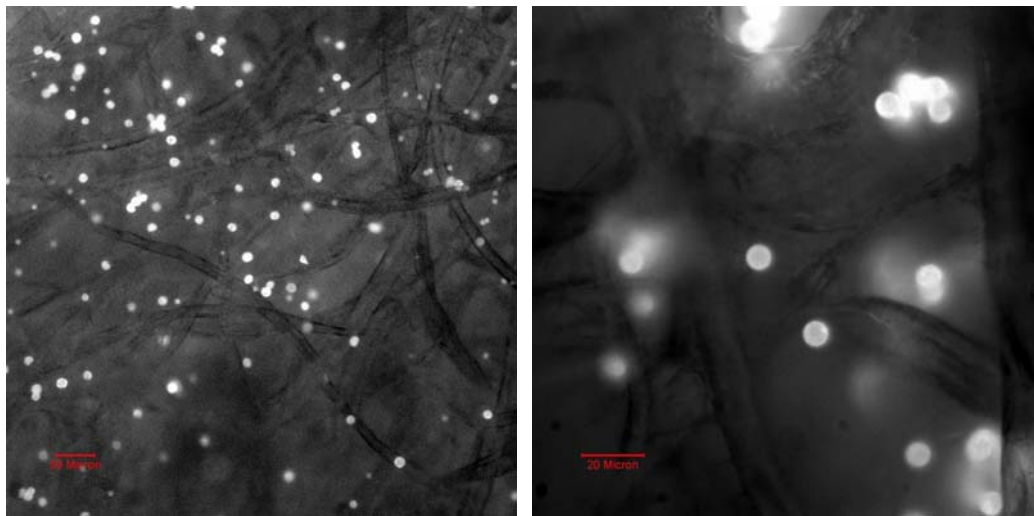
optimized mass loading condition where the interaction between particles is minimized can be found by measuring frequency of detecting fluorescent particles.

## **7.2 Verification**

### **7.2.1 Verification of Particle Size and Monodisperse Distribution**

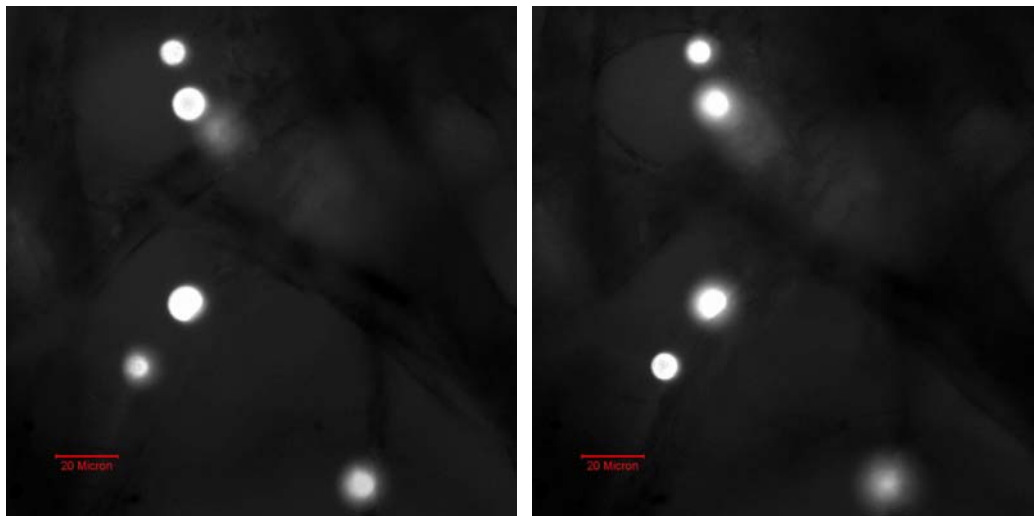
Without proper knowledge on particle size, analysis can not be achieved. Thus, the size of particle has been measured and the monodisperse distribution has been verified before and after taking experiments to ensure the credibility of experimental results by using microscope. During calibration procedure, it is found that the most preferable frequency for monodisperse condition is around 22,000 Hz.

At the initial stage of research, particles collected by air filter paper are investigated to determine monodisperse distribution and particle size. The filter paper is placed on the stage of microscope and illuminated by light source of microscope. Using filter paper, however, causes difficulties to determine monodisperse shape and to measure particle size accurately. Figure 7.11 captured by CCD installed in microscope explains problem that occurs during investigations. The captured particles shown in Fig. 7.11 is the diameter of 9  $\mu\text{m}$  of fluorescent particles generated by VOAG and monodisperse. In Figs. 7.11-a and 7.11-b, particles do not look uniform, although a generated particle has monodisperse distribution. Furthermore, some particles stick together that looks like doublet instead of single particle. In Figs. 7.11-c and 7.11-d, the identical area is taken applying the different focal plane. Some particles look clear in Fig.



(a) Magnification of 10

(b) Magnification of 40



(c) Magnification of 40

(d) Magnification of 40

Fig. 7.11. Captured images of particles collected by filter papers (generated particle size is about 9 micron, image is captured by microscope and recorded by CCD having resolution of 1024×1024).

7.11-c, but they become blur in Fig. 7.11-d. These problems occur because of following 2 reasons:

1. The Surface of Filter Is Not Flat

When images of particles are captured, determining the uniformity of generated particle size is very difficult since the particles located out of focal plane have blur resolution.

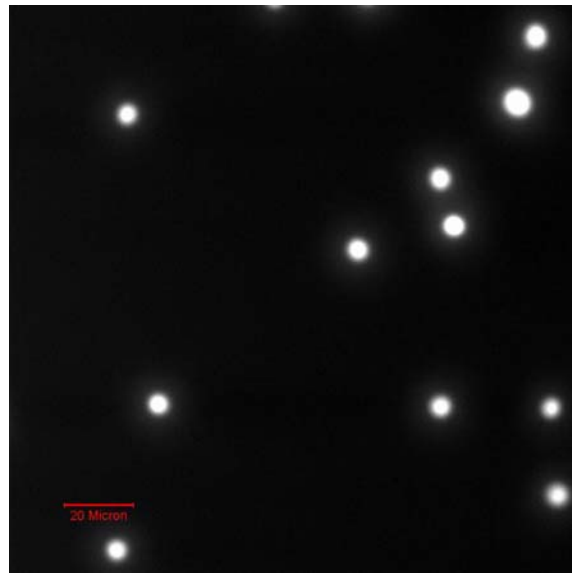
2. The Size of Particle Is Smaller Than That of Filter Fiber

Since generated particle is smaller than that of filter fiber, particles do not sit on the surface of filter as shown in Figs. 7.11-b and 7.11-d. They pass through the matrix of fibers and are located beneath fibers. This increases uncertainty of size measurement. The other problem is that they stick together during their movement in the fibers resulting in difficulties to determine the status of monodisperse distribution.

Instead of collecting particles by filter, microscopic cover glass is applied to resolve above problems. Particles are collected by the cover glass located on the surface of observation window of minor flow. Since the surface of cover glass is almost uniform, better resolution of particles can be obtained. Figure 7.12 shows one of example images under the identical condition of Fig. 7.11. The generated particle size is 4.4 micron having standard deviation of 0.40. Comparing with Fig. 7.11, the resolution of Fig. 7.12 is much better than that of Fig. 7.11. In Fig. 7.12-a, the lower magnification lens ( $\times 10$ ) is applied to investigate a general condition of generated particle configuration. The higher



(a) Magnification of 10



(b) Magnification of 40

Fig. 7.12. Images of generated particle settled on the surface of microscopic cover glass located on the observation window glass at minor flow (generated particle size is about 4.4 micron; image is captured by microscope and recorded by CCD having resolution of  $1024 \times 1024$ ).

magnification lens ( $\times 40$ ) shown in Fig. 7.12-b is applied to measure particle size and monodisperse condition.

The image processing by software is applied to measure particle size. The applied software is '*ImageJ*' from a public domain image processing and analysis program developed at the Research Services Branch (RSB) of the National Institute of Mental Health (NIMH), part of the National Institutes of Health (NIH). This software offers analysis tool to measure the area of particle. Once areas of particles are obtained, diameters of particles are converted. More than 20 particles per each investigation are examined to confirm their diameter. Table 7.3 shows results on average particle diameter and standard deviation for each investigation. The average standard deviation shows the value of 0.552. The standard deviation of current system is relatively good comparing with Berglund and Liu (1973) who claimed 1.014 as the average geometrical standard deviation for particle range of 0.5 – 50  $\mu\text{m}$ .

Table 7.3

Average diameter and standard deviation of particles generated by VOAG

Average $d_p$	1.2 $\mu\text{m}$	4.0 $\mu\text{m}$	4.4 $\mu\text{m}$	4.8 $\mu\text{m}$	5.4 $\mu\text{m}$	7.3 $\mu\text{m}$	9 $\mu\text{m}$	Average $\sigma$
$\sigma$ [ $\mu\text{m}$ ]	0.33	0.39	0.40	0.42	0.32	0.98	0.6	0.491

### 7.2.2 Verification of Detecting Fluorescent Image under Mixture with Dust

The visibility of images of fluorescent particles under the condition of loading a mixture of ARD and fluorescent particles has been verified. To verify this, two separated experimental conditions have been conducted. They are:

#### 1. Loading ARD Only

Under this condition, images of ARD have been taken with and without optical filter in order to make sure that ARD can not be detected using optical filter. Results shown in Fig. 7.13 confirm that ARD can not be detected under optical filter. Image of ARD shown in Fig. 7.13-a is recorded by Mie-scattering method without optical filter. Figure 7.13-b is recorded using optical filter (notch filter which blocks only wavelength of 532 nm) located between CCD and test section.

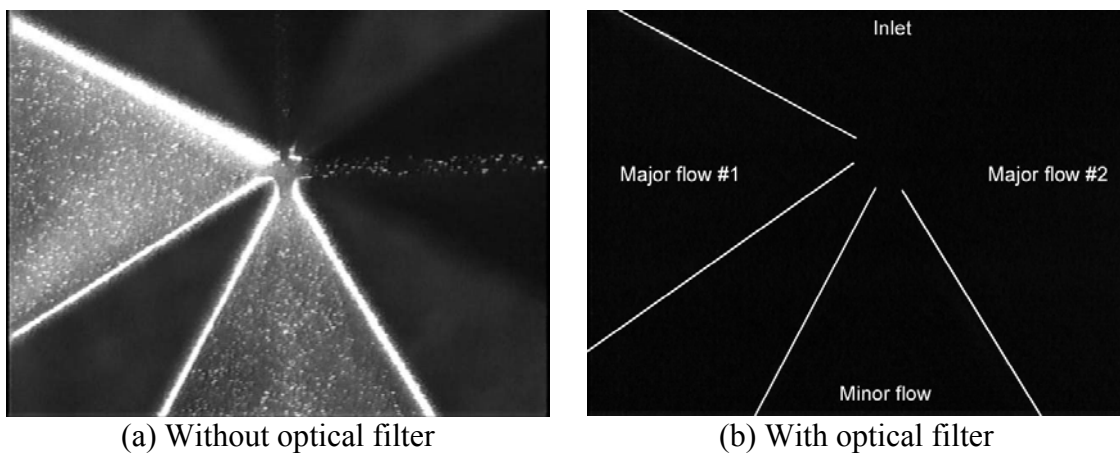


Fig. 7.13. Results of verification on detecting images under loading ARD only using optical filter.

## 2. Loading Mixture of ARD and Fluorescent Particles

The images of fluorescent particles have been detected using optical filter when mixture of ARD and fluorescent particles is loaded. This confirms that experimental setup is well established to pursue the objective of current research. Result is shown in Fig, 7.14. In Fig. 7.14, the image is identical as Figure 7.13-(a) if optical filter is not applied.

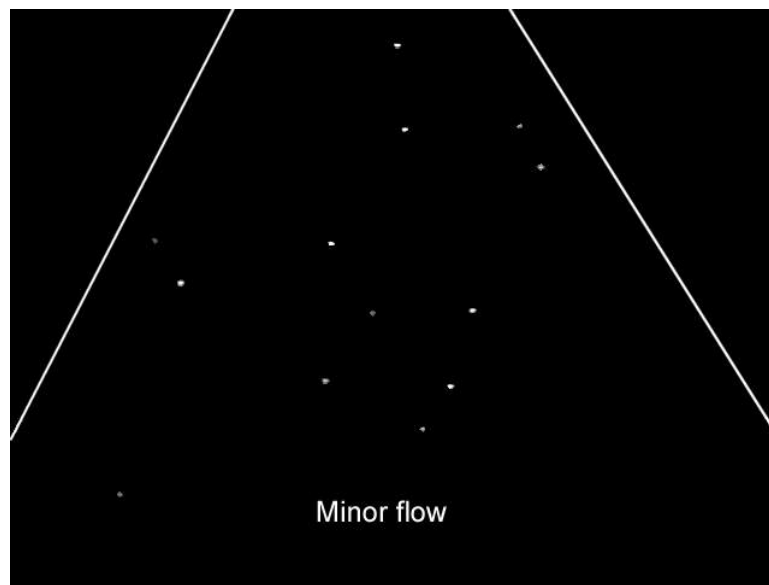


Fig. 7.14. Detecting fluorescent particles only using optical filter when mixture of ARD and fluorescent particles is loaded (actual image is identical as Fig. 7.13-a if optical filter is not applied).



## CHAPTER VIII

### RESULTS AND ANALYSIS

Chapter VIII will show the results of visualization on the characterization of convective transport behavior as a function of Stokes number in VI. The analysis from results will be also introduced.

#### 8.1 Collecting Efficiency of VI

The collecting efficiency ( $\eta$ ) of VI has been investigated to evaluate its performance. The major parameter to be used as a reference value for collecting efficiency is Stokes number at the nozzle from Eq. (6.1).

$$Stk = \frac{d_p^2 \rho_p V_{nozzle}}{9 \mu_g w} \quad (8.1)$$

where  $d_p$ ,  $\rho_p$ ,  $V_{nozzle}$ ,  $\mu_g$ , and  $w$  is the particle diameter, the particle density, the nozzle velocity of gas, the viscosity of a gas, and the characteristic length (the width of nozzle throat, 0.3 mm), respectively. In Eq. (8.1), Stokes number is the only function of the particle size and the nozzle velocity under given experimental environments (identical geometry, gas medium, and material of particle). By modifying air flow rate and particle size, Stokes number can be varied. Table 8.1 shows experimental conditions to vary Stokes number in order to gather data on collecting efficiency of current VI system. In

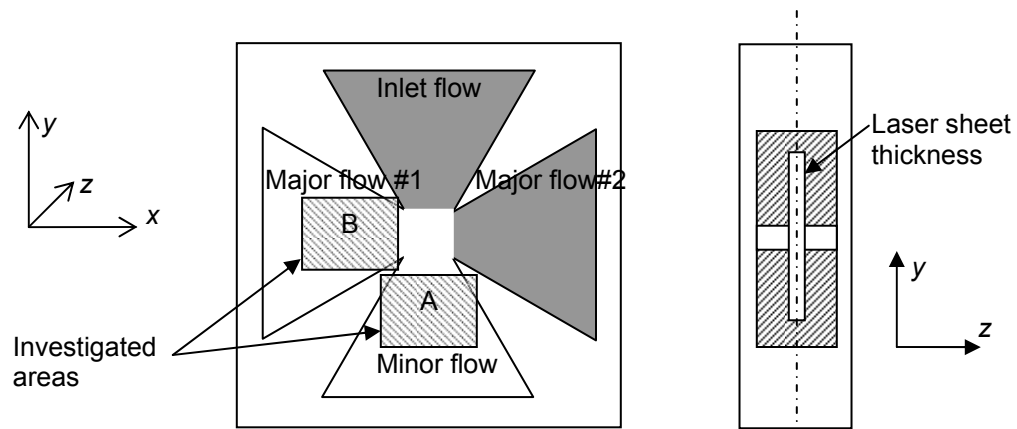
Table 8.1, two parameters, nozzle throat velocity ( $V_{\text{nozzle}}$ ) and particle size ( $d_p$ ), are modified to change Stokes number.

Table 8.1

Experimental conditions of particle sizes and velocities to vary Stokes numbers for gathering data on collecting efficiency (applied solid particle is fluorescent)

Stk.	0.42	0.72	0.81	0.92	1.00	7.20	9.08	16.60	25.00
$d_p$ [mm]	4.6	1.2	1.2	1.2	1.2	4.8	5.4	7.3	7.3
$V_{\text{nozzle}}$ [m/s]	0.67	16.45	18.39	21.18	22.84	10.59	10.59	10.59	15.95
Re	14.2	348.4	389.4	448	483	224	224	224	337

The frequency of detecting numbers of particles is measured at a downstream of minor flow and major flow #1 shown in Fig. 8.1 by means of Mie-scattering method. In Fig. 8.1-a, two rectangles labeled as A and B are the areas of investigation. The Nd:Yag pulsed laser illuminates the center plane of the VI in depth direction. The thickness of laser sheet is about 1.5 mm. Figure 8.1-b shows the example of captured images of detecting particles. Once images are recorded by VHS tape and converted into digital file by computer, the number of particle under a given time is counted for both minor and major flow #1. For example, 15 particles are captured in Fig. 8.1-b. When counting numbers for given frames is done, the number of particles per



(a) Areas of investigations for counting number of particles



(b) The example image of captured particles at A

Fig. 8.1. Areas of investigation for collecting efficiency of current VI system and example of Mie-scattering image of captured particles (applied light is Nd:Yag laser having 7 nsec of a single pulse and 10 Hz of repetition).

frame for each flow is obtained. Table 8.2 shows results of detecting frequency for major flow #1 and minor flow. Figure 8.2 shows one example of detecting frequency for a given Stokes number of 0.72. The average number of particles per frame for minor flow and major flow #1 is 1.08 and 0.96, respectively. The standard deviations are 0.34 for minor flow and 0.37 for major flow #1.

Table 8.2

Detected particle number density for both major and minor flow for Stokes number ranging from 0.42 to 25.0

Stokes number (Stk)	Major flow #1		Minor flow		Collecting efficiency at minor flow
	Average number of particles per frame	Total number of particles / Total number of frames	Average number of particles per frame	Total number of particles / Total number of frames	
0.42	0.539	302 / 560	0.175	98 / 560	13.96
0.72	0.96	1028 / 1071	1.08	896 / 830	35.99
0.81	0.70	406 / 582	1.07	646 / 603	43.43
0.92	0.41	331 / 815	3.03	1150 / 380	78.84
1.00	0.082	134 / 1642	2.36	1392 / 591	93.52
7.2	0.107	127 / 1187	10.105	1253 / 124	97.93
9.08	0.07	81 / 1202	15.01	2086 / 139	99.11
16.0	0.007	8 / 1200	22.00	594 / 27	99.94
25.0	0.003	4 / 1213	13.67	902 / 66	99.95

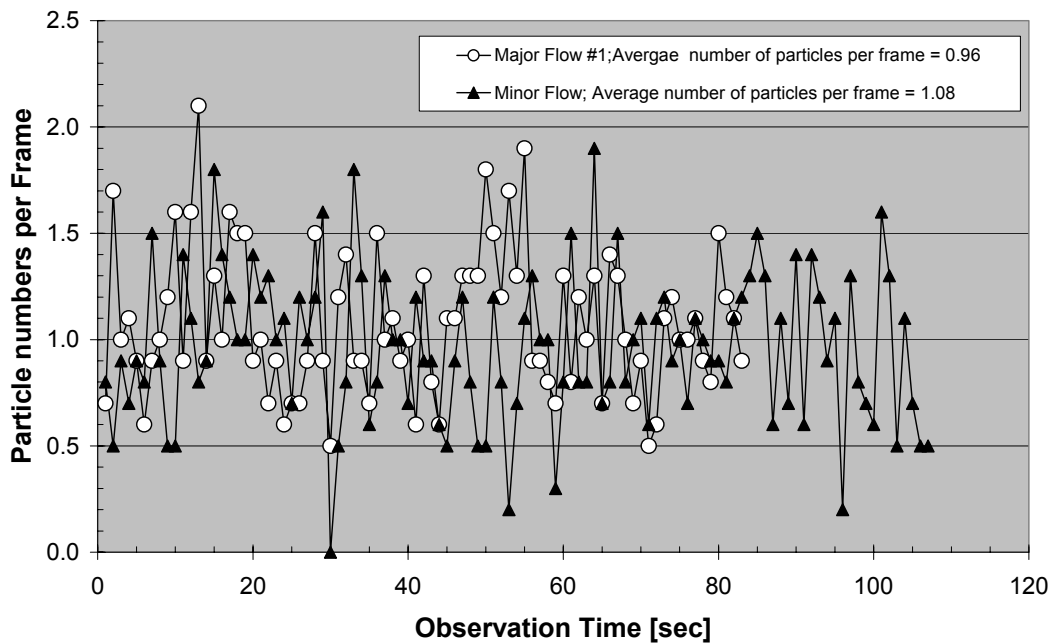


Fig. 8.2. Frequencies of detecting particles at major and minor flow for Stokes number of 0.72 ( $\sigma_{\text{std, minor}} = 0.34$ ,  $\sigma_{\text{std, major \#1}} = 0.37$ ).

To obtain collecting efficiency for current system using current experimental setup, following assumption is established: Numbers of particles at major flow # 2 is the same as those of major flow #1. Since the major flow #2 is not illuminated, the numbers of particles can not be obtained. Thus, the assumption that the numbers of particles of major flow #2 is the same as those of major flow #2 since current VI system is symmetric. The final collecting efficiency of the current system can be calculated as

$$\eta_{\text{major flows}} = \frac{\text{Avg.\#of major flow\#1 per frame} \times 2}{\text{Avg.\#of major flow\#1 per frame} \times 2 + \text{Avg.\#of minor flow per frame}} \quad (8.2)$$

The result of experiments on evaluation of collection efficiency is shown in Fig. 8.3.

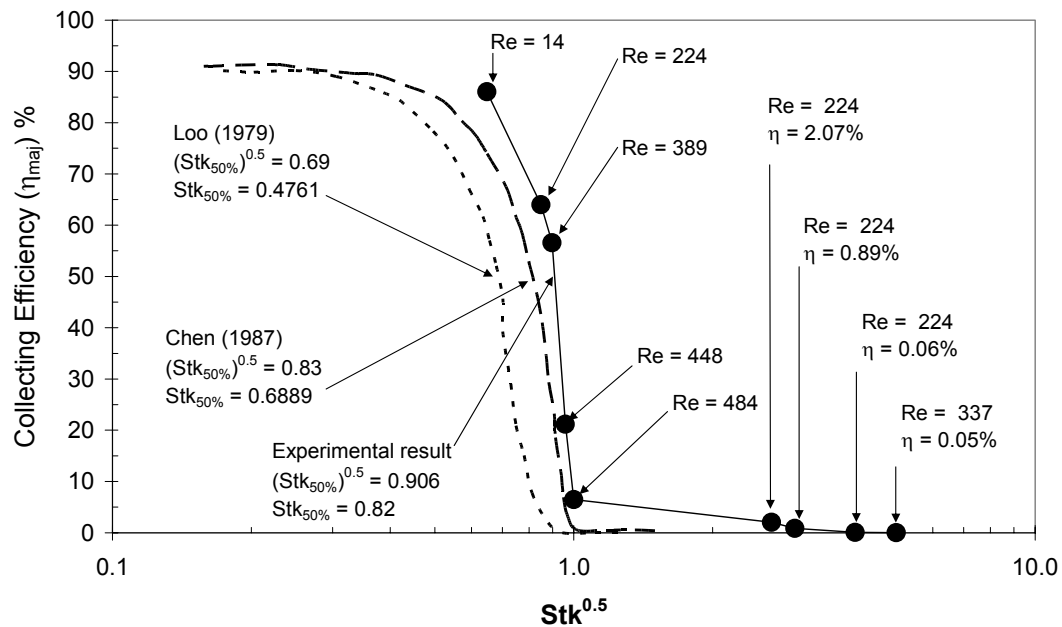


Fig. 8.3. Result of evaluating collecting efficiency of major flow of VI.

In Fig. 8.3, the results of Loo and Adachi (1979) and Chen and Yeh (1987) are introduced for the purpose of comparison. The result of experiments on collecting efficiency is quite reasonable since the trend line of efficiency curve looks similar to others. The current VI system, however, has very sharp cutoff curve than others indicating that current system has very narrow cutoff size distribution than others. This satisfies the purpose of using current VI system to sort smaller precursor particles from raw material ensuring much better efficiency on collecting smaller particles. The Stokes number of 50% cutoff for current system is found as 0.82, equivalent to diameter of 1.09  $\mu\text{m}$  of precursor powder whose density is 3  $\text{g}/\text{cm}^3$  under a designed operation condition.

At lower Stokes number, the collecting efficiency can not reach at 100% because of inherent of VI system. As the principle of VI was introduced in Chapter VI, 10% of inlet flow goes to minor flow resulting 10% of smaller particle can not be separated by two major flows. Thus, maximum collecting efficiency of major flow for smaller particles is 90 %.

For larger particles (higher Stokes numbers), theoretically these particles can not be found in major flow. However, the results show larger particles have been observed in major flows. In Fig. 8.3, the collecting efficiency of fluorescent particles for Stokes number of  $d_p = 3.23 \mu\text{m}$  (Stk = 7.2),  $d_p = 3.61 \mu\text{m}$  (Stk = 9),  $d_p = 4.81 \mu\text{m}$  (Stk = 16), and  $d_p = 6.01 \mu\text{m}$  (Stk = 25) under given designed condition are 2.07, 0.89, 0.06, and 0.05, respectively. As the importance of applying smaller particles in powder state in the process of PIT is discussed in Chapter VI, entering larger particles into major flow makes detrimental effect on performance and lifetime of superconductor wire. To resolve this problem, the trajectories of different particle sizes investigated by means of visualization will be discussed in next section. By knowing problem, solution can be made to enhance the performance of current VI system.

## **8.2 Visualization of Particle Trajectory**

### **8.2.1 Lower Stokes Number**

To investigate the characteristics of convective transport behavior, a particle motion, in the VI system, continuous wave laser is applied as a light source. Three different sizes, 4  $\mu\text{m}$ , 4.8  $\mu\text{m}$  and 9  $\mu\text{m}$ , of monodisperse particles are applied.

Figure 8.4 shows particle trajectory images at relatively lower Stokes number,  $Stk = 0.2$  with  $4.8 \mu\text{m}$  diameter particles. The individual trajectory represents the particle path for the period of 33 ms per image at 30 frames-per-second recording rate. Figure 8-a shows two distinctively different particle paths, the particle *P1* travels to the minor flow region and the particle *P2* deflects to enter the major flow region. Note that the laser illumination is originated from the bottom of the image and only a narrow strip of the laser sheet with the same width as the nozzle throat penetrates into the inlet region. Therefore, only those incoming particles staying within the narrow laser strip for the entire recording period (33 ms) can be fully visualized in the image and any other particles flowing into the narrow strip from the outer regions of slower flow speeds. The former particles carry higher inertia because they are carried by the higher flow speed of the central narrow region and tend to maintain their trajectory into the minor flow region, whereas the relatively lower inertia of the latter particles in the slower flow speeds make them more susceptible to bend into the major flow region. From this observation, it is conjectured that the inlet flow region is divided into two: (A) the central region where the particle trajectories maintain their relatively linear paths into the minor flow region, and (B) the outer region where the particle trajectories follow the bending air flows into the major flow regions. Figures 8-b and 8-c more apparently show the straight particle trajectories staying in the central region entering into the minor region and the bending particle trajectories along the outer region entering into the major region, respectively.



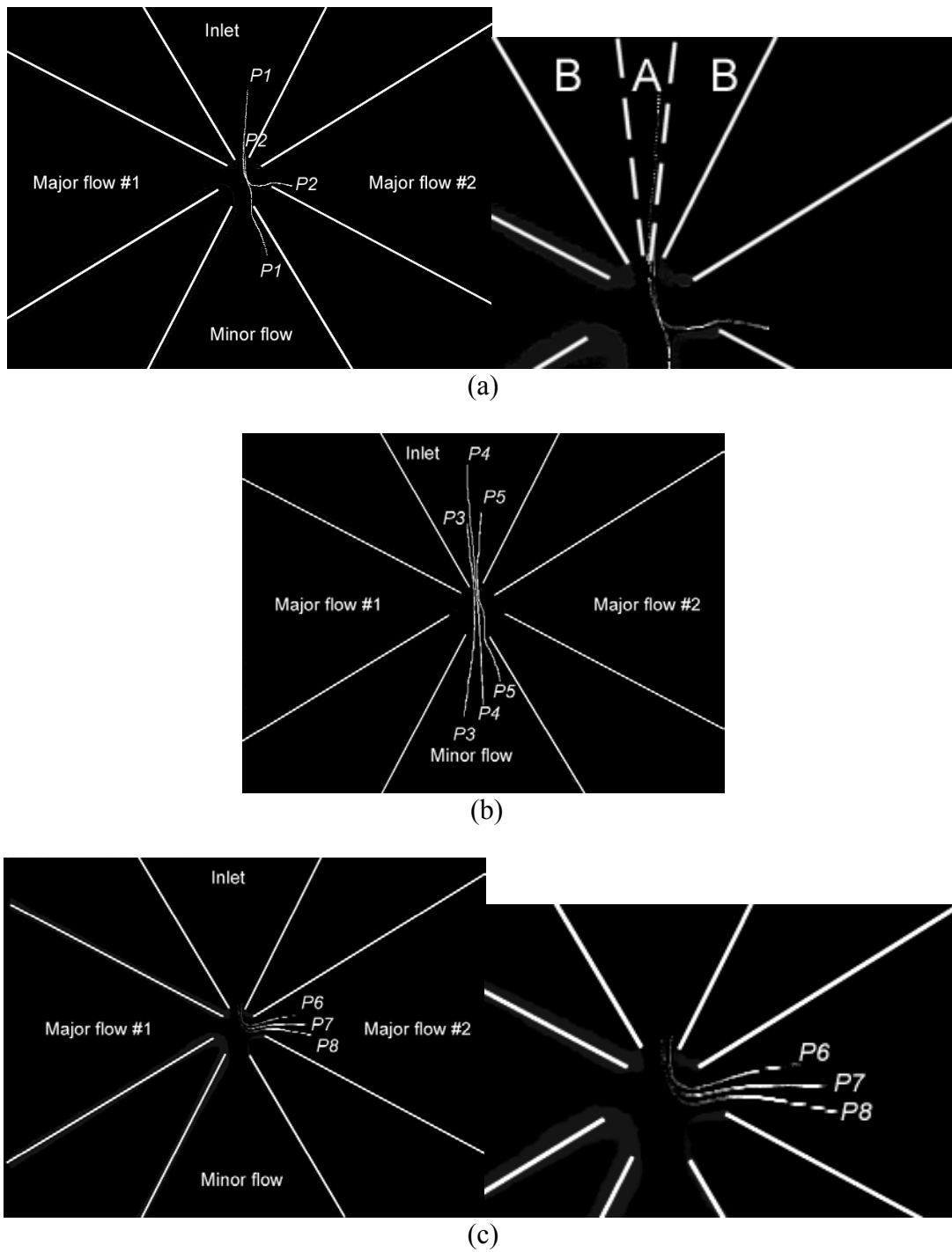


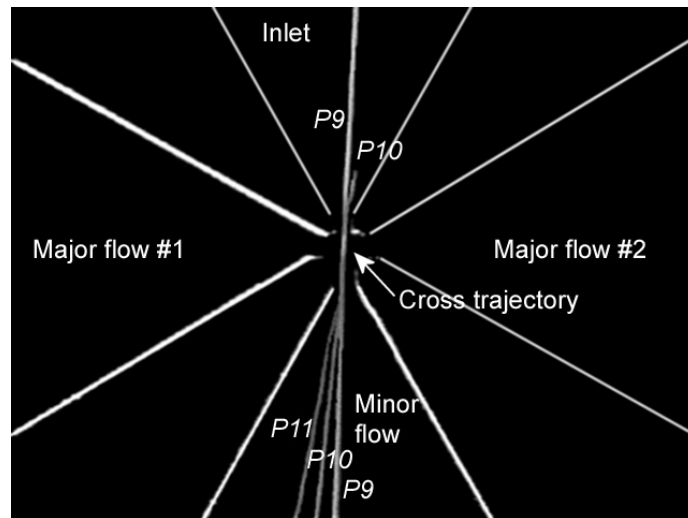
Fig. 8.4. Visualized images of lower Stokes number ( $d_p = 4.8 \mu\text{m}$ ,  $\text{Stk.} = 0.2$ ,  $\dot{V}_{air} = 0.29 \text{ SCFH}$ ,  $\text{Re} = 6.3$ ).

### 8.2.2 Higher Stokes Number

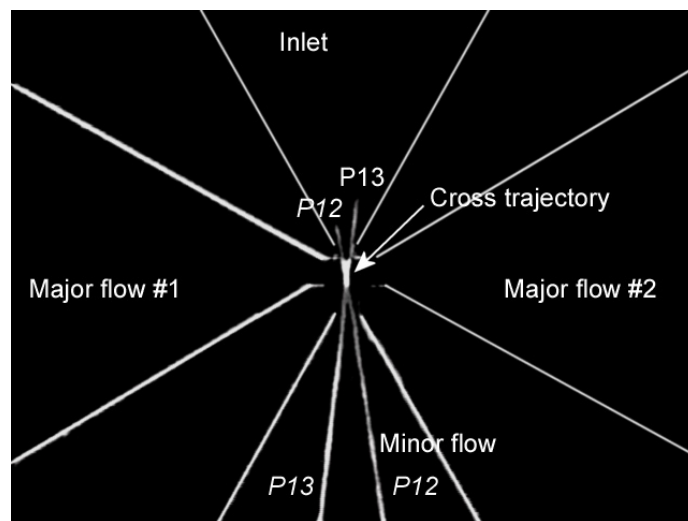
The result of visualization on larger particles is shown in Fig. 8.5. The notable difference between lower and higher Stokes number of particles is the cross trajectory in the intersection area which was not observed in the case of lower Stokes numbers (Figure 8.4). This indicates that the aforementioned two separately considered inlet sub-regions, the central region and the outer region, are no longer distinctive. The extremely high inertial forces of particles at such a high Stokes number keep the particle trajectory straight maintaining its incoming direction without being affected by the major flows. Figure 8.5-a show straight flight of particles into the minor region coming along the central region and 8.5-b shows straight flight of particles coming along the outer region.

### 8.2.3 Defect Particles for Higher Stokes Number

The result of collecting efficiency into major flow shown in Fig. 8.3, however, shows that even for sufficiently large Stokes numbers, a few defect particles can enter the major flow region. Figure 8.6 shows the visualized trajectories of defect particles. In Fig. 8.4, all defect particles approach the nozzle throat at excessively slow speeds creeping along the near-wall region. Figure 8.4-a shows a clear demonstration of the straight trajectory in the central region (Trajectory 1) and the defecting trajectory along the near-wall region (Trajectory 2) for the case of  $St = 10$ . Figures 8.4-b and -c show two defecting particle trajectories along the near-wall region entering the major region at extremely higher  $St = 50$ . It is now conjectured that the unexpected defecting particles occurring at sufficiently high Stokes numbers, against the known theory ideally



(a)



(b)

Fig. 8.5. Visualized images of higher Stokes number ( $d_p = 9 \mu\text{m}$ ,  $\text{Stk.} = 50$ ,  $\dot{V}_{air} = 20.33 \text{ SCFH}$ ,  $\text{Re} = 448$ ).

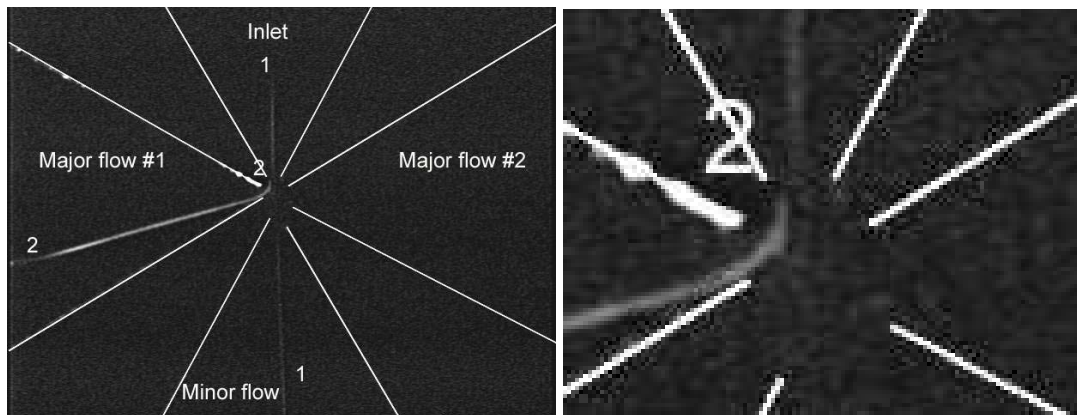
predicting zero defect, may be explained by the presence of relatively larger particles but with excessively low inertia creeping along the near-wall boundary of the inlet region and by their insufficient inertia allowing to bend their trajectories by the major flows.

Usually, when collecting efficiency for virtual impactor is considered, Stokes number which is calculated by the average velocity of air flow is applied. This average Stokes number, however, does not represent actual particle status since velocity profile is different depending on geometric configuration and flow condition (Schlichting, 1979). Thus, new parameter needs to be introduced to analyze characteristic of individual particle.

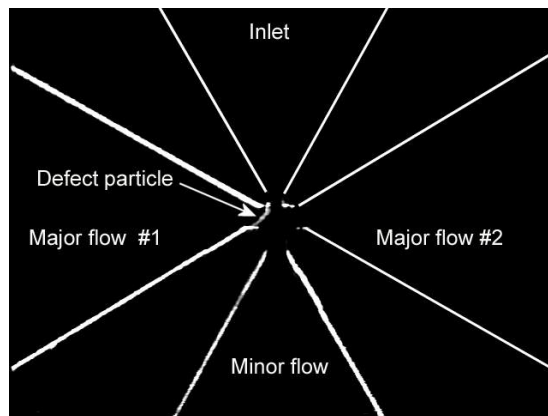
#### **8.2.4 Analysis of Defect Particles by Local Stokes Number**

Local Stokes number is introduced to investigate the state of particles as a function of location since average Stokes number can not explain defect particles as velocity profile is explained. The local Stokes number for a specific diameter size can be calculated since it is only function of velocity under identical experimental conditions. To investigate local Stokes number, the velocity profile of current system should be known.

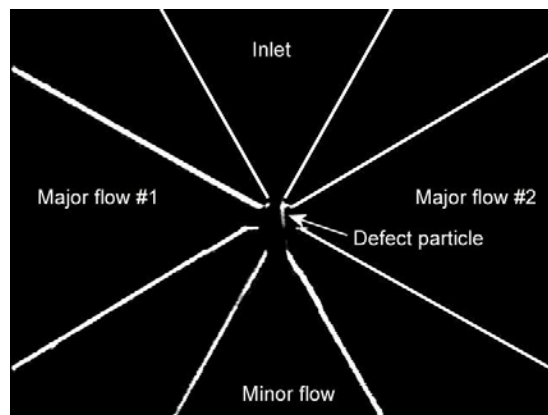
The velocity profile of current system ( $60^\circ$  converging flat plate flow) at the nozzle throat is calculated by '*Fluent*', commercial CFD program. The result is shown in Figure 8.7. In Fig. 8.7,  $h_y$  is the half of nozzle width, 0.15 mm. Air flow located  $\pm 0.1$  of  $y/h_y$  is the region A, central flow region, and the outer area is region B, as they are defined in previous section. For the purpose of comparison, the profile of parallel flat



(a)  $d_p = 4 \mu\text{m}$ ,  $\text{Stk} = 10$ ,  $\dot{V}_{air} = 20.33 \text{ SCFH}$ ,  $\text{Re} = 448$



(b)  $d_p = 9 \mu\text{m}$ ,  $\text{Stk} = 50$ ,  $\dot{V}_{air} = 20.33 \text{ SCFH}$ ,  $\text{Re} = 448$



(c)  $d_p = 9 \mu\text{m}$ ,  $\text{Stk} = 50$ ,  $\dot{V}_{air} = 20.33 \text{ SCFH}$ ,  $\text{Re} = 448$

Fig. 8.6. Visualized images of defect particles under higher Stokes number.

plate is also drawn under identical flow condition (10.26 SCFH of volume flow rate). What are the distinctive differences on velocity profile between current system and parallel plate flow are the thinner thickness of boundary layer and flat profile around central flow region for converging flow. The thickness of current system is much thinner than that of parallel plate indicating boundary effect is significantly reduced. The profile near central flow region becomes flatter resulting the maximum velocity is slower than that of parallel flat plate in order to satisfy the law of continuity. By applying the profile of Fig. 8.7, the results of local Stokes numbers will be shown in following three Figures.

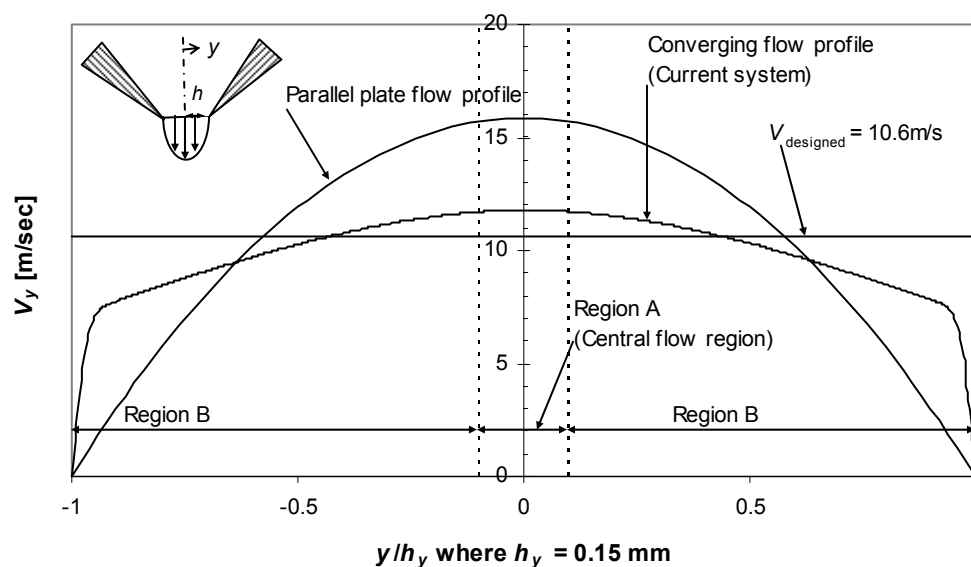
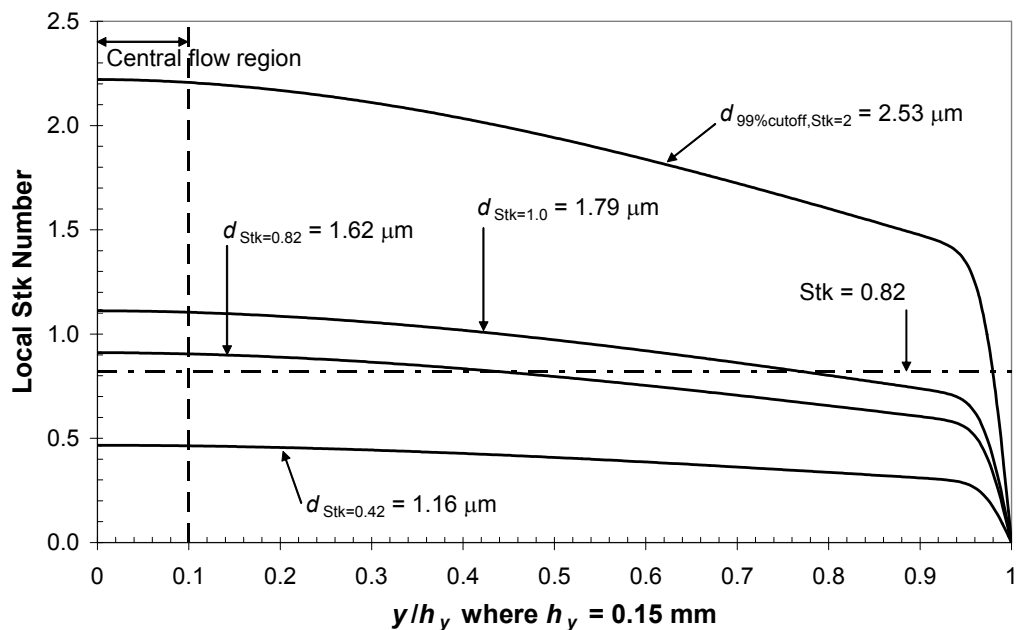


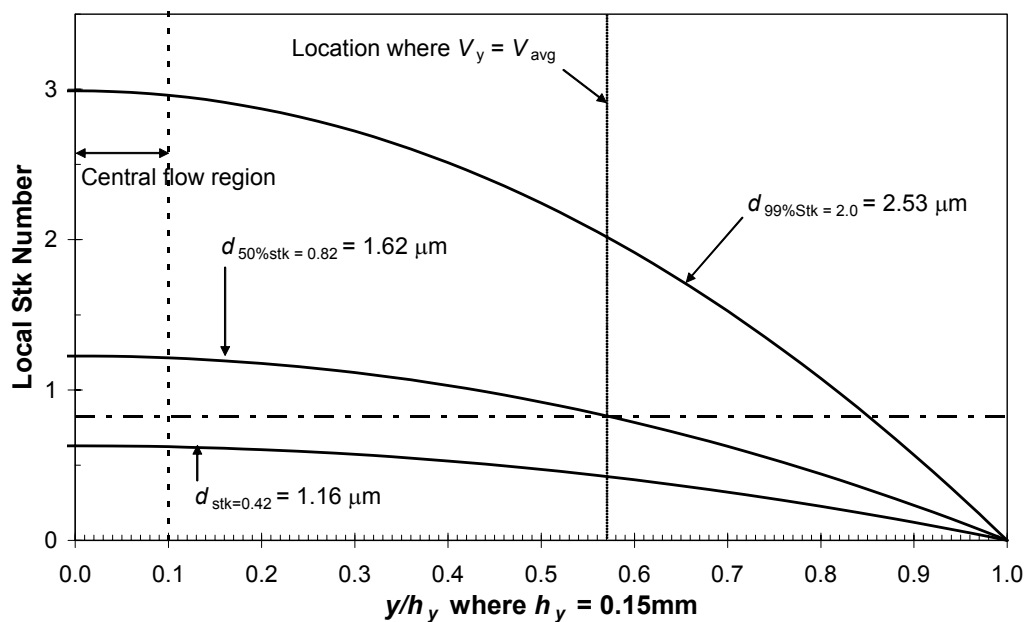
Fig. 8.7. Velocity profile of current VI system at the nozzle throat under designed flow condition (volume flow rate of 10.26 SCFH;  $60^\circ$  of converging parallel plate condition is drawn for the purpose of comparison).

Figure 8.8 shows local Stokes number for smaller particles by using two different profiles for the purpose of comparison. In Fig. 8.8-a for converging flow, analysis of local Stokes number for  $d_{p50\% \text{ cutoff}} = 1.62 \mu\text{m}$  shows similar result with the measurement result of collecting efficiency,  $\text{Stk}_{50\%}=0.82$ . For  $d_{p50\% \text{ cutoff}} = 1.62 \mu\text{m}$ , Figure 8.8 shows about 44% of particles located inner region of nozzle throat have higher local Stokes numbers (higher than 0.82). Among 48% of particles, 38% of particles are laden in region A. Although they are laden in region A, these particles, however, deviated from deflected air streams entering minor flow since their inertia is high according to their local Stokes number. Thus, it can be conjectured that Stokes number of 0.82 is reference value for the current system that particles having below this number can follow air streamlines and particles having above this number can not follow deflected air streams. For  $d_p = 2.53 \mu\text{m}$  which is designed 99% cutoff diameter of current system, the local Stokes number shows only 2% of particles has Stokes number lower than 0.82 which is close to the result of experiment (about 3% - 4%). The effect of geometric configuration (converging flow) on separating smaller particles can be identified by comparing the differences between Figures 8.8-a and -b. For smaller particles, local stokes numbers of converging flow inner region of nozzle throat become lower than those of parallel flow indicating collecting efficiency for smaller particle is enhanced. Figure 8.8-b shows that collecting efficiency of  $d_p = 1.62 \mu\text{m}$  for parallel flow condition is about 42% if conjectured reference value of Stokes number of 0.82 is correct.

Figure 8.9 shows local Stokes number of larger particles for converging- and parallel-flow. In Fig. 8.9, particles having Stokes numbers lower than 0.82 is defined as



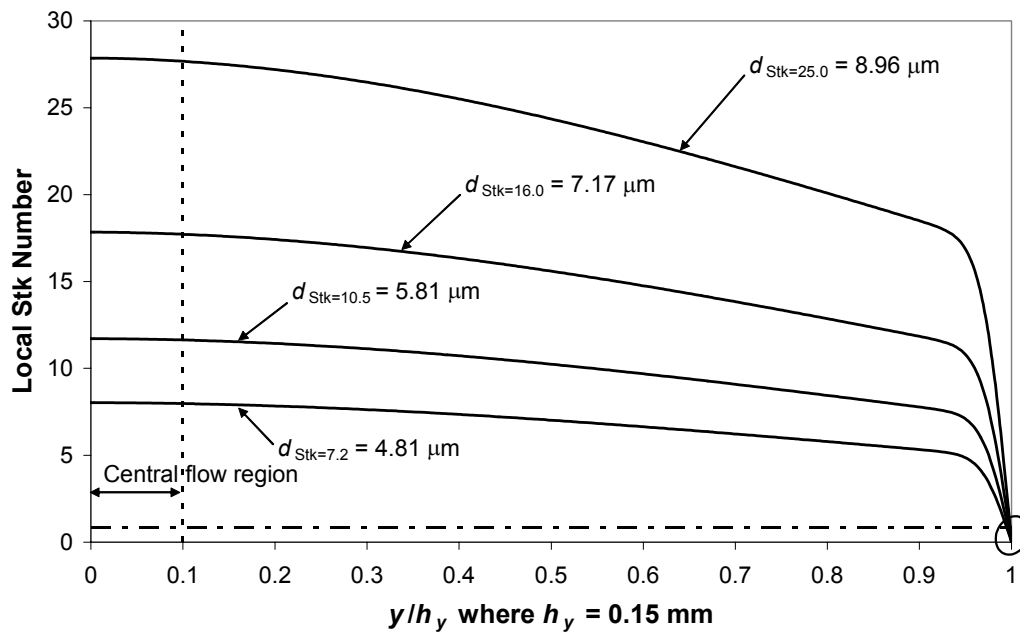
(a) Using profile of converging flow



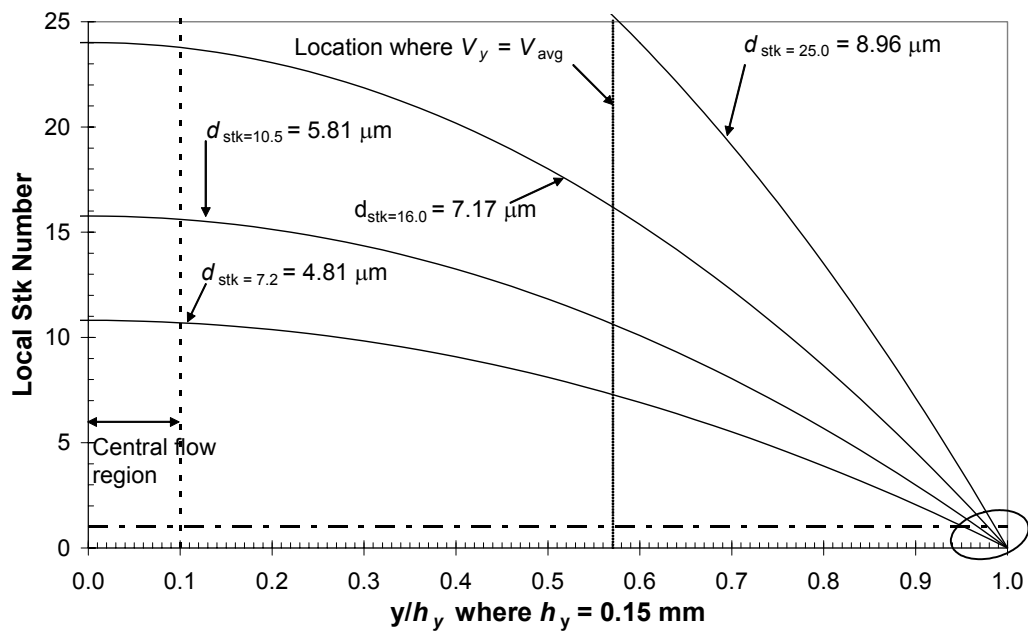
(b) Using profile of parallel flow

Fig. 8.8. Local Stokes numbers at nozzle throat for smaller particles under designed air flow rate of 10.26 SCFH.





(a) Using profile of converging flow



(b) Using profile of parallel flow

Fig. 8.9. Local Stokes number for larger particles under designed air flow rate of 10.26 SCFH.

defect particles since they enter into major flows. Figure 8.9 clearly shows the boundary layer has a significant effect on ratio of defect particles for larger particles. In Fig. 8.9-a, the possibility of having defect particles for  $d_p = 7.17 \mu\text{m}$  with Stokes number of 16 and  $d_p = 8.96 \mu\text{m}$  with Stokes number of 25 is 0.22 % and 0.14 %, respectively. Although these ratios shows little difference with the results of experiments (0.05% for  $d_p = 7.17 \mu\text{m}$  and 0.06 % for  $d_p = 8.96 \mu\text{m}$ ), the analysis of the local Stokes number looks reasonable to predict the effect of boundary layer which causes defect particles during separation. Figure 8.9 also explains the effect of geometric configuration on the efficiency of VI by comparing Figures 8.9-a and -b. Analytical defect ratios of current system are significantly reduced from 12% for  $d_p = 7.17 \mu\text{m}$  and 8% for  $d_p = 8.96 \mu\text{m}$  of parallel flow condition. Thus, it is concluded that the geometric configuration of converging flow condition can enhance the collecting efficiency for smaller particles and reduce the possibility of having defect particles for larger particles with respect to parallel flow condition since the velocity profile of converging flow has much thinner boundary layer and flat profile near the inner region. The circled area in Fig. 8.9-a is enlarged in Fig. 8.10.

From comparison between analytical result of local Stokes number and experimental results, introducing local Stokes number and selecting reference Stokes number as 0.82 for current system are quite reasonable methods to analyze the ratio of defect particles and collecting efficiency.

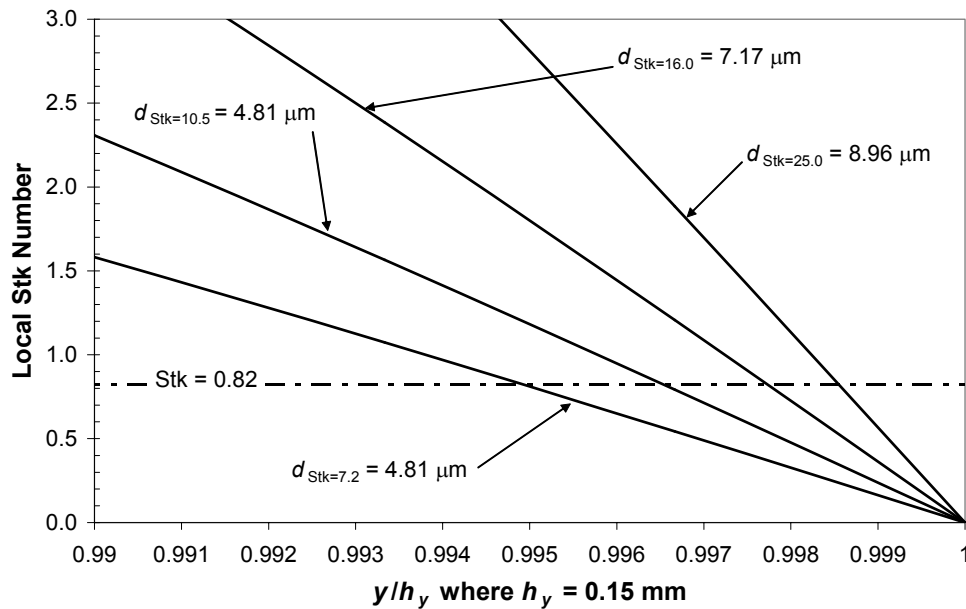
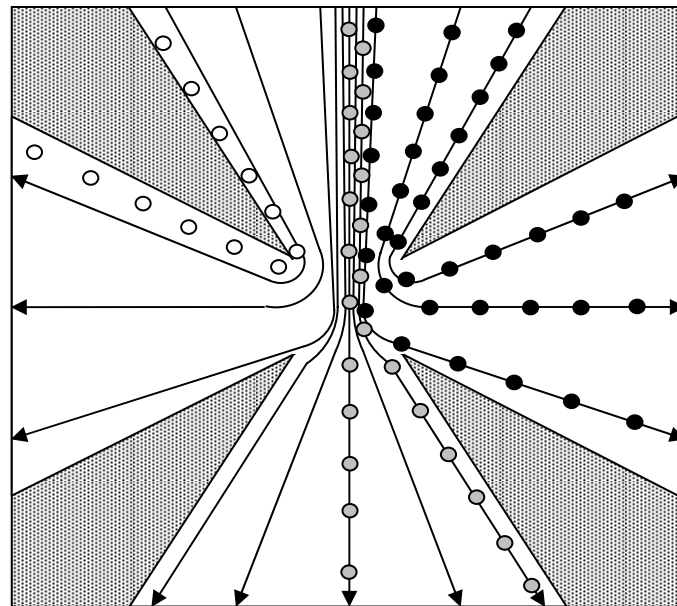


Fig. 8.10. Enlarged local Stokes number for larger particles using the velocity profile of converging flow.

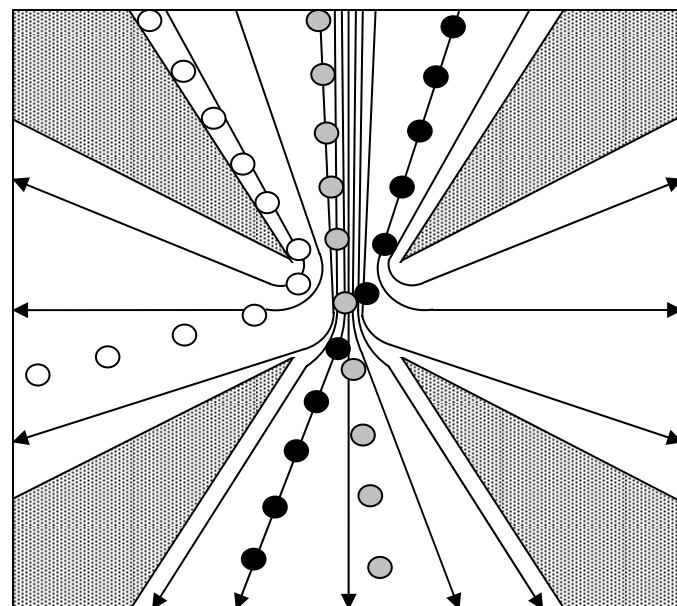
### 8.2.5 Characteristics of Convective Transport

From above results of visualization on the convective transport behavior of different sizes of solid particles in VI, their characteristics of motion can be defined as shown in Fig. 8.11. Solid arrow lines indicate air flow stream lines. Grey circles are laden by region A, the central flow region, and black circles are laden by region B, the outer region. Blank circles indicate that they are located within the near-wall area.

Figure 8.11-a schematically illustrates particles having lower Stokes numbers than 0.82. In this case, particles fully follow air streams even if air streams are deflected.



(a) Lower Stokes number (lower than 0.82)



(b) Higher Stokes Number (higher than 0.82)

Fig. 8.11. Schematically illustrated characteristics of convective transport of solid particles in virtual impactor as a function of Stokes number under a given flow rate.

For smaller particles located boundary layer (blank circles), boundary layer effect on these particles is negligible since their entering into major flows cause no concerns in this study. The characteristics of higher Stokes number are shown in Fig. 8.11-b. As cross trajectories in intersection area are visualized in previous section, particles which are laden in both region A and B enter into minor flow. Their angle of entering minor port is similar to their angle of approach in inlet. The particles laden within boundary layer, however, enter into major flow since they lost their inertia by the force of viscosity resulting in defect particles.

### 8.3 Mass Loading Effect on Current System

#### 8.3.1 Experimental Conditions

Four different conditions of mass loading from dust feeder have been calibrated. Table 8.3 shows ARD mass loading conditions. In Table 8.3, the designed mass loading condition is 600  $\mu\text{g/liter}$ . Loaded ARD is mixed with fluorescent particles at the inlet port and is introduced into nozzle throat.

Table 8.3  
Conditions of ARD mass loading from dust feeder

Condition	1	2	3	4
$\mu\text{g/liter}$	600 <sup>1</sup>	1,000	1,300	2,000

<sup>1</sup> Designed operation condition

The particle size of generated fluorescent for mass loading effect is  $4.4 \mu\text{m}$ . Under designed flow condition (10.26 SCFH of air volume flow rate), Stokes number for this fluorescent particle is about 7. At this number, collecting efficiency result shows that VI has less than 2 % of defect ratio on fluorescent particles. By detecting abnormal ratio of defect fluorescent particles, the condition of optimized mass loading can be decided.

### 8.3.2 Optimized Mass Loading Condition

Up to  $1,000 \mu\text{g/liter}$  of ARD mass loading, no defect particles have been detected. The abnormal defect ratio begins at  $1,300 \mu\text{g/liter}$ . Figure 8.12 shows experimental results of mass loading effect on defects particles. Image processing has been applied to Fig. 8.12 in order to overlap several frames and enhance resolutions. From this result of visualization, maximum mass loading for ARD can be established as  $1,000 \mu\text{g/liter}$ .

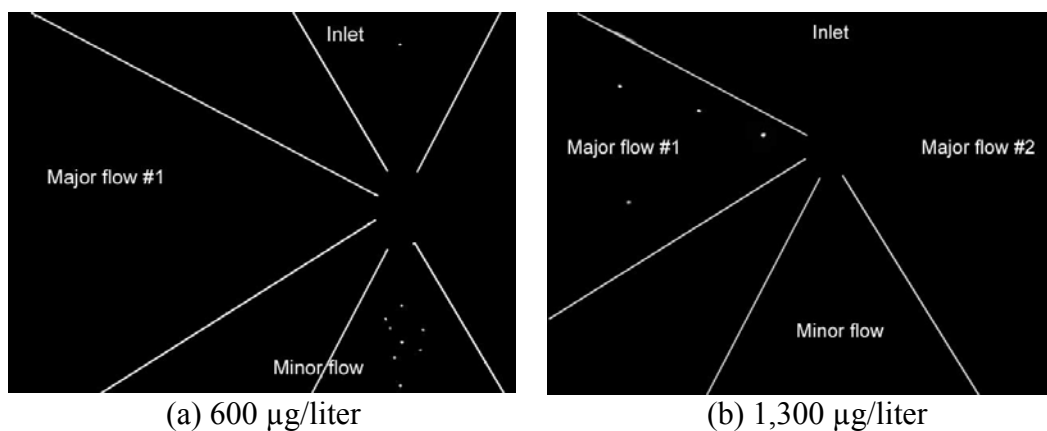


Fig. 8.12. Images of LIF for two different mass loading conditions ( $\dot{V}_{air} = 10.26$  SCFH,  $d_p = 4.4 \mu\text{m}$ ,  $Stk = 7$ ).

To recognize the effect of particles' interaction which will lead detrimental result on separation under high mass loading condition, nozzle throat area of VI has been investigated after 5 minutes of operation. Figure 8.13 shows the status of nozzle throat and clearly explains the detrimental effect of high mass loading on VI's working condition. In Fig. 8.13, the difference between lower mass loading (up to 1,000  $\mu\text{g/liter}$ ) and higher mass loading (higher than 1,300  $\mu\text{g/liter}$ ) is the status of clogging with ARD in the nozzle throat area. In Figs. 8.13-a and -b, no clogging has been observed. For the case of 1,300  $\mu\text{g/liter}$  and 2,000  $\mu\text{g/liter}$ , however, nozzle throat has been blocked by ARD. It is reasonable explanation that collision between particles is one example of particles' interaction and has responsibility on having a blockage at the nozzle throat. Statistically, the possibility of collision increases as mass loading increases since the number of particle in a given volume is increased. It is not clear whether particles' collision makes defect particles shown in Fig. 8.12-b, but it is definite that nozzle clogging causes malfunction of VI.

What has been seriously changed by clogging during operation is the change of air flow condition. The status of air flow condition is well represented by Fig. 8.14. In Fig. 8.14-a, the uniform distribution of ARD in major- and minor-flow for the condition of 600  $\mu\text{g/liter}$  is visualized. This indicates that the air flow condition is the identical as it is visualized in previous section. For the higher mass loading condition shown in Fig. 8.14-b, particle distribution becomes unstable having separation flow at the upper region of major flow since their air flow condition has been changed by blockage. Thus, previous result of visualization on collecting efficiency and the characteristics of

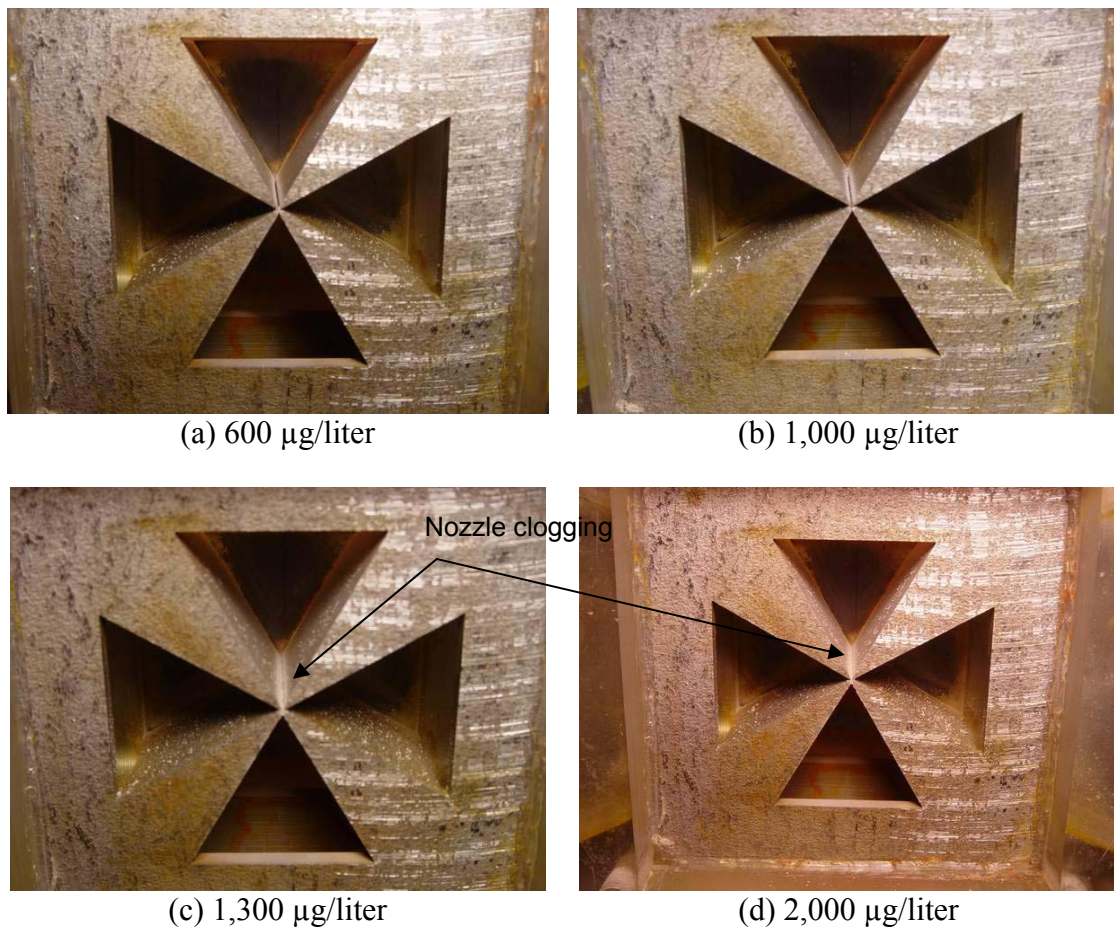


Fig. 8.13. The status of nozzle throat after running 5 minutes for four different mass loading conditions.

convective transport of particles can not be applied to this condition. For higher mass loading case, system can not be applied to separate designed particle size since flow condition has been dramatically changed by clogging caused by particle collision.



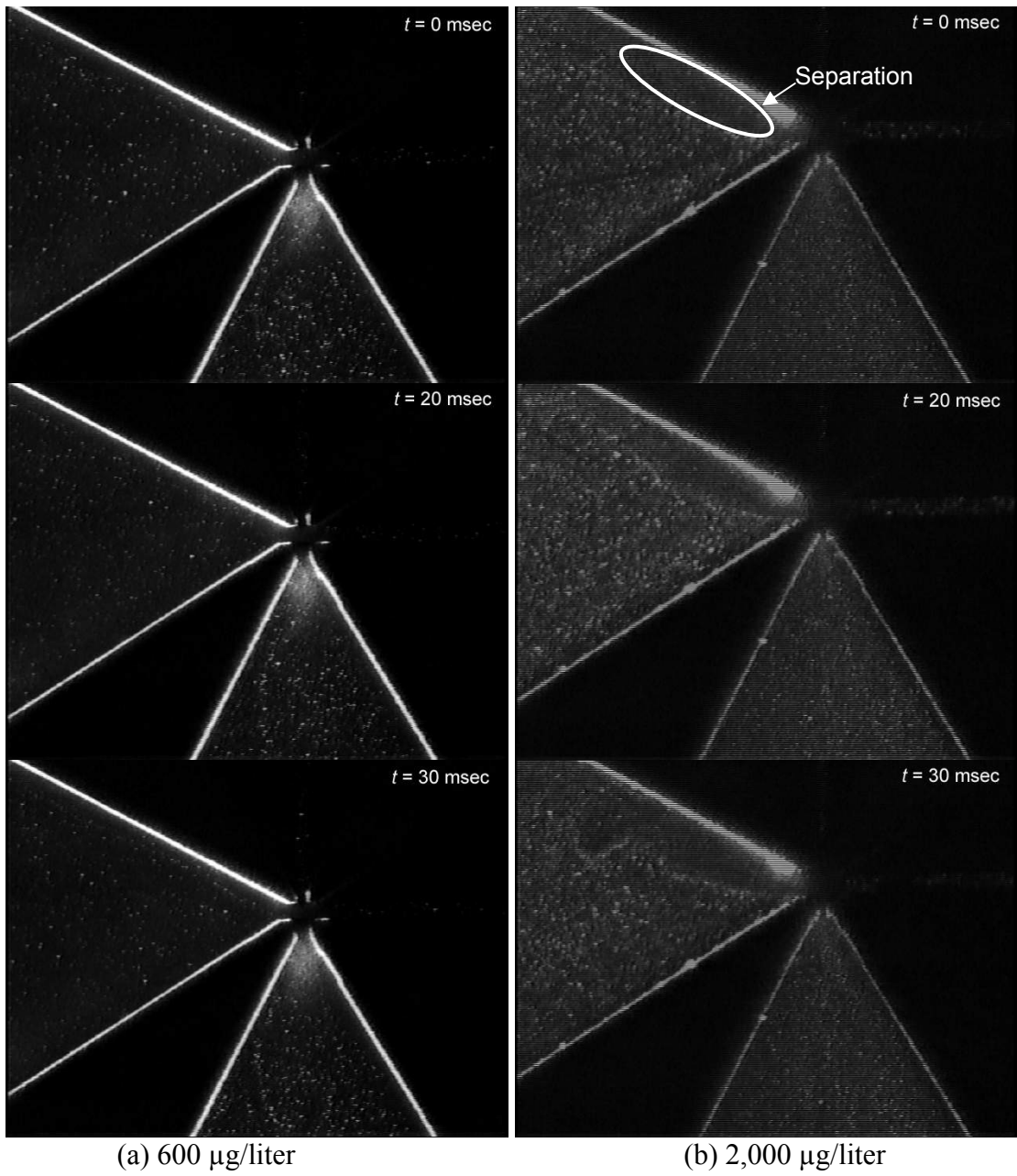


Fig. 8.14. Distribution patterns of particles for two different mass loading conditions.

### 8.3.3 Analysis of the Status at Nozzle Throat

Since current system will be applied to sorting precursor powder, some generalized references are needed to predict suitable condition of mass loading. From above experiments, it is clear that clogging caused by particles' collision makes current VI inoperative. To analyze initial point of clogging, particles' collision should be studied. Since the area of collision theory is beyond current research scope, simple analysis tool will be developed. The introduced method is to quantify the status of nozzle throat by using the ratio of cross-sectional area of particle to nozzle throat area. This concept is schematically illustrated in Fig. 8.15. The area of nozzle throat is known and black circles indicate polydisperse particles. The ratio of total cross-sectional area of the particles to the nozzle throat can be calculated if the number of particles is known. One problem is that particle size is polydisperse distribution. This can be overcome by applying cross-sectional area for a given number of particles which can be calculated as

$$A_c = \sum \left( \frac{1}{4} \pi d_i^2 \right) N_i \quad (8.3)$$

where  $d_i$  is the particle diameter and  $N_i$  is the number of particles at a given  $i$ . For example on ARD,  $A_c$  is  $1.7 \times 10^{-10} \text{ m}^2$  per 100 particles.

The number of particles can be mathematically calculated when mass loading is given under some assumptions. Since the mass of ARD per 100 particles is known from particle distribution data, total number of particles entering into inlet port can be calculated by a given mass loading condition as

$$\dot{N}_p [\#/s] = \frac{\dot{M}_A [kg/s]}{m_p [kg/particles]} \times 100 \quad (8.4)$$

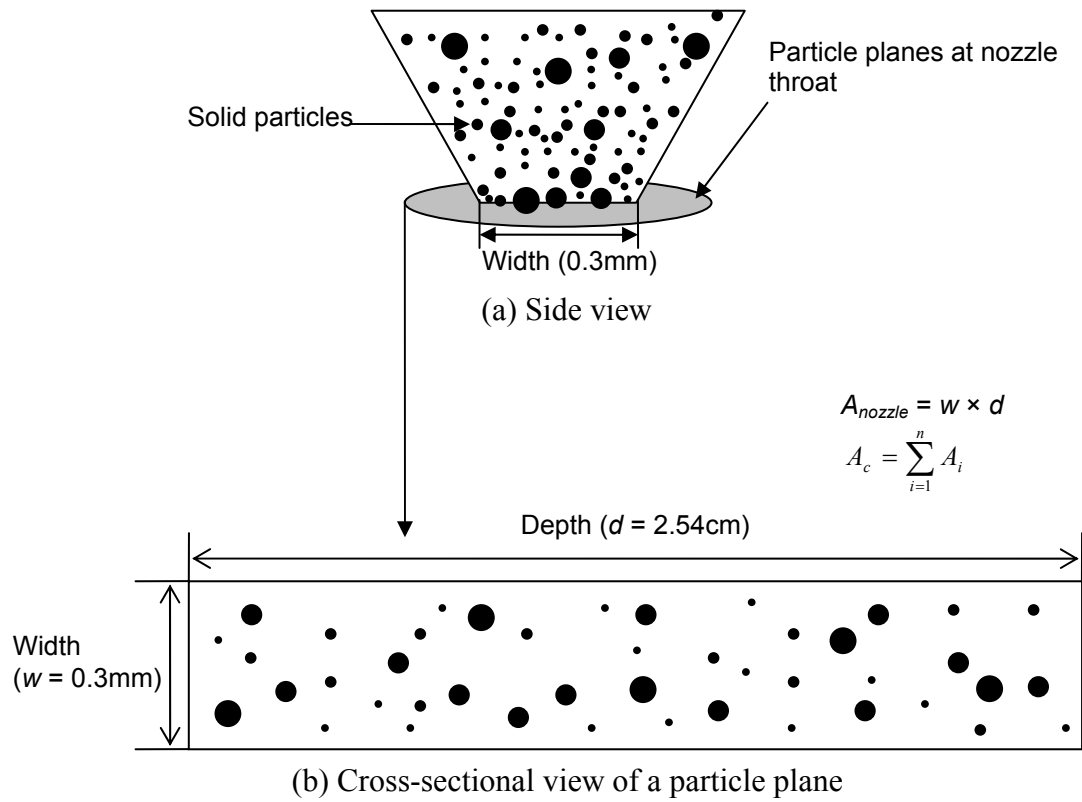


Fig. 8.15. The ratio of total cross-sectional area of particles which occupy a single plane at nozzle throat to area of nozzle throat.

where  $\dot{N}_p$  is the required particle number per second,  $\dot{M}_A$  is the applied mass loading to system,  $m_p$  is the amount of mass per 100 particles. To solve Eq. (8.4),  $\dot{M}_A$  should be known. This can be calculated by

$$\dot{M}_A [kg / s] = \dot{V}_{sys} [liter / s] \times M_D [kg / liter] \quad (8.5)$$

where  $\dot{V}_{sys}$  is the designed air volume flow rate and  $M_D$  is the designed mass loading of solid particles for the system.

Once a number of particles are calculated from Eq. (8.4), the distribution of particles at the inlet should be decided. Following assumptions are established to achieve particle distribution:

1. Uniform Distribution

To get distribution data of particles, it is assumed that all particles are distributed uniformly at inlet port (location of reservoir). The distribution of particle is not the function of particle size. The cross-sectional dimension of inlet, reservoir, is 2.7 cm for width and 2.54 cm for depth.

2. Identical Space Volume Occupied by Particles

The space volume occupied by particles is all identical. This satisfies the above assumptions. It indicates that each particle occupies identical size of cube.

From above assumptions, the concept of particle distribution is schematically illustrated in Fig. 8.16. The  $l_p$  is the length of each side of cube. To set up the reference control

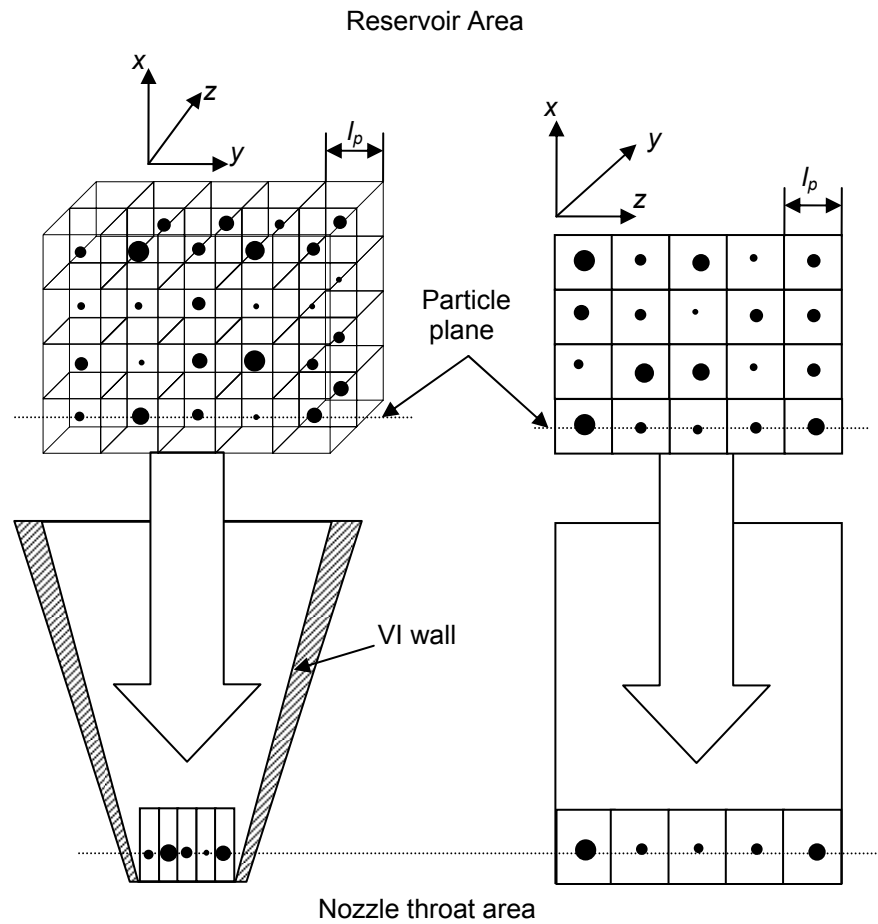


Fig. 8.16. Individual particle distribution in the reference volume.

volume, the length in  $x$ -direction is the velocity of air flow. Then, the reference volume of system is defined as

$$\dot{V}_{sys} [m^3 / s] = w_{inlet} [m] \times d_{inlet} [m] \times V_{air, inlet} [m / s] \quad (8.6)$$

Then, the volume of a cube occupied by a particle can be calculated by

$$V_{cube} [m^3 / particle] = \frac{\dot{V}_{sys} [m^3 / s]}{N_p [\# / s]} \quad (8.7)$$

From the result of Eq. (8.7), the length of each side is calculated by

$$l_p = (V_{cube})^{1/3} \quad (8.8)$$

Once  $l_p$  is obtained, the condition of particle distribution at inlet is completed for a given mass loading condition of solid particles. The one thing to be notified here is that particle size can not be larger than  $l_p$ .  $d_p$  is the same as  $l_p$  only when it is solid case.

Now, the nozzle throat condition needs to be considered. It can be assumed that inlet condition of particle distribution is maintained as particles approach to the nozzle throat. Although velocity profile is different at a given location in a particle plane, above assumption is reasonable since center region particles catch up particles located edge region of previous particle plane resulting identical number of particle plane. The shape of cube, however, is changing as it approaches to nozzle throat because of the law of continuity. The length of y-direction contracts and the x-direction elongates while z-direction remains as shown in Fig. 8.16. Thus, in y-direction, number of particles should have serious effect on the capability of VI's handling mass loading. Following tables will show the result of above equations. Table 8.4 shows total cross-sectional area and volume and mass per 100 particles of ARD. Table 8.5 shows result of solving Eqs. (8.4)-(8.8). In Table 8.5, the maximum mean particle size, is introduced and calculated as

$$d_{mean,max} [\mu m / particle] = \frac{w_{nozzle} [\mu m]}{\#of\ particle\ per\ width [particle]} \quad (8.9)$$

This indicates that if mean particle size is larger than this, particles can not pass through the nozzle since their dimension exceeds that of nozzle width.

Table 8.4

Cross-sectional area and volume of ARD per 100 particles

$A_c$ [m <sup>2</sup> /100 particles]	Volume [m <sup>3</sup> /100 particles]	$m_p$ [kg/100 particles]
1.70023E-10	8.74591E-16	2.31767E-12

Table 8.5

Result of analysis for number of particles in a reference volume

$M_D$ , Designed mass loading, [μg/liter]	600	1,000	1,300	2,000
$\dot{M}_A$ , Eq. (8.5) Applied mass loading to system, [μg/s]	48.46	80.77	105.00	161.54
$\dot{N}_p$ , Eq. (8.4), Required number of particles, [particles/s]	$2.09 \times 10^6$	$3.49 \times 10^6$	$4.53 \times 10^6$	$6.97 \times 10^6$
$V_{cube}$ , Eq. (8.7), [m <sup>3</sup> ]	$3.86 \times 10^{-11}$	$2.32 \times 10^{-11}$	$1.78 \times 10^{-11}$	$1.16 \times 10^{-11}$
$l_p$ , Eq. (8.8), [m]	$3.38 \times 10^{-4}$	$2.85 \times 10^{-4}$	$2.61 \times 10^{-4}$	$2.26 \times 10^{-4}$
<b>Particle # at inlet particle plane</b>				
Width <sup>1</sup> [particles]	$8.02 \times 10^1$	$9.51 \times 10^1$	$1.04 \times 10^2$	$1.20 \times 10^2$
Depth <sup>2</sup> [particles]	$7.51 \times 10^1$	$8.91 \times 10^1$	$9.72 \times 10^2$	$1.12 \times 10^2$
Particle number per plane <sup>3</sup> [particle]	$6.02 \times 10^3$	$8.47 \times 10^3$	$1.01 \times 10^4$	$1.34 \times 10^4$
$A_{tc}^4$ , Total cross-sectional area, [m <sup>2</sup> ]	$1.02 \times 10^{-8}$	$1.44 \times 10^{-8}$	$1.71 \times 10^{-8}$	$2.29 \times 10^{-8}$
% of $A_{tc}/A_{nozzle}$	0.134	0.189	0.225	0.300
$d_{mean,max}$ , Eq. (8.9), [μm]	3.74	3.16	2.89	2.51

<sup>1</sup> Calculated by  $w/l_p$ <sup>2</sup> Calculated by  $d/l_p$ <sup>3</sup> Products of 1 and 2<sup>4</sup> Calculated by  $N_p/100 \times A_c$

The ratio of total summation of particle diameter at a particle plane to nozzle width is considered since the dimension of nozzle width has critical role in collision rate. From particle distribution data, number mean diameter can be calculated as

$$d_{mean} = \frac{\sum N_i d_i}{N} \quad (8.10)$$

where  $d_{mean}$  is the average diameter of particle.  $N_i$  and  $d_i$  are the number of particle and particle size at a given particle range, respectively.  $N$  is the total number of particles. For ARD case,  $d_{mean}$  is 1.136  $\mu\text{m}$ . From this value, new reference value can be calculated as

$$R_{length} = \frac{N_{p,width} \times d_{mean}}{W_{nozzle}} \quad (8.11)$$

where  $R_{length}$  is the ratio of total summation of particle diameter at a particle plane to width and  $N_{p,width}$  is the particle number for width direction. The result of  $R_{length}$  indicates the ratio of length occupied by particles at nozzle throat. Table 8.6 shows calculation result of  $R_{length}$ . For the case of 600  $\mu\text{g/liter}$ , about 30% of nozzle width is filled with particles. From this analysis, it is recommended that the value of  $R_{length}$  is lower than 35% based on results of experiments and analytical investigation.

Table 8.6

Ratio of total summation of particles' diameter at a particle plane to nozzle width

Mass loading [ $\mu\text{g/liter}$ ]	600	1,000	1,300	2,000
$R_{length}$ [%]	30.35	35.98	39.27	45.34



## CHAPTER IX

### DISCUSSION AND FURTHER STUDY ON PART II

The characteristics of convective transport behavior of solid particles in VI have been investigated by means of visualization technique. The collecting efficiency of VI has been investigated by means of Mie-scattering method. The result shows that current system has very steep curve of collecting efficiency for designed particle range satisfying the requirement on selecting smaller particles for fabricating superconductor wire. The result, however, shows defect particles in the major flows. The visualization of convective transport behavior of solid particle verifies that the effect of boundary layer causes defect particles. By introducing local Stokes number, experimental result of defect particles can be analytically explained. Local Stokes number can be used for evaluating collecting efficiency and the thickness of boundary layer that affects the ratio of having defect particles.

The characteristics of convective transport behavior have been visualized. The distinguishable difference between smaller and larger particles is cross-trajectories during separation. This result satisfies the principle of inertia which is the basic principle of particle separation. Because of this behavior of different particle size, interaction between different size particles becomes serious when mass loading increases.

The effect of mass loading has been investigated. For the case of ARD, the mass loading of 1,000  $\mu\text{g/liter}$  is found for maximum mass loading condition. When higher mass loading (larger than 1,000  $\mu\text{g/liter}$ ) is applied, clogging at nozzle throat occurs resulting malfunction of operating VI. The concept of  $R_{length}$  has been applied in order to be used for different kinds of particle material since their particle distribution is different which has critical role in sorting process.

From above results, it is concluded that defect particles which should be prevented during sorting process occur because of two reasons; boundary layer effect and over loaded mass loading. Followings are recommended for having no defect particles using current VI system:

#### 1. Application of Sheath Flow of Clean Air

To eliminate boundary effect, sheath flow of clean air can be introduced in two walls of inlet. Figure 9.1 illustrates the recommended method of sheath flow. Since clean air of sheath flow prevents solid particles from being trapped in the boundary layer, defect particles can be eliminated. To maximize the amount of collecting solid particles, the amount of clean air flow rate should be minimized since introducing sheath flow in the inlet reduces the amount of mass loading as shown in Fig. 9.1. In Fig. 9.1, optimized  $y_s$ , the inlet width of sheath flow, can be established from the experiments results and analytical results by local Stokes number. To minimize  $y_s$  resulting in maximizing main air flow, the boundary condition of designed 99% cutoff size can be considered where Stokes number is 2. The experimental- and analytical-results

show 3% - 4% and 2% of defect ratio, respectively. To make 100 % cutoff size at this size, 5% of sheath flow would be enough to ensure maximized amount of main air flow.

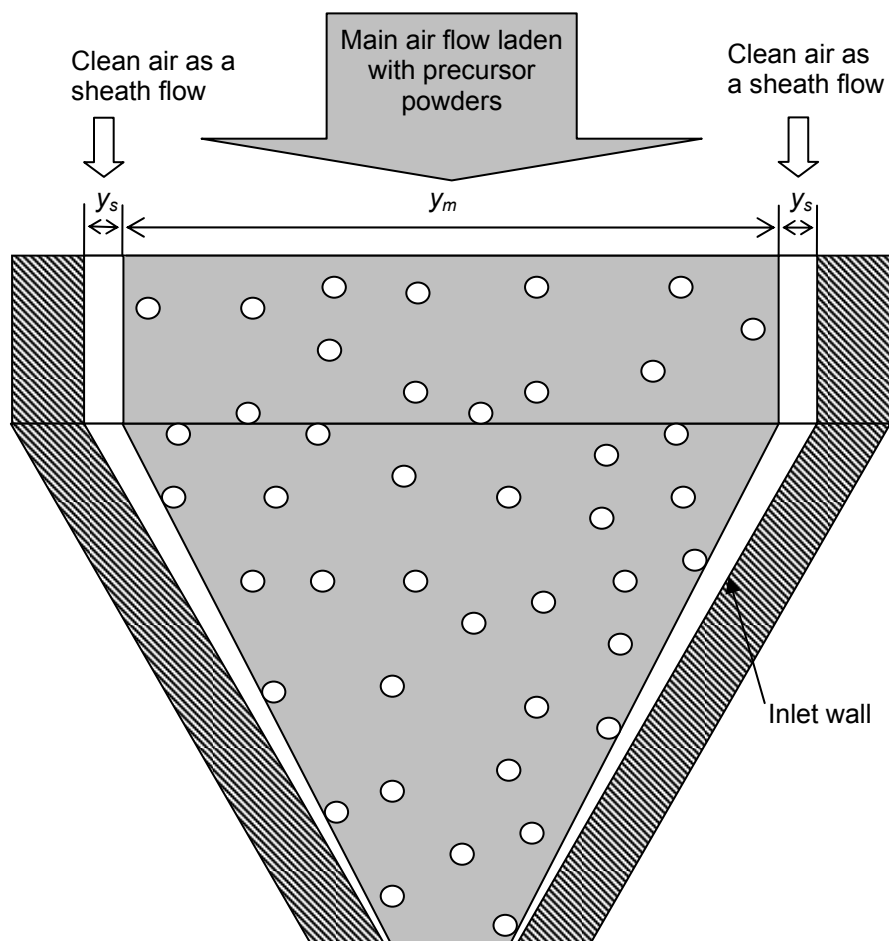


Fig. 9.1. Modified inlet design for eliminating defect particles by introducing clean air of sheath flow.

## 2. Selection of Suitable Mass Loading

To maximize mass loading, the number of particles that passes through the nozzle throat at a given time should be considered. If the number of particles exceeds maximum capacity of nozzle throat area, clogging occurs. By using  $R_{length}$ , maximum mass loading can be calculated. Experimental results show that 35% of  $R_{length}$  is the maximum for not having clogging at the nozzle throat. Table 9.1 shows the  $R_{length}$  result of precursor powder (particle distribution shown in Fig. 6.2 having the density of 3 g/cm<sup>3</sup>). Since the density has been increased from 2.65 g/cm<sup>3</sup>, the number of particle has been reduced to satisfy mass loading condition. In Table 9.1, the value of  $R_{length}$  of precursors is higher than that of ARD at a given mass loading condition because their number mean diameter is larger than that of ARD. The number mean diameters are 1.58 μm and 1.49 μm for Bi-2223 and Bi-2212, respectively. According to the result of ARD, it is recommended to apply lower mass loading condition for these precursor powder since their  $R_{length}$  is higher. If the concept of  $R_{length}$  is correct, maximum mass loading for Bi-2223 and Bi-2212 is 400 μg/liter and 500 μg/liter, respectively.

From experimental results and analytical investigation, current system has a good capacity of sorting different size of particles. To completely confirm above two recommendations, researches for the investigation on collecting efficiency of using clean

sheath flow and the examination on the concept of  $R_{length}$  using different particles whose size distribution are highly recommended.

Table 9.1  
 $R_{length}$  for precursors

Mass loading [ $\mu\text{g/liter}$ ]	400	500	600	700
Bi-2223	35.38	38.11	40.50	42.64
Bi-2212	33.33	35.91	38.16	40.17

► Number of particles at the mass loading of 600  $\mu\text{g/liter}$ :  $2.09 \times 10^6$  for Arizona Road Dust and  $1.85 \times 10^6$  for precursor powder

## CHAPTER X

### CONCLUSION

The experimental efforts have been conducted to investigate the characteristics of two types of aerosols, liquid and solid, by means of the optical diagnostic methods. The empirical results for both of them show good agreement with the basic principles of theories. These achievements are listed in Chapter V and Chapter IX and are possible with optical diagnostic techniques.

In Part I, the correlations have been established to predict atomized liquid particle size of six different HTFs in order to apply safety standard evaluation in the process industries. It should be better to select a fluid that generates larger liquid droplet size when it forms mist from leakage under the identical working conditions. To evaluate properly, the consolidated effect of liquid properties on mist formation should be considered. This can be achieved by evaluating two non-dimensional number, Ohnesorge and Reynolds number. Although the process of atomization is too random to be categorized for different conditions, these two non-dimensional numbers can give general evaluation of disintegration status of leaked HTFs under given conditions allowing a comparison of formed liquid particle size between different fluids.

In Part II, the characteristics of convective transport of solid aerosols in VI have been investigated. It is examined that the collecting efficiency of smaller particle is satisfied for the objective of applying current system to the process of manufacturing

superconductor industries. The local Stokes number is introduced to explain defect particles which was found during experiments and shows good agreement with experimental results. This indicates that the boundary effect is blamed for having defect particles. The sheath flow of clean air is recommended for eliminating defect particles. The different characteristics of convective transport behavior of different size of particle have been visualized. The difference between them is the cross-trajectory transport of larger particle in the separation region under a given flow condition. These results fully satisfy the principle of particle dynamics, the principle of inertia. The effect of different mass loading has been investigated. The maximum mass loading for ARD has been found as 1,000  $\mu\text{g/liter}$ . Beyond this amount, interaction between particles is so serious resulting defects particles and nozzle throat clogging. The ratio of summation of mean particle diameter to the width of nozzle throat, the concept of  $R_{length}$  has been introduced to apply to different types of solid particles whose size distribution is different. Experimental results show that maximum value of  $R_{length}$  is 35% for the case of ARD. This value can be applied to precursor powder.

## REFERENCES

Asihmin, V. I., Geller, Z. I., and Skoble'cyn, Y. A. (1961). Discharge of a Real Fluid from Cylindrical Orifice. *Oil Industry*, 9, 135-172.

Berglund, R. N. and Liu, B. Y. H. (1973). Generation of Monodisperse Aerosol Standards. *Environmental Science and Technology*, 7, 147-153.

Bowen, P. J. and Cameron, R. J. (1999). Hydrocarbon Aerosol Explosion Hazards: A Review. *Trans IChemE*, 77, Part B, 22-30.

Buckingham, E. (1914). On Physically Similar Systems: Illustration of the Use of Dimensional Equations. *Physical Review*, 4, 345-376.

Burgoyne, J. H., and Cohen, L. (1954). The Effect of Drop Size on Flame Propagation in Liquid Aerosols. *Proc. Roy. Soc. A*, 225, 375-392.

Cameron, L. R. J., and Bowen, P. J. (2001). Novel Cloud Chamber Design for 'Transition Range' Aerosol Combustion Studies. *Trans IChemE*, 79, Part B, 197-205.

Chan, K., and Jou. C. (1988). An Experimental and Theoretical Investigation of the Transition Phenomenon in Fuel Spray Deflagration – 1. The Experiment. *Fuel*, 67, 1222-1227.

Chan, K. and Wu, S., (1989). An Experimental and Theoretical Investigation of the Transition Phenomenon in Fuel Spray Deflagration – 2. The Model. *Fuel*, 68, 139-144.



Chen, B. T. and Yeh, H. C. (1987). An Improved Virtual Impactor: Design and Performance. *J. Aerosol Sci.*, 18(2), 203-214.

Conner, W. D. (1966). An Inertial-Type Particle Separator for Collecting Large Samples. *J. of the Air Poll. Cont. Assoc.*, 16(1), 35-38.

Christanti, Y. and Walker, L. M. (2001). Surface Tension Driven Jet Break Up of Strain-hardening Polymer Solutions. *J. Non-Newtonian Fluid Mech.*, 100, 9-26.

Ding, Y. and Koutrakis, P. (2000). Development of a Dichotomous Slit Nozzle Virtual Impactor. *J. Aerosol Sci.*, 31(12), 1421-1431.

Eichhorn, J. (1955). Careful! Mist Can Explode. *Petroleum Refiner*, 34,(11), 194-196.

EPA (2002). *World Trade Center Disaster Response Air Monitoring Data Summaries*. Available at <http://www.epa.gov/wtc/summary.html>.

Febo, H. L. and Valiulis, J. V. (1995). *Heat Transfer Fluid Mist Explosion Potential an Important Consideration for Users*. In AIChE Loss Prevention Symposium, Norwood, MA. Paper 4F.

Flüsener, O. (1933). The Injection Process in Compressorless Diesel Engines. *VDI-Zeitschrift*, 77 (7), 171-172.

Fristrom, R. M. (1995). *Flame Structure and Process*, New York: Oxford University Press.

Frohn, A. and Roth, N. (2000). *Dynamics of Droplets*, New York: Springer.

Fu, X., Gupta, A., McIntyre, P. M., and Phares, D. (2003). New Size Sorting Technology for Superconducting Powders. *IEEE Transactions on Applied Superconductivity*, 13, 3494-3497.

Fuchs, N. A. (1964). *The Mechanics of Aerosols*, New York: Macmillan.

Gotoh, K. and Masuda, H. (2000). Improvement of the Classification Performance of Rectangular Jet Virtual Impactor. *Aerosol Science and Technology*, 32, 212-232.

Guo, Y. C., Li, J. N., Yavuz, M., Vance, E. R., and Cou, X. Z. (1996). Effect of Precursor Powder on the Properties of Silver-Clad Bi-2223 Superconducting Wires and Tapes. *Advances in Cryogenic Engineering*, 42, 761-768.

Han, R. and Moss, O. R. (1997). Flow Visualization Inside a Water Model Virtual Impactor. *J. Aerosol Sci.*, 28(6), 1005-1014.

Haugan, T., Chen, S., Patel, S., Wong, F., Bush, P., and Shaw, D. T. (1995). Pinhole Defects in Ag Sheath of PIT Bi-2212 Tapes. *Cryogenics*, 35, 853-859.

Hecht, E. (1998). *Optics* (3rd ed.), New York: Addison Wesley Longman, Inc..

Herman, B. (1998). *Fluorescent Microscopy* (2nd ed.), New York: Springer.

Hinds, W. C. (1999). *Aerosol Technology: Properties, Behavior, and Measurement of Airborne Particles* (2nd ed.), New York: John Wiley & Sons.

Hinze, J. O. (1955). Fundamental of the Hydrodynamic Mechanism of Splitting in Dispersion Processes. *AIChE J.*, 1, 289-295.

Hirleman, E. D. (1994). Nonintrusive Laser-Based Particle Diagnostics. *Progress in Astronautics and Aeronautics*, 92, 177-207.

Hirleman, E. D., Bachalo, W. D., and Felton, P. G. (1990). *Liquid Particle Size Measurement Techniques, Vol. 2*, Pittsburg, PA: American Society for Testing and Materials.

Jiang, J and Abell, J. S. (1998). Effects of Precursor Powder Particle Size on Critical Current Density and Microstructure of Bi-2223/Ag Tapes. *Physica C*, 296, 13-20.

Kihm, K., D., Kim, T. K., and Son, S. Y. (1999). Visualization of High-Speed Gas Jets and Their Airblast Sprays of Cross-Injected Liquid. *Experiments in Fluids*, 27, 102-106.

Kihm, K. D. Terracina, D. P., and Caton. J. A. (1995). Spray-Tip Droplet SMDs of Intermittent High-Pressure Sprays of Diesel Fuel Compared with Coal-Water Slurry Sprays. *Journal of the Institute of Energy*, 68, 57-64.

Koo, J. H., and Hirleman, E. D. (1996). Review of Principles of Optical Techniques for Particle Size Measurement. *Progress in Astronautics and Aeronautics*, 166, 3-32.

Lee, P., Chen, D., and Pui, D. Y. (2003). Experimental Study of a Nanoparticle Virtual Impactor. *Journal of Nanoparticle Research*, 5, 269-280.

Lefebvre, A. H. (1989). *Atomization and Sprays*, New York: Hemisphere Publishing.

Levendis, Y. A. and Flagan, R. C. (1987). Combustion of Uniformly Sized Glassy Carbon Particles. *Combust. Sci. and Tech.*, 53, 17-136.

Loo, B. W. and Adachi, R. S. (1979). A Second Generation Dichotomous Sampler for Large Scale Monitoring of Airborne Particulate Matter. *Lawrence Berkeley Laboratory Report*, No. LBL-8752, Berkeley, California.

Marple, V. A. and Chien C. M. (1980). Virtual Impactors: A Theoretical Study. *Environmental Science & Technology*, 14(8), 976-985.

Marple V. A., and Liu, B. Y. H. (1974). Characteristics of Laminar Jet Impactors. *Environmental Science & Technology*, 8(7), 648-654.

Marple, V. A., and Liu, B. Y. H., and Whitby, K. T. (1974). Fluid Mechanics of the Laminar Flow Aerosol Impactor. *J. Aerosol Sci.*, 5, 1-16.

Miesse, C. C. (1955). Correlation of Experimental Data on the Disintegration of Liquid Jets. *Ind. Eng. Chem.*, 47(9), 1690-1701.

Mugele, R. and Evans, H. D. (1951). Droplet Size Distribution in Sprays. *Ind. Eng. Chem.*, 43(6), 1417-1324.

Nakayama, Y. (1961). Action of the Fluid in the Air Micrometer: First Report, Characteristics of Small Diameter Nozzle and Orifice. *Bull. Japan. Soc. Mech. Eng.*, 4, 516-524.

Nakayama, Y. and Tanida, Y. (1997). *Atlas of Visualization III, The Visualization Society of Japan*, New York: CRC Press.

Ohnesorge, W. (1936). Formation of Drops by Nozzles and the Breakup of Liquid Jets. *Z. Angew. Math. Mech.*, 16, 355-358.

Park, J. S., McCarty, C., Kihm, K. D., and Pratt, D. M. (2000). Lagrangian Flow Mapping of Heated Capillary Pore and Thin Film Using Molecular Fluorescence Velocimetry (MFV). *J. of Heat Transfer*, 122, 423.

Polymeropoulos, C. E. (1984). Flame Propagation in Aerosols of Fuel Droplets, Fuel Vapor and Air. *Combustion Science and Technology*, 40, 217-232.

Prandtl, L. (1904). Über Flüssigkeitsbewegung bei sehr kleiner Reibung. Proc. Verhandlungen des III., Internationalen Mathematiker-Kongresses, Heidelberg, Teubner, Leipzig, 404-491.

Raffel, M., Willert, C., and Kompenhans, J. (1998). *Particle Image Velocimetry*, New York: Springer.

Rayleigh, Lord (1978). On the Instability of Jets. *Proc. London Math. Soc.*, 10, 4-13.

Reitz, R. D. (1978). Atomization and Other Breakup Regimes of a Liquid Jet. Ph. D. dissertation, New Jersey: Princeton University.

Rosin, P. and Rammler, E. (1933). The Laws Governing the Fineness of Powdered Coal. *J. Inst. Fuel*, 7(31), 29-36.

Schlichting, H. (1979). *Boundary-Layer Theory* (7th ed.), New York: McGraw-Hill.

Schneider, J. M. and Hendricks, C. D. (1964). Source of Uniform-sized Liquid Droplets. *The Review of Scientific Instrument*, 35(10), 1349-1350.

Sioutas, D., Koutrakis, P., and Burton, R. M. (1994). Development of a Low Cutpoint Slit Virtual Impactor for Sampling Ambient Fine Particles. *J. Aerosol Sci.*, 25(7), 1321-1330.

Sukmarg, P., Krishna, K., Rogers, W. J., Kihm, K. D., and Mannan, M. S. (2002). Non-intrusive Characterization of Heat Transfer Fluid Aerosol Sprays Released from an Orifice. *J. of Loss Prevention in the Process Industries*, 15, 19-27.

Sullivan, M. V., Wolfe, J. K., and Zisman, W. A. (1947). Flammability of the Higher Boiling Liquids and Their Mists. *Industrial and Engineering Chemistry*, 39(12), 1607-1614.

Swithenbank J, Beer J., and Taylor D. S. (1977). A laser diagnostic technique for the measurement of droplet and particle size distributions. *Prog. Aeronaut*, 53, 421-425.

Syamaprasad, U., Sarma, M.S., Guruswamy, P., Prakash Kumar, V., Ragini, R., Warriar, K. G. K., and Damodaran, A. D. (1998). Effect of Precursor Phase Assemblage on 2223 Phase Formation and  $J_c$  in Ag/(Bi,Pb)-2223 Tapes. *Physica C*, 297, 85-90.

Turns, S. R. (2000). *A Introduction to Combustion: Concepts and Applications*, New York: McGraw Hill.

Tyler, F. (1933). Instability of Liquid Jets. *Philos. Mag. (London)*, 16, 504-518.

van de Hulst, H. C. (1981). *Light Scattering by Small Particles*, New York: Dover.

Varde, K. S. and Popa, D. M. (1984). Diesel Fuel Spray Penetration at High Injection Pressure. *SAE Paper 830448*.

Wen, F., Kamalu, N., Chung, J. N., Crowe, C. T., and Troutt, T. R. (1992). Particle Dispersion by Vortex Structures in Plane Mixing Layers. *Journal of Fluids Engineering*, 114, 657-666.

## APPENDIX A

### PROCEDURES OF ESTABLISHING CORRELATION

Eq. (2.4) shows the parameters which are applied for establishing correlations for predicting atomized particle sizes as

$$d = f(d_o, x, V, \sigma, \mu_l, \mu_g, \rho_l, \rho_g) \quad (2.4)$$

where  $d$  [L] is the atomized mean droplet diameter (SMD),  $d_o$  [L] is the nozzle orifice diameter,  $x$  [L] is the axial distance from the nozzle orifice,  $V$  [L/T] is the initial velocity of the liquid at nozzle orifice,  $\sigma$  [L/T<sup>2</sup>] is the liquid surface tension,  $\mu_l$  [M/LT] is the dynamic liquid viscosity,  $\mu_g$  [M/LT] is the dynamic ambient gas viscosity,  $\rho_l$  [M/L<sup>3</sup>] is the atomized liquid density, and  $\rho_g$  [M/L<sup>3</sup>] is the ambient gas density. Brackets indicate dimension of parameters; L (Length), T(Time), and M(Mass).

From Buckingham pi theorem, 6 pi groups can be formed by power products since there are 9 variables and three dimensions. In this research,  $d_o$ ,  $V$ , and  $\rho_g$  are designated as repeating variables. The pi groups are expressed as

$$f(\Pi_1, \Pi_2, \Pi_3, \Pi_4, \Pi_5, \Pi_6) = 0 \quad (A.1)$$

where

$$\Pi_1 = d_o^{a_1} V^{b_1} \rho_g^{c_1} d \quad (A.2)$$

$$\Pi_2 = d_o^{a_2} V^{b_2} \rho_g^{c_2} \sigma \quad (A.3)$$

$$\Pi_3 = d_o^{a_3} V^{b_3} \rho_g^{c_3} \mu_l \quad (A.4)$$



$$\Pi_4 = d_o^{a4} V^{b4} \rho_g^{c4} \mu_g \quad (\text{A.5})$$

$$\Pi_5 = d_o^{a5} V^{b5} \rho_g^{c5} \rho_L \quad (\text{A.6})$$

$$\Pi_6 = d_o^{a6} V^{b6} \rho_g^{c6} x \quad (\text{A.7})$$

18 exponents that make the product dimensionless in Eqs. (A.1-A.7) can be algebraically found. 6 pi parameter

$$\Pi_1 = \frac{d}{d_o} \quad (\text{A.8})$$

$$\Pi_2 = \frac{\sigma}{\rho_g V^2 d_o} = We_g \quad (\text{A.9})$$

$$\Pi_3 = \frac{\mu_l}{\rho_g V d_o} \quad (\text{A.10})$$

$$\Pi_4 = \frac{\mu_g}{\rho_g V d_o} \quad (\text{A.11})$$

$$\Pi_5 = \frac{\rho_l}{\rho_g} \quad (\text{A.12})$$

$$\Pi_6 = \frac{x}{d_o} \quad (\text{A.13})$$

In Eq. (A.9),  $\Pi_2$  is formed by Weber number, well known non-dimensional parameter indicating the ratio of inertia to surface tension. Eqs. (A.10) and (A.11) show the same formation except property of viscosity term. The procedure of regrouping is needed to setup well known dimensionless parameter and make parameter simple.

$$\Pi'_3 = \frac{\Pi_5}{\Pi_3} = \frac{\rho_l V d_o}{\mu_l} = Re_l \quad (\text{A.14})$$

$$\Pi'_4 = \frac{\Pi_3}{\Pi_4} = \frac{\mu_l}{\mu_g} \quad (\text{A.15})$$

In Eq. (2.18), Reynolds number that indicates the ratio of inertia to viscosity forms  $\Pi'_3$ .

From above results, Eq. (2.4) becomes

$$\frac{d}{d_o} = f\left(\frac{\sigma}{\rho_g V^2 d_o}, \frac{\rho_l V d_o}{\mu_l}, \frac{\mu_l}{\mu_g}, \frac{\rho_l}{\rho_g}, \frac{x}{d_o}\right) \quad (\text{A.16})$$

or

$$\frac{d}{d_o} = f\left(We_g, Re_l, \frac{\mu_l}{\mu_g}, \frac{\rho_l}{\rho_g}, \frac{x}{d_o}\right) \quad (\text{A.17})$$

From Eq. (A.17), correlation for atomized droplet size is setup as

$$\frac{d}{d_o} = Cont. (We_g)^{e1} (Re_l)^{e2} \left(\frac{\mu_l}{\mu_g}\right)^{e3} \left(\frac{\rho_l}{\rho_g}\right)^{e4} \left(\frac{x}{d_o}\right)^{e5} \quad (2.5)$$

## APPENDIX B

### SURFACE TENSION MEASUREMENT

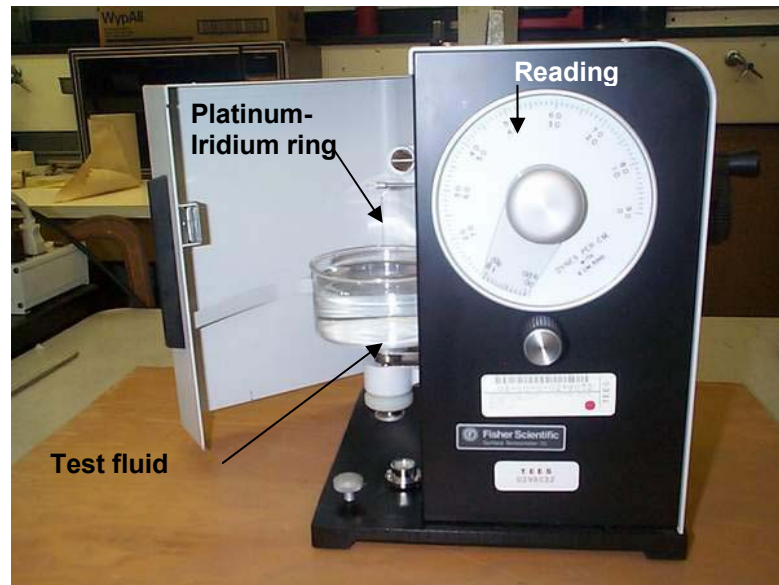
Fisher Surface Tensiomat model 20 shown in Fig B.1 is applied to measure surface tension. It can measure the surface tension range of 0-90 dyne/cm. In Fig. B.1-b, a platinum-iridium ring of precisely known dimensions is suspended from a counter-balanced lever-arm. The arm is held horizontal by torsion applied to a taut stainless steel wire, to which it is clamped. Application of torsion to raise ring and simultaneous lowering of sample table are done manually. The force necessary to pull the test ring free from this surface tension film is measured.

Applying known mass to Platinum-iridium ring instead of surface tension of fluid, the accuracy of Tensiomat reading is determined. The accurate reading can be calculated by

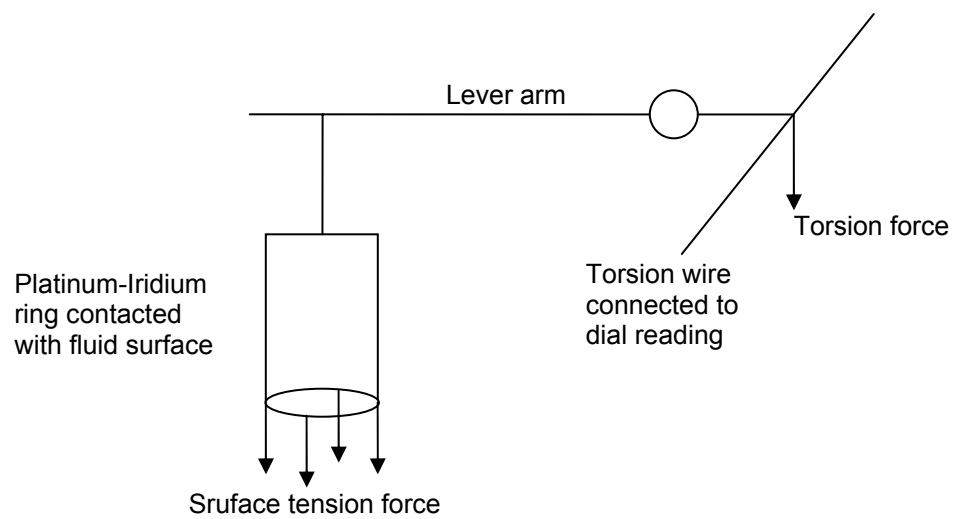
$$S = \frac{Mg}{2L} \quad (\text{B.1})$$

where  $M$  is the known weight expressed in grams,  $g$  is acceleration of gravity in  $\text{cm}/\text{sec}^2$ ,  $L$  is mean circumference of the ring in centimeter, and  $S$  is dial reading (apparent surface tension in dynes per cm). Table B.1 shows the calculated reading for this experiment. For all experiments, the difference between readings and calculated value is below 1.5%. Applied three thermocouples and thermo-meter are calibrated at ice melting point.

In order to verify the accuracy of surface tension measurement, the surface tension of water and AAR are measured because their surface tensions are known.



(a) General apparatus



(b) Enlargement of platinum-iridium ring

Fig. B.1. Apparatus of Fisher Surface Tensiometer Model 20.

Figure B.2 shows the results of verification experiments. Overall results of verification experiments show that the difference between measurement and manufacturer's data is below than 10%.

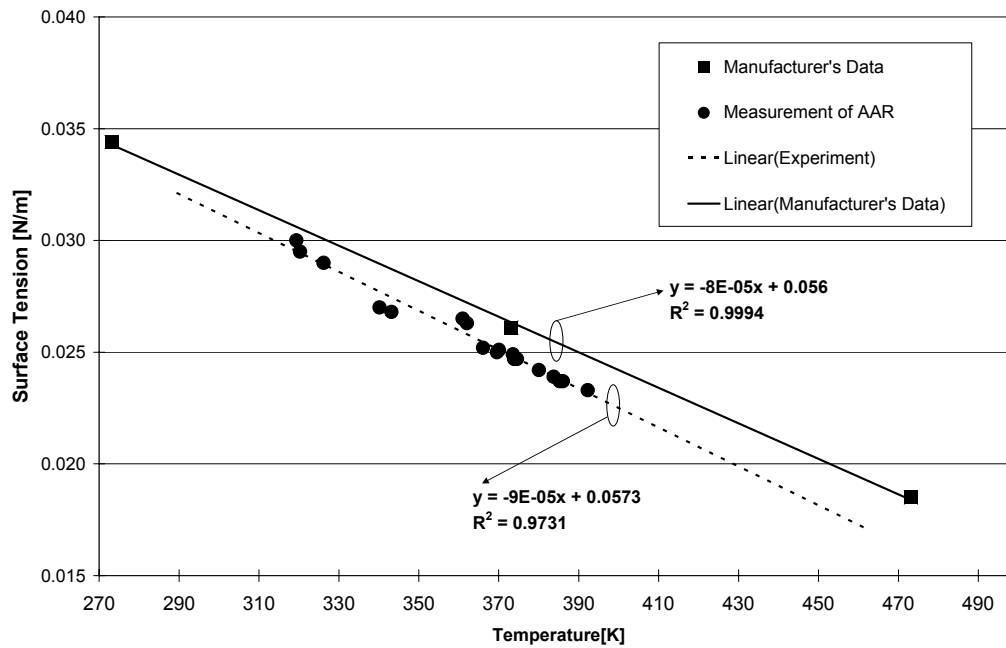


Fig. B.2. Comparison of surface tension between given data from manufacturer and measurement on AAR.

Table B.1

Calculated value of reading

$M$	0.73	0.74	0.75
$S$	60.3	61.1	62.0

\* Applied weight: 0.74 g, \*\*  $g = 980 \text{ cm/sec}^2$ , \*\*\* $L = 5.930 \text{ cm}$

## APPENDIX C

### REGRESSION METHOD

Regression using the least squares method is applied to achieve correlation on prediction of atomized particle size as a function of liquid properties and atomization conditions. The correlations is set up by Buckingham theory and shown in Eq. (2.5) as

$$\frac{d}{d_o} = Cont.(We_g)^{e1}(Re_l)^{e2}\left(\frac{\mu_l}{\mu_g}\right)^{e3}\left(\frac{\rho_l}{\rho_g}\right)^{e4}\left(\frac{x}{d_o}\right)^{e5} \quad (2.5)$$

Microsoft Excel offers regression analysis tool using the linear least squares method to fit a line through a set of empirical data. To obtain parameters in Eq. (2.5), it needs to be converted into linear equation since Eq. (2.5) is power series. By applying logarithm for both sides, Eq. (2.5) is converted into

$$\ln\left(\frac{d}{d_o}\right) = \ln\left( cont.(We_g)^{e1}(Re_l)^{e2}\left(\frac{\mu_l}{\mu_g}\right)^{e3}\left(\frac{\rho_l}{\rho_g}\right)^{e4}\left(\frac{x}{d_o}\right)^{e5}\right) \quad (C.1)$$

From the nature of logarithm, Eq. (B.1) is converted into final form of linear equation of Eq. (2.5) as

$$\begin{aligned} \ln\left(\frac{d}{d_o}\right) = & \ln(cont.) + e1 \times \ln(We_g) + e2 \times \ln(Re_l) + e3 \times \ln\left(\frac{\mu_l}{\mu_g}\right) + \\ & e4 \times \ln\left(\frac{\rho_l}{\rho_g}\right) + e5 \times \ln\left(\frac{x}{d_o}\right) \end{aligned} \quad (C.2)$$

By applying above linear regression method to Eq. (2.5), all parameters can be achieved.

**VITA**

Tae-Kyun Kim

Department of Mechanical Engineering

Texas A&amp;M University

College Station, TX 77843-3123

**Personal Data**

Date of Birth: Nov. 30, 1967

Spouse: Duk Jin Jung

Sons: Woo Sung Kim and Woo Jin Kim

Parents: Duk Hyun Kim and Soon Ja Kim

Permanent Address: Jongro-Gu Buam-Dong 208, Hanmaum Villa 101  
Seoul, 110-817, Republic of Korea**Education**

Ph. D., Mechanical Engineering, Texas A&amp;M University, May 2004

M.S., Mechanical Engineering, Texas A&amp;M University, Aug. 1996

B.S., Mechanical Engineering, Korea Military Academy, Mar. 1990

**Academic Professional Experience at Texas A&M University**

Research Assistant in Dept. of Mechanical Engineering, Jan. 2000 – Dec. 2003

Teaching Assistant in Dept. of Mechanical Engineering, Aug. 2002 – Dec. 2002

**Military Professional Experience in Korean Army**

Company Commander at Special Forces, Feb. 1997 - Aug. 1998

Battalion Headquarters Company Commander, Dec. 1992 – Dec. 1993

Infantry Platoon Leader/Operational-Air Staff of Battalion, Aug. 1990 - Dec. 1992